Optimization of Neck Musculature Activation for Head Kinematics in Frontal, Lateral and Rear Impact Simulations

by

Matheus Augusto Correia

A thesis
presented to the University of Waterloo
in fulfillment of the
thesis requirement for the degree of
Master of Applied Science
in
Mechanical Engineering

Waterloo, Ontario, Canada, 2020

Author’s Declaration

I hereby declare that I am the sole author of this thesis. This is a true copy of the thesis, including any required final revisions, as accepted by my examiners.

I understand that my thesis may be made electronically available to the public.

Abstract

The activation of the neck musculature plays an important role in the response of the head and neck and can affect the risk of injury under impact conditions. Yet, the role of the level (*i.e.*, magnitude) and timing of the neck muscle activation towards injury risk remains not well understood. Advanced finite element Human Body Models (HBMs) can predict the kinematic response of the head and neck upon impact, providing critical information to researchers and vehicle safety systems designers, but there is currently a lack of verified and validated schemes for neck muscle activation. This thesis focused on improving understanding of neck musculature activation by identifying optimized activation schemes for different impact scenarios using the 50th percentile male GHBMC contemporary finite element HBM assessed with experimental human volunteer impact test data. The HBM head-neck kinematics were evaluated for frontal, lateral and rear impacts over a wide range of accelerations, which represents novel information not found in the existing literature. The two main hypotheses were: (1) for different impact scenarios, the optimal muscle activation (OMA) schemes could be determined using the experimental volunteer kinematics, and (2) that a single muscle activation scheme could achieve a good correlation for all impact cases.

The optimization results were assessed using volunteer data of 119 frontal impacts between 2g and 15g, 72 lateral impacts between 4g and 7g and 12 rear impacts between 3g and 4g. The frontal and lateral impacts data was collected from widely referenced studies with 16 volunteers, and rear impact data was collected from recent tests with 12 volunteers. No muscle activation data was recorded in the available experimental data; however, the studies presented kinematics of the head and first thoracic (T1) vertebra that were compared to the output of the computational HBM.

The optimized muscle activation schemes improved the kinematic response for all impact cases (maximum average improvement of 35% for the frontal impacts) and could be used to elucidate the

influence of muscle activation and onset time in head kinematics in other impact severities and directions. A novel Cocontraction Muscle Activation (CMA) scheme presented good correlation with frontal (23% average improvement), lateral (17% average improvement) and rear (6% average improvement) impacts, confirming the hypothesis that a unique activation scheme could be used to achieve an improved correlation of HBM global head kinematics with the experimental data. Furthermore, this work identified that the rear impact simulations demonstrated less sensitivity than the other impact directions for different muscle activation schemes. The lower sensitivity could be attributed to the reduced force associated with flexor muscles, which were antagonistic to the head movement.

In conclusion, the optimized muscle activation scheme helped contextualize the neck muscle activation level and onset time through the identification of the sensitive parameters to impact, and the CMA scheme provided overall good correlation in all impact directions. The results from this work will enhance computational HBM that may better inform and develop preventions of injury to the head and neck during impact.

Acknowledgements

First, I would like to thank Dr. Duane Cronin for being always available to give a guiding word, academically or not, even with his tight schedule. He provided me with an opportunity to research at the University of Waterloo, funding to attend international conferences, the possibility to publish a journal paper and, most importantly, the chance to challenge myself.

Thanks to Dr. Stewart McLachlin for also giving me guidance, encouragement, and a different point of view, especially during the writing process.

I would like to show my appreciation for working with the Global Human Body Models Consortium (GHBMC), Honda R&D Americas, FCA Canada, GM Canada and NSERC. Specially Chin-Hsu Lin, Maika Katagiri, John Combest and Daniel Kim for their financial support and feedback throughout the project.

I would also like to thank my colleagues from the GHBMC and Orthotron groups who accepted me and were always ready to help. Special thanks to David Shen, Prasannaah Hadagali and Harish Rao to be ready at any time to give me a hand with any small trouble and also making me feel useful. Additional thanks to Jeffrey Barker and Donata Gierczycka for knowing everything about the neck model and giving relevant feedback with a surgeon`s precision. Thanks to Chi-Hsiang Liao for being great at coordinating gatherings for the group and introducing me to the Raptors at their best moment.

Finally, I would like to thank my family and friends for trusting in me and reminding me what is worth it. Special thanks to my close relatives for understanding why I am living so far away, although we miss each other.

Dedication

Dedicated to my parents for giving me a solid ground in our liquid modernity and to Dâmaris for making me still believe in a better future.

Table of Contents

Author's Declaration ii
Abstract iii
Acknowledgements v
Dedication vi
List of Figures x
List of Tables xv
List of Abbreviations xvi
Chapter 1 : Introduction 1
1.1 Research Motivation 1
1.2 Research Objectives 4
1.3 Thesis Organization 5
Chapter 2 : Background 6
2.1 Musculoskeletal Anatomy of the Human Neck 6
2.1.1 Neck Anatomy and Motion 6
2.1.2 Material Properties of the Neck Tissues 12
2.2 Muscle Activation Theory and Modeling 16
2.2.1 Passive Muscle Properties 16
2.2.2 Active Muscle Properties 17
2.2.3 Hill-Type Active Muscle Model 20
2.2.4 EMG Measurement of Active Muscle Response 22
2.2.5 Human Startle Response 24
2.3 Experimental Impact Studies involving Human Volunteers 25
2.3.1 Frontal Human Volunteer Sled Test Data 25
2.3.2 Lateral Human Volunteer Sled Test Data 29
2.3.3 Low Severity Human Volunteer Rear Impact Scenarios 32
2.4 Computational Human Body Models 35
2.5 Comparative Data Analysis through Correlation Ratings 41
2.6 Muscle Activation Optimization 42
Chapter 3 : Methods 44
3.1 Methodology Overview 44

3.2 Assessment of the Muscle Activation 47
3.2.1 Muscle Activation Schemes 49
3.2.2 Muscle Activation Onset Time 49
3.2.3 Muscle Activation Magnitude 49
3.3 Pre-optimization of Muscle Activation for Impact Simulations 50
3.3.1 Frontal Impact Activation Parameter Investigation 50
3.3.2 Lateral Impact Activation Parameter Investigation 52
3.3.3 Rear Impact Activation Parameter Investigation 53
3.4 Optimization of Muscle Activation for Impact Simulations 54
3.4.1 Optimization of Active Musculature for Frontal Impact Schemes 55
3.4.2 Optimization of Active Musculature for Lateral Impact Schemes 55
3.4.3 Optimization of Active Musculature for Rear Impact Schemes 56
3.5 Assessment of Model Response using Correlation Rating 56
Chapter 4 : Results 58
4.1 Frontal Impact Muscle Activation Strategy and Comparison to Experimental Data 58
4.1.1 Kinematic Sensitivity to Flexor Muscle Activation 58
4.1.2 Pre-optimization Study of Impact Kinematics 59
4.1.3 Frontal Impact Optimization Analysis 61
4.1.4 Optimized Frontal Impact Muscle Activation Parameters 65
4.1.5 Correlation of Frontal Impact Kinematics with Experimental Data 67
4.2 Lateral Impact Muscle Activation Strategy and Comparison to Experimental Data 68
4.2.1 Pre-optimization Study of Impact Kinematics 68
4.2.2 Lateral Impact Optimization Analysis 70
4.2.3 Optimized Lateral Impact Parameters 75
4.2.4 Correlation of Lateral Impact Kinematics with Experimental Data 77
4.3 Rear Impact Muscle Activation Strategy and Comparison to Experimental Data 78
4.3.1 Kinematic Sensitivity to Flexor Activation Onset Time 78
4.3.2 Pre-optimization Study of Impact Kinematics 79
4.3.3 Rear Impact Optimization Analysis 80
4.3.4 Optimized Rear Impact Parameters 81
4.3.5 Correlation of Rear Impact Kinematics with Experimental Data 82
Chapter 5 : Discussion 84

5.1 Muscle Activation in Frontal Impact Scenarios 84
5.2 Muscle Activation in Lateral Impact Scenarios 89
5.3 Muscle Activation in Rear Impact Scenarios 93
5.4 Cocontraction or Startle Muscle Activation Scheme 96
5.5 Study Limitations 97
5.6 Significance and Impact of the Study 99
Chapter 6 : Conclusions 100
Bibliography 102
Appendix A : Kinematics of the Frontal Impact Simulations 114
Appendix B : Kinematics of the Lateral Impact Simulations 123
Appendix C : Kinematics of the Rear Impact Simulations 127
Appendix D : Copyright Permission 129

List of Figures

Figure 2-1: Anatomical directions and planes of reference (Image adapted from: (Fehrenbach and Herring, 2016)). 6
Figure 2-2: Anatomical terminology of the head movements (Image from: (Schmitt et al., 2014)). 7
Figure 2-3: Top view of a typical vertebra with the main anatomical structures labelled (Image adapted from: (Gray, 1918)). 8
Figure 2-4: Top view of the C1 vertebra with the main anatomical structure labelled (Image from: (Gray, 1918))..... 8
Figure 2-5: View of the C2 vertebra with the main anatomical structures labelled (Image from: (Gray, 1918)). 9
Figure 2-6: A cross-section of the neck model at C5 showing the flexors in red and the extensors in blue. The head is pointing to the right. 10
Figure 2-7: Muscle structure at different levels (Image from: ("Skeletal muscle," 2019)). 11
Figure 2-8: The PCSA is presented in different muscles in green, and the anatomical cross-sectional area is displayed in blue (Image from: (Gille, 2007)). 12
Figure 2-9: Example of ligament distraction curve (Image from: (Robi et al., 2013)). 14
Figure 2-10: Relaxation of the shear modulus of the 3D passive element over time. 16
Figure 2-11: Sarcomere regions and contraction (Image adapted from:(Richfield, 2014)). 18
Figure 2-12: Contraction force in relation to muscle length. 19
Figure 2-13: Contraction force in relation to the velocity of the contraction. 20
Figure 2-14: Hill-type element (Imaged adapted from: (Hellmuth, 2010)). 21
Figure 2-15: Startle response stereotyped movement (Image from: (Yeomans et al., 2002)). 24
Figure 2-16: Average of the sled acceleration for the 8g frontal impact 26
Figure 2-17: Average of the sled velocity for the 8g frontal impact. 27
Figure 2-18: Average velocity in the X direction of the T1 in the 8g frontal impact experiments. 28
Figure 2-19: Average rotation of T1 in the Y direction for the 8g frontal impact experiments. 28
Figure 2-20: Average of the sled acceleration for the 7g lateral impact. 29
Figure 2-21: Average of the sled velocity for the 7g lateral impact. 30
Figure 2-22: Average velocity in the Y direction of the T1 in the 7g lateral impact experiments. 31
Figure 2-23: Average rotation of T1 in the X direction for the 7g lateral impact experiments. 31
Figure 2-24: Average of the sled acceleration for the 4g rear impact. 32

Figure 2-25: Average of the sled velocity for the 4g rear impact. 33
Figure 2-26: Average acceleration in the X direction of the T1 in the 4g rear impact experiments. ... 34
Figure 2-27: Average acceleration in the Z direction of the T1 in the 4g rear impact experiments. 34
Figure 2-28: Average rotation of T1 in the Y direction for the 4g rear impact experiments. 35
Figure 2-29: 1D Hill-type active muscle elements and 3D passive muscle tissue elements in the GHBMC neck model. 37
Figure 2-30: A) GHBMC 50th percentile male full human body model B) GHBMC 50th percentile male full detailed head C) GHBMC 50th percentile male simplified head 38
Figure: 2-31 Neuronal impulse and equivalent activation level curve for a 100 ms neuronal impulse starting at 74 ms. 39
Figure 2-32: Differences of phase (A) size (B) and shape (C) responses (Image adapted from: (Thunert, 2017)). 42
Figure 3-1: Steps of the muscle activation optimization. 45
Figure 3-2: Example of experimental average and standard deviation (corridors) for head rotation in 8g frontal impact. 46
Figure 3-3: GHBMC M-50 muscles grouped in quadrants. 48
Figure 3-4: Frontal impact optimization direction of the kinematic parameters. The displacement and acceleration in the green directions were the objectives of the optimization. 51
Figure 3-5: Lateral impact optimization direction of the kinematic parameters. The displacement and acceleration in the green directions were the objectives of the optimization. 52
Figure 3-6: Rear impact optimization direction of the kinematic parameters. The displacement and acceleration in the green directions were the objectives of the optimization. 53
Figure 3-7: Frontal impact optimization process based on the LS-OPT user interface. 55
Figure 4-1: Different activation levels for the flexors with a constant activation level of 10% for the extensors in the 8g frontal impact. 58
Figure 4-2: Different activation levels for the flexors with a constant activation level of 10% for the extensors in the 2g frontal impact. 59
Figure 4-3: Correlation rating to the experimental data for different muscle activation schemes for frontal impacts ranging from 2g to 15g. 61
Figure 4-4: Response surfaces of X-displacement (left plot) and Y-rotational displacement (right plot) for the 2g frontal impact optimization. The black dot represents the optimum response. 62

Figure 4-5: Response surfaces of X-displacement (left plot) and Y-rotational displacement (right plot) for the 8g frontal impact optimization. The black dot represents the optimum response. 62
Figure 4-6: Response surfaces of X-displacement (left plot) and Y-rotational displacement (right plot) for the 15g frontal impact optimization. The black dot represents the optimum response. 63
Figure 4-7: Response surfaces of the X-acceleration (left plot) and Y-rotational acceleration (right plot) for the 2g frontal impact optimization. The black dot represents the optimum response..... 63
Figure 4-8: Influence of each optimization parameter in the Y-rotational displacement for the 2g frontal impact simulation. 64
Figure 4-9: Influence of each optimization parameter in the Y-rotational displacement for the 8g frontal impact simulation. 64
Figure 4-10: Influence of each optimization parameter in the Y-rotational displacement for the 15g frontal impact simulation. 64
Figure 4-11: Optimized extensor muscle activation level demonstrating increasing trend in activation with increasing frontal impact severity. 66
Figure 4-12: Optimized extensor muscle activation onset time. 67
Figure 4-13: Correlation of muscle activation strategies to the experimental data for rear impacts ranging from 2g to 15g. 68
Figure 4-14: Correlation to the experimental data for different muscle activation schemes for lateral impacts ranging from 4g to 7g. 70
Figure 4-15: Response surfaces of X-rotational displacement (A), X-rotational acceleration (B) Y-rotational displacement (C), Y-rotational acceleration (D), Z-rotational displacement (E), and Z-rotational acceleration (F) for left extensors in 3 iterations of the 4g frontal impact optimization. The black dot represents the optimum response. 71
Figure 4-16: Influence of each optimization parameter on the Y-rotational displacement for the 4g lateral impact simulation 72
Figure 4-17: Influence of each optimization parameter on the Y-rotational acceleration for the 4g lateral impact simulation 73
Figure 4-18: Influence of each optimization parameter on the X-rotational displacement for the 4g lateral impact simulation 74
Figure 4-19: Influence of each optimization parameter on the X-rotational acceleration for the 4g lateral impact simulation 74
Figure 4-20: Optimized muscle groups activation level trends in lateral impact severity 76

Figure 4-21: Optimized muscle groups activation onset time trends in lateral impact severity 76
Figure 4-22: Correlation of muscle activation strategies to the experimental data for lateral impacts ranging from 4g to 7g. 77
Figure 4-23: Y-rotational displacement of the head center of gravity for different flexor activation onset times, with a constant activation level of 20% for the extensors in the 3g rear impact. 79
Figure 4-24: Response surfaces of the X-displacement (left plot) and Y-rotational displacement (right plot) for the 3g rear impact optimization. The black dot represents the optimum response. 80
Figure 4-25: Influence of each optimization parameter in the Y-rotational displacement for the 3g rear impact simulation. 81
Figure 4-26: Correlation of muscle activation strategies to the experimental data for rear impacts ranging from 3g to 4g. 82
Figure 5-1: Predicted trabecular bone failure (purple) in C6 for the 15g frontal impact. 87
Figure 5-2: Maximum flexion of the model during the 8g front impact (blue line) for MMA (A), CMA (B) and OMA (C). The average maximum head rotation of the 8g sled test is presented as black lines. 88
Figure 5-3: Head position after 250 ms in the 7g lateral right side-impact (head X-rotational displacement of the model in blue) for the MMA (A) and the OMA (B). The average head X-rotational displacement of the 7g sled test after 250 ms is presented as black lines. 90
Figure 5-4: Predicted odontoid process and C6 trabecular bone failure (purple) in the 7g lateral impact. 92
Figure 5-5: Maximum angular displacement of the head for the MMA 3g rear impact (A), OMA 3g rear impact (B), MMA 4g rear impact (C), and OMA 4g rear impact (D). 95
Figure 5-6: Idealized curvature of the spine during a rear impact (top) and simulated result for the CMA 4g rear impact (bottom). (Adapted from (Stemper and Corner, 2016)) 98
Figure 6-1: Head center of gravity kinematics for the 2g frontal impact in the global coordinate system for all plots except for the linear displacements that are in the local T1 coordinate system. . 114
Figure 6-2: Head center of gravity kinematics for the 3g frontal impact in the global coordinate system for all plots except for the linear displacements that are in the local T1 coordinate system. . 115
Figure 6-3: Head center of gravity kinematics for the 6g frontal impact in the global coordinate system for all plots except for the linear displacements that are in the local T1 coordinate system. . 116
Figure 6-4: Head center of gravity kinematics for the 8g frontal impact in the global coordinate system for all plots except for the linear displacements that are in the local T1 coordinate system. . 117

Figure 6-5: Head center of gravity kinematics for the 10g frontal impact in the global coordinate system for all plots except for the linear displacements that are in the local T1 coordinate system.. 118
Figure 6-6: Head center of gravity kinematics for the 12g frontal impact in the global coordinate system for all plots except for the linear displacements that are in the local T1 coordinate system.. 119
Figure 6-7: Head center of gravity kinematics for the 13g frontal impact in the global coordinate system for all plots except for the linear displacements that are in the local T1 coordinate system.. 120
Figure 6-8: Head center of gravity kinematics for the 14g frontal impact in the global coordinate system for all plots except for the linear displacements that are in the local T1 coordinate system.. 121
Figure 6-9: Head center of gravity kinematics for the 15g frontal impact in the global coordinate system for all plots except for the linear displacements that are in the local T1 coordinate system.. 122
Figure 6-10: Head center of gravity kinematics for the 4g lateral impact in the global coordinate system. 123
Figure 6-11: Head center of gravity kinematics for the 5g lateral impact in the global coordinate system. 124
Figure 6-12: Head center of gravity kinematics for the 6g lateral impact in the global coordinate system. 125
Figure 6-13: Head center of gravity kinematics for the 7g lateral impact in the global coordinate system. 126
Figure 6-14: Head center of gravity kinematics for the 3g rear impact in the global coordinate system for all plots except for the linear displacements that are in the local T1 coordinate system..... 127
Figure 6-15: Head center of gravity kinematics for the 4g rear impact in the global coordinate system for all plots except for the linear displacements that are in the local T1 coordinate system..... 128

List of Tables

Table 2-1: Failure criteria for the ligaments of the lower cervical spine. 14
Table 2-2: Classification of the correlation rating. 42
Table 3-1: Flexor and extensor muscle groups 48
Table 4-1: Pre-optimized muscle activation level for varying frontal impact severity. 60
Table 4-2: Optimized extensor muscle activation level and activation onset time for each frontal impact case (flexors level at 100% and onset time at 74 ms). 65
Table 4-3: Pre-optimization activation levels for varying lateral impact severity. 69
Table 4-4: Optimized muscle activation level and onset time for each lateral impact severity 75
Table 4-5: Pre-optimization activation levels for two rear impact cases 79
Table 4-6: Optimized extensor muscle activation level for the two rear impact cases (activation onset times at 74 ms). 81

List of Abbreviations

Gp, Gv, Gs: Cross-correlation constants 57
a: Muscle activation magnitude 22
ATD: Anthropometric Testing Device 1
C: Corridor rating 57
CE: Contractile element 21
CMA: Cocontraction Muscle Activation 49
EMG: Electromyography 2
f: Fibre 21
F: Force 21
FE: Finite Element 3
G: Shear modulus 16
GHBMC: Global Human Body Models Consortium 4
HBM: Human Body Model 3
JAMA: Japan Automobile Manufacturers Association model 3
KTH: Royal Institute of Technology model 3
l: change in length 21
MMA: Maximum Muscle Activation 49
MVC: Maximum Voluntary Contraction 22
NBDL: Naval Biodynamics Laboratory 2
NHTSA: National Highway Traffic Safety Administration 2
NMA: No Muscle Activation 49
OMA: Optimized Muscle Activation 49
P: Phase rating 57
PCSA: Physiologic Cross-Sectional Area 11
PE: Parallel element 21
PMHS: Post Mortem Human Subject 1
S: Size rating 57
SE: Series element 21
t: time 16
THUMS: Total Human Model for Safety 3

u: Neuronal input 40
V: Shape Rating 57
δ: Non-dimensional quantity proportional to the strain 22
ε: Strain 16
λ_f: Fibre stretch 22
σ: Stress 16

Chapter 1: Introduction

1.1 Research Motivation

Muscle activation affects the risk of injury to the neck, stiffening the spinal column when an internal or external load is applied to the body (Stemper and Corner, 2016). Muscle activation can broadly be described by the muscle activation level and the time of activation. In addition, dynamic movement and stabilization of the head-neck system are primarily controlled by activation of the cervical (neck) musculature enclosing the spinal column (Olszko et al., 2018). However, a more in-depth understanding of muscle activation and its role in head and neck response during impact is needed. This knowledge is crucial to develop improved strategies to mitigate the large number of head and neck injuries, which occur annually from motor vehicle accidents. Neck and back strains and sprains are related to approximately 25% of the four million annual emergency room visits from motor vehicle traffic injuries in the United States (Albert and McCaig, 2015).

The role of cervical muscle activation on head and neck injury risk in motor vehicle accidents has been investigated but has not been quantified. Stemper and Corner (2016) observed that cervical injury symptoms, time to recover, pain intensity and injury risk were reduced when a person subjected to a vehicle impact was pre-aware of the collision, indicating the importance of muscle activation in terms of bracing prior to impact (Hendriks et al., 2005; Sturzenegger et al., 2012). In contrast, other clinical studies have reported no correlation between injury symptoms and pre-awareness (Walton et al., 2013). Post-mortem human subjects (PMHS) and anthropometric testing devices (ATD) cannot represent physiologic muscle activation, creating challenges for vehicle safety tests that commonly use these methods to assess injury (Arbogast et al., 2009; Iwamoto, 2018; Stemper and Corner, 2016). As occupants in real crash scenarios could have their kinematic response altered by muscle activation,

vehicle safety tests may be limited when extrapolating post-mortem results to those of human volunteers (Albert et al., 2018).

A number of experimental studies have investigated car and sled tests with volunteers in low severity (1g to 4g) autonomous braking and impacts (1g to 4g) and reported the effect of muscle activation on the response (Carlsson et al., 2010; Dehner et al., 2013; Fanta et al., 2013; Hedenstierna et al., 2009; Kumar et al., 2002, 2004a, 2004b; Mathews et al., 2013; Ólafsdóttir et al., 2013; Siegmund et al., 2007). Relevant conclusions have included an observed increase in the neck muscle activation during impacts, a higher angular head rotation for females during impacts, as well as challenges in terms of measuring muscle activation magnitudes using normalized electromyographic (EMG) data. Further, many of these studies have not reported important experimental boundary conditions (*i.e.*, seat inclination, presence of headrest, etc.), making it difficult to reproduce the experiments in a simulation environment or to quantify the effects of muscle activation.

A key experimental dataset containing higher severity volunteer impacts has been made available through the National Highway Traffic Safety Administration (NHTSA) database ("National Highway Traffic Safety Administration," 2012). This work presented results from a series of sled tests with human volunteers, conducted by the Naval Biodynamics Laboratory (NBDL). The head and neck kinematic data were collected from 16 volunteers subjected to 119 frontal and 72 lateral impact sled tests (Thunnissen et al., 1995; Wismans et al., 1986). The experimental data was consistent for a range of impact levels, from 2g to 15g, owing to the restraint system used in the experiments. A limitation of the experimental data was that no measurements of the volunteer's muscle activation were recorded during the impact tests, as well as no assessment of rear impacts. There is a scarcity of higher severity rear impact studies owing to volunteer injury risk. The limited data available for this impact scenario is primarily a series of 3g and 4g sled tests (Ono et al., 1997; Sato et al., 2014). These experiments used

12 human volunteers and did not incorporate a headrest in the seat. Similar to the NBLD database, no muscle activation was recorded during the tests.

Computational Human Body Models (HBMs) can complement experimental data to assess injury risk during impact by helping fill knowledge gaps in areas difficult to gather experimental measurements. Neck muscle activation has been examined in the Finite Element (FE) HBMs including the GHBMC, Royal Institute of Technology model (KTH), Japan Automobile Manufacturers Association model (JAMA), Total Human Model for Safety (THUMS), and simTK models (Brolin et al., 2005; Ejima et al., 2005; Iwamoto et al., 2012; Vasavada et al., 1998). A significant benefit of HBM is the potential to evaluate injury risk in complex impact scenarios without the ethical and practical challenges of human volunteers (Dibb et al., 2013). Considering contemporary HBM, only the GHBMC and THUMS models incorporate a combination of skin, adipose tissue, 3D passive muscles and active 1D muscles. The soft tissues are relevant for the head and neck kinematics because of the increase in stiffness of the system resulting from these tissues. At present, active musculature models have focused only on a small number of lower severity events when validating against volunteer studies. Thus, there is a need for improved understanding of muscle activation schemes over a wider range of impact severities.

In general, current active musculature implementations in HBMs use pre-defined activation parameters, also called open-loop control. However, these models could benefit from the automation of the activation parameters (closed-loop control) that could allow the models to adapt to different impact scenarios. This potential benefit has resulted in an increased interest in implementing these algorithms in the models (Östh et al., 2015). Still, many HBMs are calibrated only to specific experimental and loading cases due to the lack of electromyography data in high severity impacts (>8g).

To date, there has been no study analyzing the effects of active neck musculature over a range of low to high impact severities; although some studies have presented optimizations of the muscle activation for other scenarios (Dibb et al., 2013; Ivancic and Pradhan, 2017; Mortensen et al., 2018). The M50-O v4.5, 50th percentile, Global Human Body Models Consortium (GHBMC) HBM, used in the present study, includes 1D Hill-type elements representing the active portion of the muscles and 3D solid hexahedral elements with a hyperelastic material constitutive model representing the passive response of the muscle; however, the effect of various activation schemes of the neck muscles on the impact response has not yet been investigated.

1.2 Research Objectives

The overall objective of this thesis was to develop activation schemes for the cervical muscles to improve the resulting head kinematics of the model over a wide range of impact severities and directions. Within this objective, the main goals were to: (1) define optimal activation schemes for each impact scenario that maximized the correlation of head kinematics to experimental data and (2) identify a possible single muscle activation scheme that generated appropriate head kinematics for all impact cases.

Based on the defined objectives, it was hypothesized that the muscle activation schemes could be optimized to approximate head kinematics of human volunteers in sled impacts by modifying the muscle activation level and timing of the model. In addition, based on known head reflex mechanisms, possible candidates of a unique activation scheme could be compared over a range of impact severities using the average correlation for all the impact severities considered in this study. Further, with this approach, the degree of influence of the activation variables on the head response could be obtained from the optimization process to better inform future studies of the effects of active muscle in impacts.

1.3 Thesis Organization

Chapter 2 expands on the necessary background information, presenting information on cervical muscle properties such as anatomy, material properties, activation parameters, the Hill-type model implementation, and the 3D passive muscle in the model. Also, the available experimental data with human volunteers for impact studies are summarized in this section, including the startle response mechanism. Existing computational HBMs for the cervical spine with active musculature are also discussed. Chapter 3 describes the research methodology. The methodology includes the assessment of the muscle activation parameters in the literature, and the application of these parameters to the muscle groups. A series of pre-optimization simulations were undertaken, enabling the definition of the optimization procedure, and the optimized results were assessed through cross-correlation with the experimental data. Chapter 4 describes the results of the simulations for the different activation schemes in frontal, lateral and rear impacts, as well as the information obtained from the optimization process. Chapter 5 presents a discussion of the results, including a comparison of the muscle activation schemes with experimental data, relation to muscle reflex mechanisms and muscle activation schemes comparison. Chapter 6 presents the research conclusions, limitations and future research.

Chapter 2: Background

2.1 Musculoskeletal Anatomy of the Human Neck

2.1.1 Neck Anatomy and Motion

The human neck comprises the cervical spine (ligaments, intervertebral discs and vertebrae), musculature, skin, and flesh (adipose tissue). The anatomy of the head and neck are described with respect to three reference planes: frontal, median and transverse (Betts et al., 2013) (Figure 2-1). The anatomical directions are used with the aforementioned anatomical reference planes to describe the location and motion of the body segments. The directions are the anterior, posterior, superior, inferior, lateral, medial, proximal, distal, superficial and deep (Betts et al., 2013).

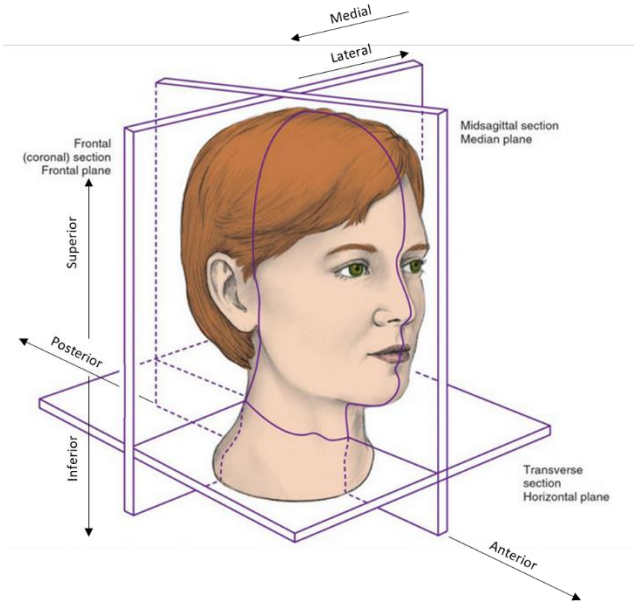

Figure 2-1: Anatomical directions and planes of reference (Image adapted from: (Fehrenbach and Herring, 2016)).

The motion of the head and neck can be classified as flexion, extension, lateral flexion, and rotation (Figure 2-2). The term flexion describes the anterior bending of the neck while extension describes the posterior bending of the neck. The lateral flexion describes the left and right bending of the head in the transverse plane, and rotation describes the left and right twisting movement in the frontal plane (Betts et al., 2013).

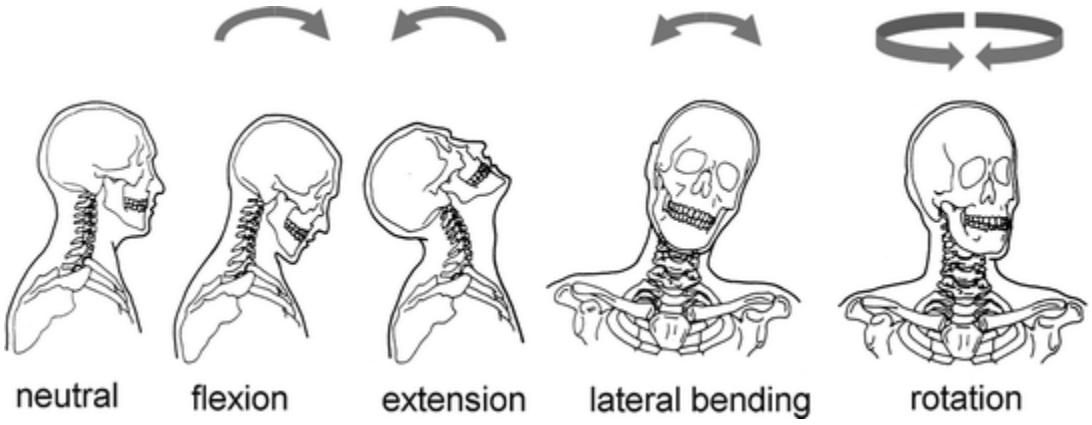

Figure 2-2: Anatomical terminology of the head movements (Image from: (Schmitt et al., 2014)).

The cervical spine is composed of seven vertebrae (C1to C7) in the inferior direction divided into the upper (C1 and C2) and lower (C3 to C7) cervical spine. The range of motion of the cervical spine for flexion is 80° to 90°, for extension is 70°, for lateral bending is 20° to 45°, and for axial rotation for each side is 90° (Swartz et al., 2005). The vertebrae are composed of the vertebral body anteriorly and by the vertebral arch posteriorly. The arch surrounds the vertebral foramen at the spinal cord location. The vertebral arch consists of a pair of pedicles and a pair of laminæ, and supports four articular processes, two transverse processes, and one spinous process (Figure 2-3). The C1 and C2 are different from the other vertebrae. The first vertebra (C1) has no vertebral body and no spinous process (Figure 2-4). A distinct characteristic of the second vertebra (C2) is the odontoid process or dens, which rises perpendicularly from the upper surface of the body, about which the C1 vertebra rotates. (Figure 2-5).

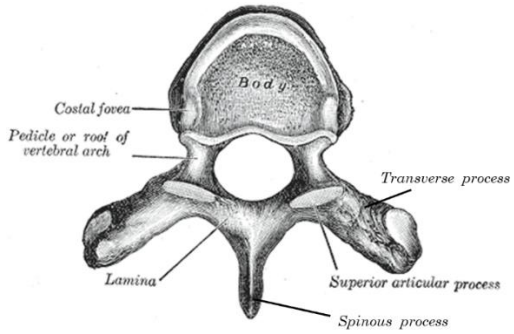

Figure 2-3: Top view of a typical vertebra with the main anatomical structures labelled (Image adapted from: (Gray, 1918)).

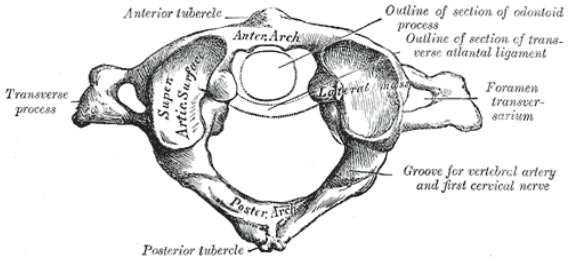

Figure 2-4: Top view of the C1 vertebra with the main anatomical structure labelled (Image from: (Gray, 1918)).

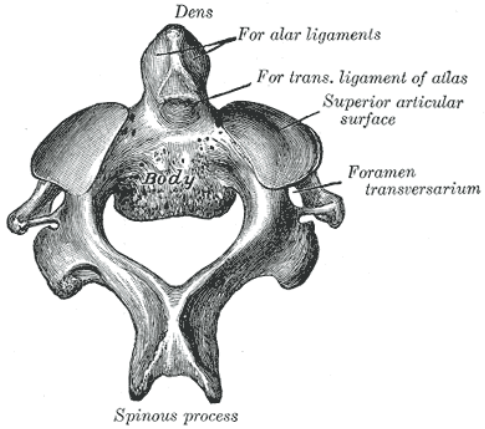

Figure 2-5: View of the C2 vertebra with the main anatomical structures labelled (Image from: (Gray, 1918)).

The C1 vertebra, also named atlas, allows for flexion and extension of the skull with the occipital condyle articulation. The articulation is restrained to rotation and lateral flexion due to the reduced space of the joint. The C2 vertebra, also named axis, is connected to C1 through the odontoid process and stabilized by the transverse, alar and apical ligaments (Swartz et al., 2005). The C1-C2 articulations are not restricted to lateral bending and rotation. Further, the C1-C2 flexion and extension motions are often in the opposite direction of the atlas movement due to the geometry of the atlantoaxial articulation (Swartz et al., 2005). Another important fact is the upper cervical spine rotation coupling with extension, flexion and/or lateral bending. Similarly, the lower cervical spine vertebral rotation is always associated with extension, flexion and/or lateral bending because of the shape of the articulations. However, the lateral-flexion movement of the lower cervical spine is only possible with the rotation of the vertebrae while, in the upper cervical spine, it can occur without rotation (Swartz et al., 2005). In summary, the movement in the cervical spine is complex, and the global motion of the head and neck does not necessarily reflect the action of the individual vertebrae in the cervical spine.

The muscles of the neck can contract and transmit force to the bones enabling motion of the neck. The muscles present sagittal symmetry and are often classified as flexors or extensors (Figure 2-6). The grouping in flexors and extensors is a simplification since a single muscle can extend or flex the neck depending on posture and the action of other muscles. Muscles are hierarchical structures composed of groups of muscle fibres called fascicles; the muscle fibres are composed of parallel bundles of myofibrils, which consist of contractile units, sarcomeres, in series (Figure 2-7).

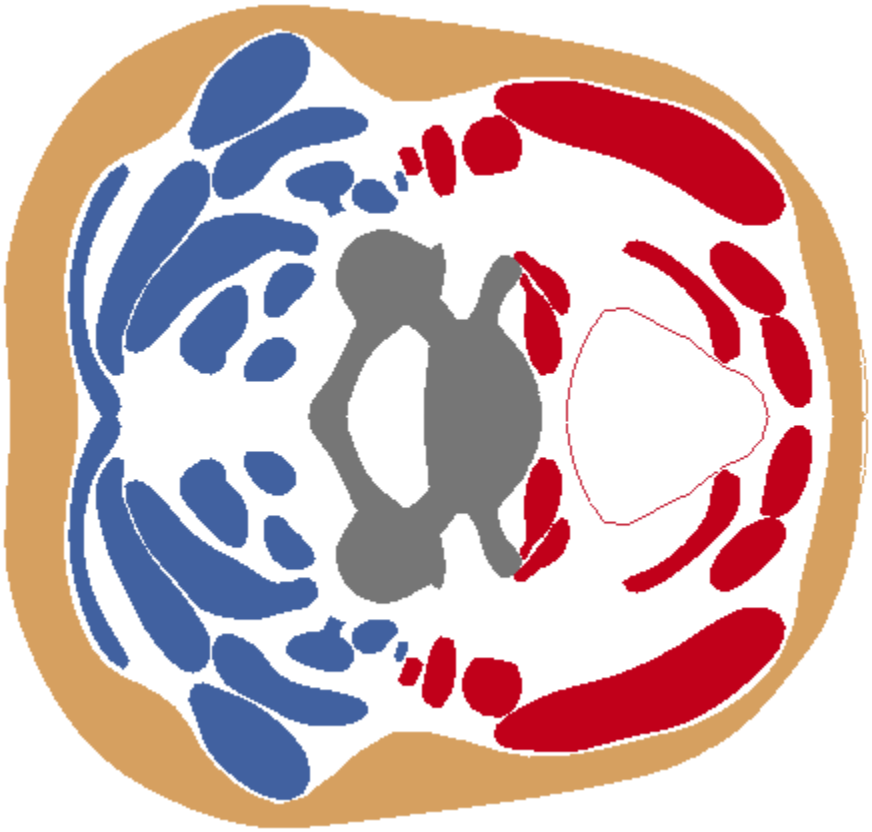

Figure 2-6: A cross-section of the neck model at C5 showing the flexors in red and the extensors in blue. The head is pointing to the right.

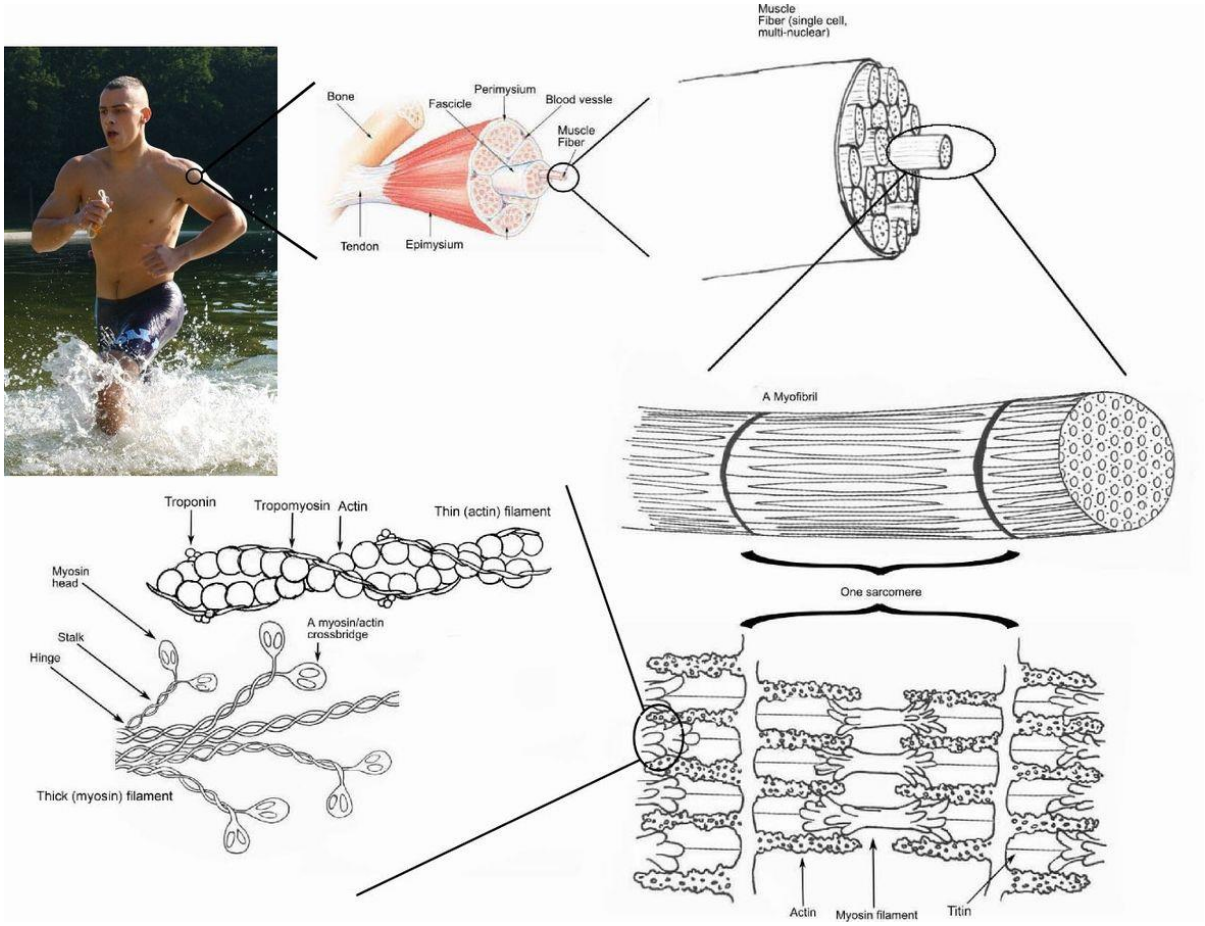

Figure 2-7: Muscle structure at different levels (Image from: ("Skeletal muscle," 2019))**.**

The direction of the force exerted by the muscle contraction takes place along the length of the muscle fibres and can occur along a straight line between the two points of insertion if the fibres. However, the muscle path may follow a curve due to ligament attachments and boney structures (Gray, 1918).

The maximum force exerted by a muscle is proportional to the number of fibres in the Physiologic Cross-Sectional Area (PCSA) (Figure 2-8), in other words, the perpendicular section crossing through the maximum number of fibres within a muscle (Gray, 1918). The number of fibres is also related to the volume of the muscles. For example, the sternocleidomastoid is the strongest flexor

in the neck, representing 43% of the volume of this muscle group, and the strongest extensor is the trapezius, which represents 44% of the size of the muscle group.

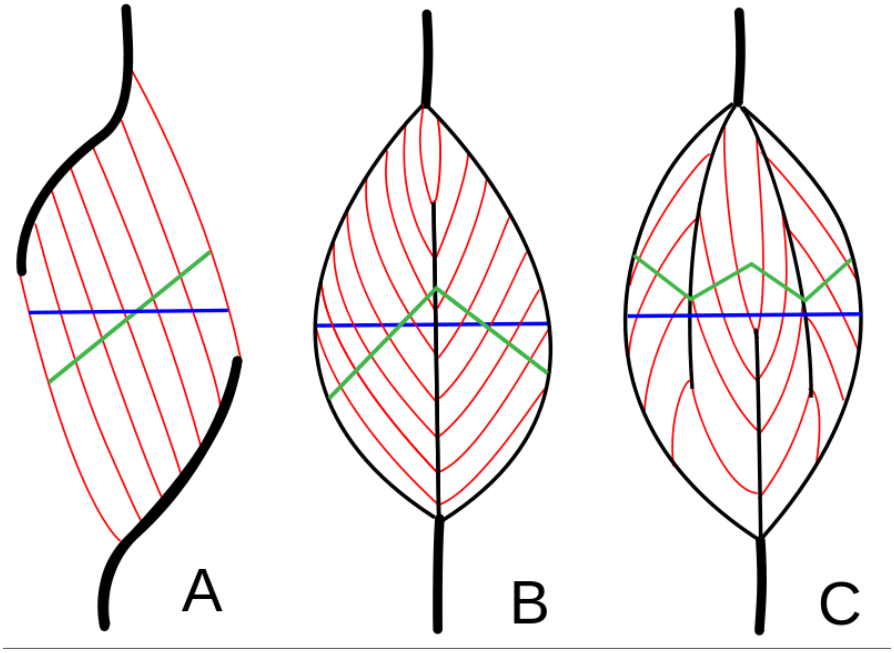

Figure 2-8: The PCSA is presented in different muscles in green, and the anatomical cross-sectional area is displayed in blue (Image from: (Gille, 2007)).

2.1.2 Material Properties of the Neck Tissues

There are many tissues that contribute to the mechanical response of the neck in impact scenarios, including the hard tissues or bones, cartilage, ligaments, intervertebral discs (annuli fibrosi, nuclei pulposi, ground substance), muscle, skin and adipose tissue.

The hard tissues are classified as cortical or cancellous, according to the density and structure of the bone. Cortical bone has a high density and occurs as a thin shell around the vertebra in the neck (Martin et al., 2015). Cancellous or trabecular bone is found inside the vertebrae, and it is composed of slender filaments called trabeculae with spaces among them (Martin et al., 2015).

Both bone types are composed mainly of hydroxyapatite mineral (Martin et al., 2015) with an organic matrix of collagen fibres (Cowin, 2001). The microstructure of the cortical bone is formed by formations called lamellae, composed of mineralized collagen fibres and by structures called osteons, composed by longitudinal blood vessels, lymphatic nerves, and loose connective tissue surrounded by rings of concentric lamellae connecting to the bone marrow and periosteum (Cowin, 2001). The trabecular bone microstructure is similar to the cortical bone, but it is arranged in filaments of lamellar bone with a characteristic orientation that defines the mechanical stiffness and strength of the material. The cancellous bone is anisotropic due to the directionality of the filaments. The trabecular bone has a behaviour that depends on time as most biological tissues, but it is highly heterogenic. The heterogeneity is resultant of a diversity of volume fraction, geometry and even tissue properties, varying the global material properties (Keaveny et al., 2001).

The cortical bone presents a low ductility material stress-strain curve, and the peak stress (or its related bending moment) can be used to define the limits of the material before fracture initiates. The crack propagation is directly related to the microstructures of the bone. Where the osteons lengths are parallel to the length of the impacted region, the crack initiation and propagation occur in the direction of the osteons because the interface between these systems and the matrix creates a weaker path (Nalla et al., 2003). However, in the opposite case, the cracks are perpendicular to the short axis of the osteons (Nalla et al., 2003). The trabecular bone, although complex, also presents a simple way to determine failure as it exhibits a strong linear correlation between the maximum stress and the corresponding elastic modulus, suggesting that the failure strains for trabecular bone are relatively constant. Compression experiments with cadavers determined that the maximum strain for the failure of the cortical bone is 0.0178, and trabecular bone is 0.095 (Keaveny et al., 2001; Lindahl, 1976; McElhaney, 1966).

Ligaments connect two points in the body resisting tension forces. The experiments usually measure the force and corresponding ligament distraction and indicate three regions from no load to peak load: the toe region, linear region, and traumatic region (Figure 2-9) (Yang et al., 2018). In the first region, the stiffness increases as the folded collagen fibres are unravelled. In the second region, the stiffness can be considered constant as the straight fibres are parallel to the loading (Yang et al., 2018). The last region presents a sudden reduction of the ligament stiffness as individual fibres tear gradually until the complete rupture of the ligament (Yang et al., 2018).

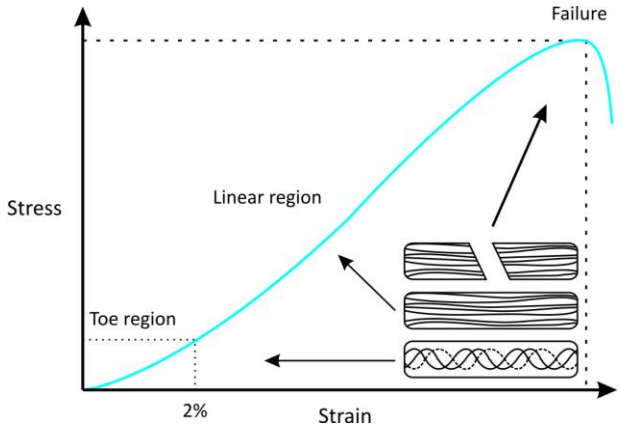

Figure 2-9: Example of ligament distraction curve (Image from: (Robi et al., 2013)).

The average experimental curves were obtained by fitting data of a series of tests until the failure of the cervical ligaments. The tests measured the distance between the bone regions where the ligaments were inserted (distraction) while applying traction. From these tests, the average failure distractions could be defined for each ligament (Table 2-1) (Mattucci et al., 2012; Mattucci and Cronin, 2015).

Table 2-1: Failure criteria for the ligaments of the lower cervical spine.

	Average failure distraction (mm)			Standard deviation (mm)		
Ligament	C2 to C4	C4 to C6	C6 to T1	C2 to C4	C4 to C6	C6 to T1
Anterior Longitudinal Ligament	3.8	3.3	4.2	2.8	2.2	3.3

Posterior Longitudinal Ligament	3.3	2.8	2.8	2.1	1.9	1.7
Capsular Ligament	4.0	4.9	5.1	2.5	3.0	2.7
Ligamentum Flavum	4.5	5.5	7.5	2.6	3.5	4.7
Interspinous Ligament	5.9	6.6	8.1	3.4	3.4	4.1

The complex structure of the IVD assists loading transmission and range of motion between vertebrae. It is comprised of the nucleus and annulus fibrosus. The nucleus is located in the center of the disk and can be considered elastic viscous fluid (Yang et al., 2018). The annulus surrounds the nucleus and is composed of a concentric lamina of fibres embedded in a homogeneous matrix called ground substance (Yang et al., 2018). The ground substance is made mainly of water and proteins, and a strain-energy function can represent the mechanical properties (Yang et al., 2018). The embedded annulus fibrosus can be represented by layers with an anisotropic elastic material model (Yang et al., 2018).

The skin and flesh are the superficial tissues that cover almost all the human body. The skin is composed of three regions: epidermis, dermis and hypodermis. The epidermis is the most superficial layer, and with the dense fibrous tissue of the dermis, form the cutis (Joodaki and Panzer, 2018). The third layer is the hypodermis, also called flesh in this thesis, composed mainly of adipose cells.

The mechanical response of the skin is non-linear due to the heterogeneity of the constituents. Similar to the ligaments, the fibres are initially folded, and at tensile strains around 30%, they are straightened, highly increasing the stiffness (Joodaki and Panzer, 2018). For higher strains, the stiffness increases rapidly as more collagen fibres are straightened. Continuing increasing the strain will make the tissue reach a peak tension and gradually fail due to the fibres rupture. Skin also exhibits the relaxation behaviour characteristic of viscoelastic materials and, due to the direction of the fibres, anisotropy (Joodaki and Panzer, 2018). In a living person, the skin is normally in a state of tension, contracting when excised (Joodaki and Panzer, 2018).

2.2 Muscle Activation Theory and Modeling

2.2.1 Passive Muscle Properties

The mechanical behaviour of the sarcomeres and connective tissue penetrating the muscle are viscoelastic and isotropic, as expected for most biological tissues (Anderson et al., 2002; Bensamoun et al., 2006; Meyer et al., 2011; Toursel et al., 2002). In other words, the stress (σ_{ij}) and strain (ε_{kl}) relation depends on time (t). The mechanical behaviour of these passive tissues has been modelled using a linear-viscoelastic formulation as the Ogden Rubber (Equation 1) (Hedenstierna et al., 2008).

$$\boldsymbol{\sigma_{ij} = \int_0^t G_{ijkl}(t-\tau)\,(\partial \varepsilon_{kl}/\partial \tau)\,d\tau} \quad \textbf{(1)}$$

The shear modulus G(t) in the formulation is obtained through relaxation curves (Figure 2-10) that are defined by the terms from the Prony series (Equation 2), which make this model a Maxwell fluid, which means it consists of dampers and springs in series (Livermore Software Technology Corporation, 2016).

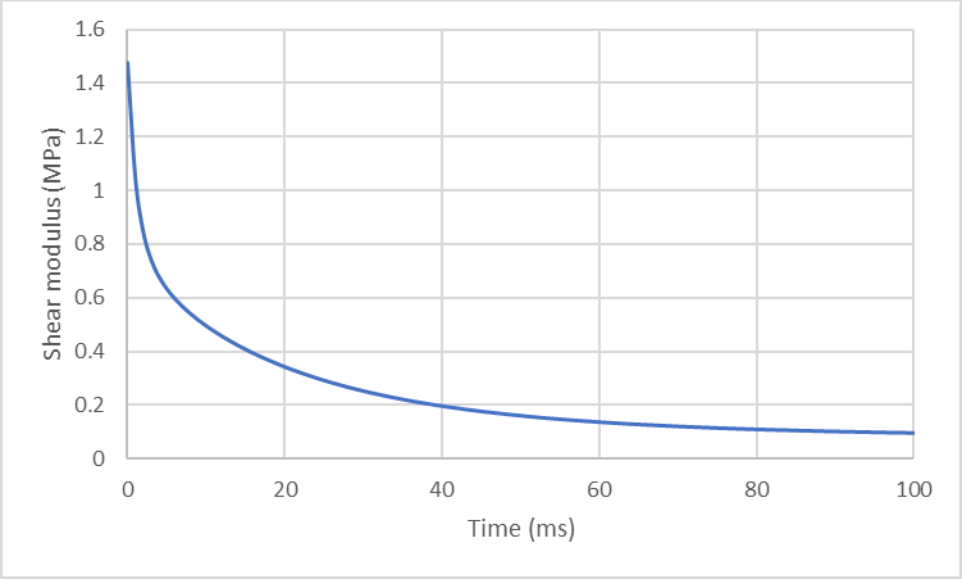

Figure 2-10: Relaxation of the shear modulus of the 3D passive element over time.

$$\mathbf{G(t)} = \sum_{i=1}^{n} \boldsymbol{G_i e^{-\beta_i t}} \quad \textbf{(2)}$$

This implementation is isotropic, though the muscles are anisotropic due to the defined direction of the muscle fibres. Some anisotropic formulations have been studied; however, the current detailed HBMs implement that property with additional beam elements in the direction of the fibres or use only the isotropic material (Alizadeh et al., 2020; Khodaei et al., 2013). In addition, beam elements can be used as support to connect the muscles to the cervical spine, maintaining the physiological pathway of the contraction.

2.2.2 Active Muscle Properties

The contraction of a muscle is controlled by nerve impulses originating in the central nervous system and transmitted through motor neurons to the actuating cells. In response to this stimulus, the contraction is developed by the intracellular structure, called sarcomeres, through sliding filaments of actin and myosin parallel to the longer dimension of the muscle fibres. The actin filaments are thin and localized in a parallel array at the Z-disk, and the myosin filaments are thick and localized at the A-band (Figure 2-11). The I-band is the region connecting two sarcomeres with the Z-disk in its middle, the A-band connects myosin filaments between the I-bands, and the H-zone is the region without superposition between actin and myosin (Mukund and Subramaniam, 2020). The contraction of the sarcomere is produced by the conformational change of a chemical structure formed with myosin. After spending stored energy, the thin and thick filaments overlap by binding and sliding (Mukund and Subramaniam, 2020).

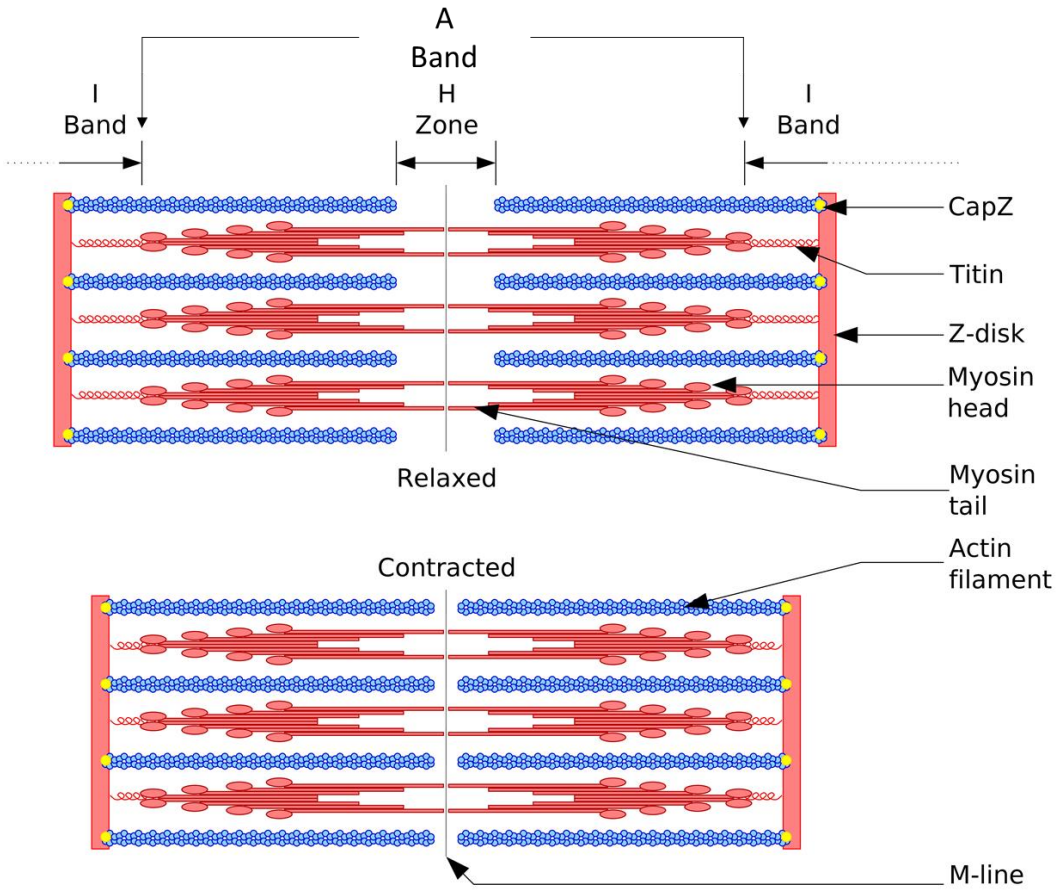

Figure 2-11: Sarcomere regions and contraction (Image adapted from:(Richfield, 2014)**).**

The chemical structure of the sarcomeres has other proteins that are also relevant in understanding the mechanical characteristics of the muscle cells. Titin is an elastic protein that ensures an equal force is developed at both sides of the sarcomere extending from the Z-disk along the myosin filaments (Mukund and Subramaniam, 2020). The titin molecule is suggested to define the length and conformation of the myosin filaments, which is directly related to the passive and active properties of the muscles at a cellular level (Mukund and Subramaniam, 2020). The nebulin molecules display a similar function for the actin filaments (Mukund and Subramaniam, 2020). Myomesin, located at the M-band, is suggested to function as a strain sensor also related to the myocyte (muscle cell) contraction activation (Mukund and Subramaniam, 2020). Furthermore, other molecules like troponin and

tropomodulin are fundamental for the enzymatic reactions responsible for the movement of the structure of the sarcomeres (Mukund and Subramaniam, 2020).

Experiments of stretching and shortening a muscle to different lengths were used to determine the relationship between muscle forces and lengthening (Gasser and Hill, 1924; Gordon et al., 1966; Winters and Stark, 1985) (Figure 2-12). In the tests, an isometrically clamped fully activated muscle was released to determine the relationship between muscle force and velocity of contraction (Figure 2-13).

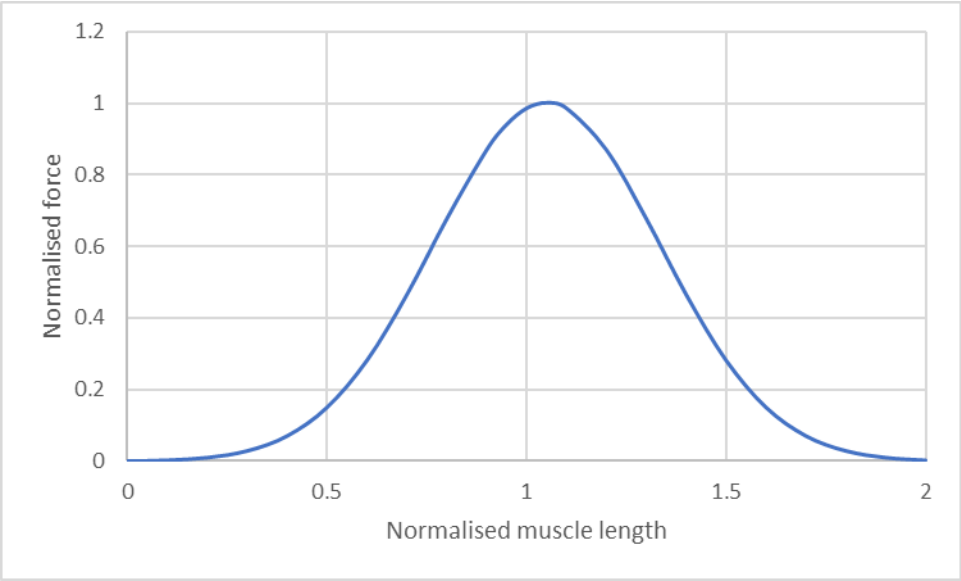

Figure 2-12: Contraction force in relation to muscle length.

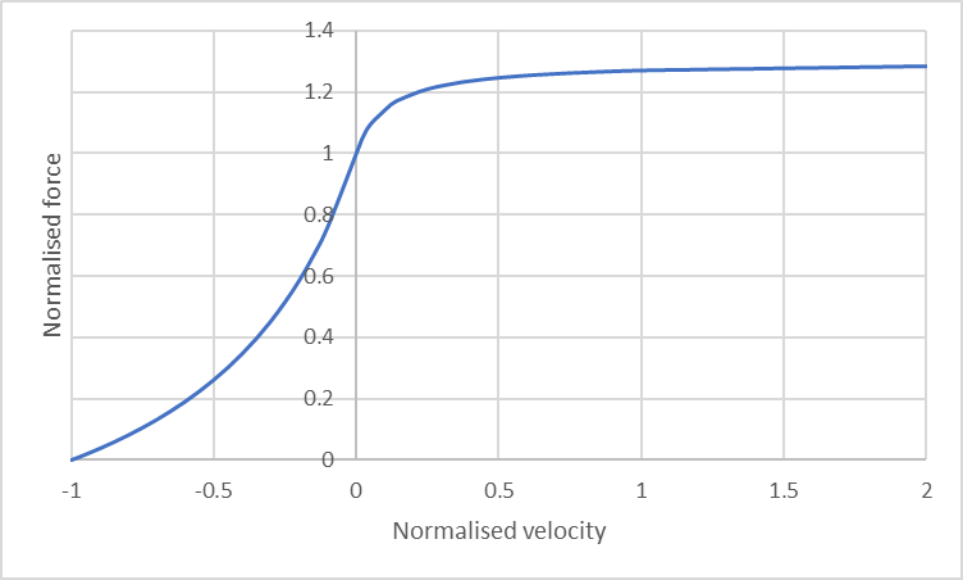

Figure 2-13: Contraction force in relation to the velocity of the contraction.

The muscle can produce passive restorative force and active force. The first one is developed without activation by the material against stretching, and the other one is generated with activation, not directly related to the length, caused by the sliding filaments of the sarcomere. Another characteristic is that as the velocity of shortening increases, the resistance force decreases, because of the relation with the number of links between actin and myosin (Lee et al., 2011), which takes some time to connect. For example, when a muscle shortens with lower velocity, the higher number of connections produce more force.

2.2.3 Hill-Type Active Muscle Model

The Hill-type active muscle model is a widely used approach to model muscle activation and the resulting force. The model is based on the micro-structures responsible for the movement of the myocytes (cells), the sarcomeres. The Hill muscle model has been widely implemented in many commercial finite element codes, often for two-dimensional elements joining two points in a model, representing a muscle.

Three components form the Hill-type muscle representation (Figure 2-14): the series element (SE), the parallel element (PE), and the contractile element (CE). The SE represents the elastic behaviour of the sarcomeres and tendons, the PE represents the passive elasticity produced by connective tissue penetrating the muscle, and the CE represents the active contraction force (Lee et al., 2011).

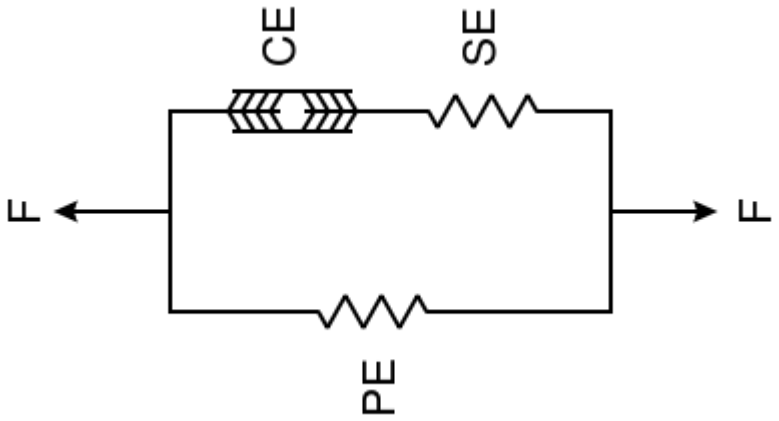

Figure 2-14: Hill-type element (Imaged adapted from: (Hellmuth, 2010)).

The resultant force produced by this model is the sum of the SE, and the serial effect of the PE or CE and the serial effect of PE (Equation 3). The resultant change in length is equal to the stretch in PE or the sum of the change in length in SE and CE (Equation 4).

$$\mathbf{F_f = F_{PE} + F_{SE} = F_{PE} + F_{CE}} \quad \textbf{(3)}$$

$$l_f = l_{PE} = l_{SE} + l_{CE} \quad \textbf{(4)}$$

From the structure of the sarcomeres, it is possible to assume that the force generated by the contractile element has a maximum value, F_{max}. This value is reached when the neuronal activation, $a(t)$, is 100%. Further, the force produced by the myocyte depends on the functions of the rate of contraction, $g(\dot{\lambda_f})$, and the stretch (or length) of the fibre, $f(\lambda_f)$, (Equation (**5**). The force of the PE is

based on a function of the stretch of the fibre, $h(\lambda_f)$, (Equation (**6**) and the force of the SE is a function of the length of the fibre and a non-dimensional quantity proportional to the strain of the contractile element, $k(\lambda_f, \delta_{CE})$ (Equation **(7**). The $g(\dot{\lambda_f})$, $f(\lambda_f)$, $h(\lambda_f)$ and $k(\lambda_f, \delta_{CE})$ are functions or curves defined by experimental data.

$$F_{CE} = F_{max}.a(t).f(\lambda_f).g(\dot{\lambda_f}) \quad \textbf{(5)}$$

$$F_{PE} = F_{max}.h(\lambda_f) \quad \textbf{(6)}$$

$$F_{SE} = F_{max}.k(\lambda_f, \delta_{CE}) \quad \textbf{(7)}$$

2.2.4 EMG Measurement of Active Muscle Response

The neuronal impulses that activate the muscles cannot be measured directly; however, the electromyography (EMG) techniques are used to obtain information about the muscle response during specific movements providing indirect insight in the activation parameters. The EMG method measures the intensity of electric signals in the muscles through time. Surface electrodes placed on the skin or fine-wires inserted in the muscles can be used to measure the activation time when volunteers are subjected to external loads (Wittek et al., 2001). The measured signals are usually normalized to the maximum voluntary contraction (MVC) (Fice et al., 2018; Morimoto et al., 2013; Siegmund et al., 2007). The signals obtained from the electrodes need to be modified to account for the thermal noise from the electronics and electrochemical noise at the interface of the electrodes (De Luca et al., 2010). In addition, the surface-mounted sensor methodology presents a limitation due to the necessity to remove artifacts related to low-frequency movements of muscle and other tissues relative to the skin (De Luca et al., 2010; Wittek et al., 2001). The fine-wire technique, on the other hand, produces signals that are not altered by high-pass filters with cut off frequencies, but it is rarely used in biomechanics due to the inconvenient application (Wittek et al., 2001). A study comparing both types of electrodes

indicated that the use of high-pass filtering can prevent motion artifacts from the EMG collected under impact conditions and that the reflex times obtained were similar for the two types of electrodes (Wittek et al., 2001).

A study investigating EMG effects in superficial neck muscles contracting voluntarily in different directions showed that the forces, and therefore $a(t)$ (Equation 5), presented a small correlation to the signal obtained (Amell, 2002). As indicated by the author, the EMG can be used to indicate which muscle group is more active but cannot be used to precisely measure the activation level magnitude. Considering the limitations of the methodology, the onset times during impact tests with volunteers, of the cervical muscle groups, could be more accurately defined through EMG experiments. A review of several frontal and rear impact tests showed that the ranges of onset times are between 55 ms and 99 ms with an average of 74 ms (Blouin et al., 2003; Foust et al., 1973; Hernández et al., 2006; Magnusson et al., 1998; Ono et al., 1997; Siegmund et al., 2002; Snyder et al., 1975).

Other experimental studies in volunteers normalized the EMG data to the maximum voluntary contraction (MVC) and could be used to compare the activation scaling in HBMs. Two studies used to validate the muscle activation of the KTH neck model followed these criteria (Hedenstierna et al., 2009). One was a low severity test conducted with three volunteers with deep muscle EMG that presented a sternocleidomastoid activation of 40% and a trapezius activation of 10% (Siegmund et al., 2007). The other one was a low severity sled test conducted with ten volunteers with a superficial EMG that presented a sternocleidomastoid activation of 39% and a trapezius activation of 79% (Kumar et al., 2003). It is worth noting that the EMG data is useful to inform onset times and muscle activation magnitudes, but the measurement of MVC always has some variability associated. The equipment noise, as well as the possibility of the MVC not representing the true maximum muscle activation possible, indicates the necessity of observing comparisons with this data with skepticism and the need for more experiments to obtain more comprehensive knowledge of muscle activation schemes.

2.2.5 Human Startle Response

The startle reflex is initiated by sudden acoustic, tactile or vestibular stimuli, according to animal studies, and it generates a whole-body response, activating hundreds of muscle groups in a stereotyped way (Yeomans et al., 2002) (Figure 2-15). Another characteristic of this response is the fast habituation after a small number of stimuli; the activation of the muscle groups is reduced, and just the eye blink reflex is recorded to remain (Siegmund et al., 2001b). Also, the startle reflex is facilitated and habituation is diminished if the subject is alerted before executing the movement (Siegmund et al., 2001b).

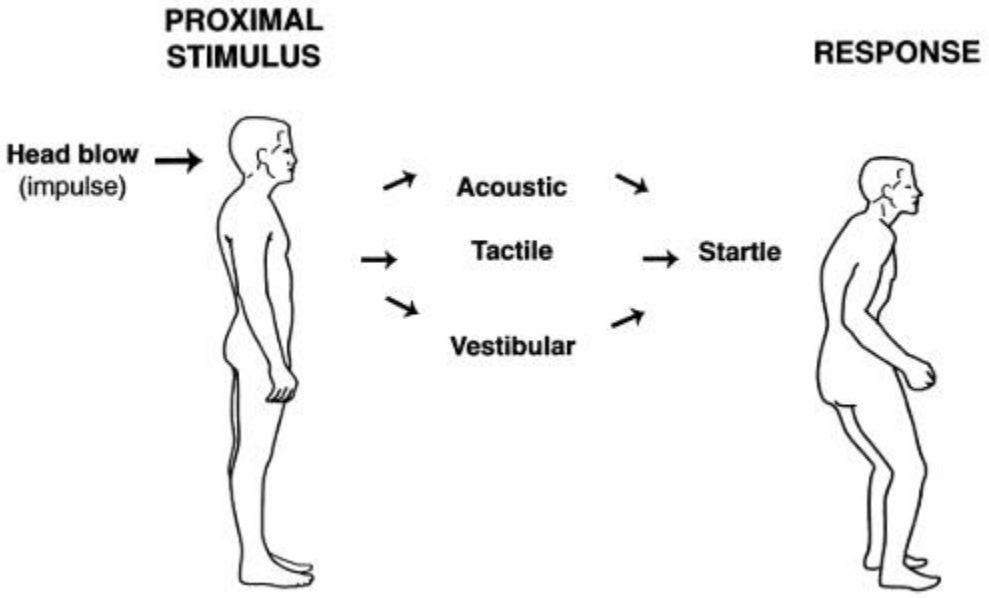

Figure 2-15: Startle response stereotyped movement (Image from: (Yeomans et al., 2002)).

An experiment conducted with sequential sled rear impacts with volunteers (Blouin et al., 2003) showed that during the first unexpected trials, all the subjects presented stereotypical kinematics and EMG responses. During the subsequent trials, half of the volunteers presented an increase in head extension, indicating habituation similar to the one predicted in the startle response. Also, different

responses were observed between aware and unaware subjects in other sled impact studies (Fanta et al., 2013; Siegmund et al., 2003), which could be related to the pre-alert effect seen in a startle reflex.

A series of studies were conducted with acoustic stimuli being used before sled impacts and voluntary movements (Mang et al., 2015; Siegmund et al., 2008, 2001b). Changes in muscle activation were observed due to the applied sound, pointing to muscle activation characteristics similar to the startle response.

2.3 Experimental Impact Studies involving Human Volunteers

A series of methods can be used to analyze the biomechanical response of the human body: human volunteers, PMHS, animals, ATD and mathematical models (Schmitt et al., 2014). ATDs and PMHS are usually used for sled impact studies but lack muscle activation. Therefore, human volunteers are necessary to observe muscle contributions during impacts (Siegmund et al., 2001a). Many impact studies using cars or sleds have been conducted with volunteers (Carlsson et al., 2010; Ólafsdóttir et al., 2013; Pramudita et al., 2007; van den Kroonenberg et al., 2010); however, to apply their conditions to a computational HBM well-defined boundary conditions are necessary. This can be challenging to obtain precise material properties of the seat or the restraint system from the available literature. For frontal, lateral and rear impact studies, the NBDL (Wismans et al., 1986) and Sato (Sato et al., 2014) sled tests with volunteers presented detailed information for the boundary conditions as well as the resultant head kinematics.

2.3.1 Frontal Human Volunteer Sled Test Data

Frontal impact studies were undertaken by the NBDL with human volunteers using a sled, with maximum accelerations ranging from 2g to 15g and having head kinematics as the main output. For the NBDL study, the head and T1 motions were recorded in three-dimensions using accelerometers and

high-speed photography for 119 frontal impact sled tests with 16 volunteers (Wismans et al., 1986). The short duration acceleration pulses (Figure 2-16 and Figure 2-17) were applied while the subjects had their movement restricted by shoulder straps, an inverted V-pelvic strap, a lap belt, upper arm and wrists restraints (Wismans et al., 1986).

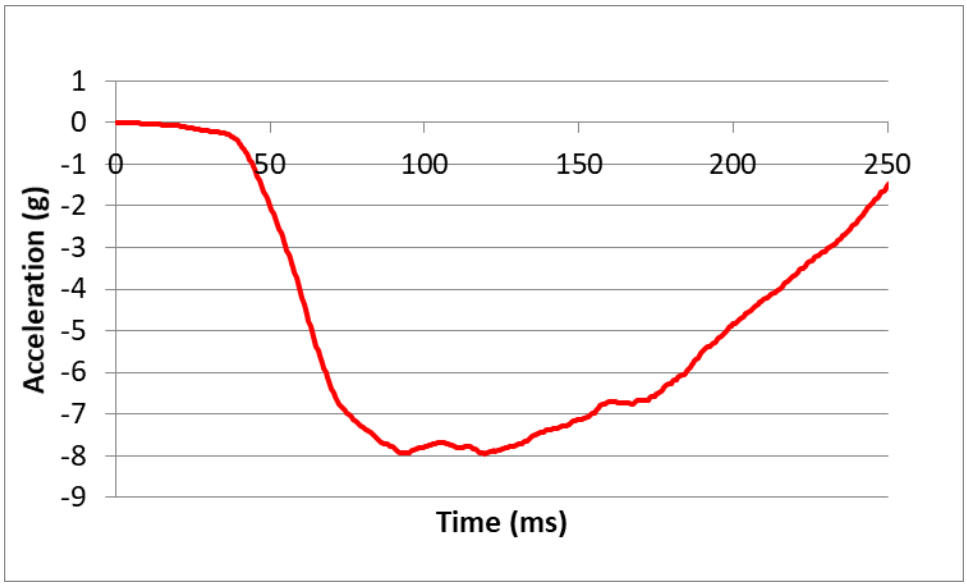

Figure 2-16: Average of the sled acceleration for the 8g frontal impact

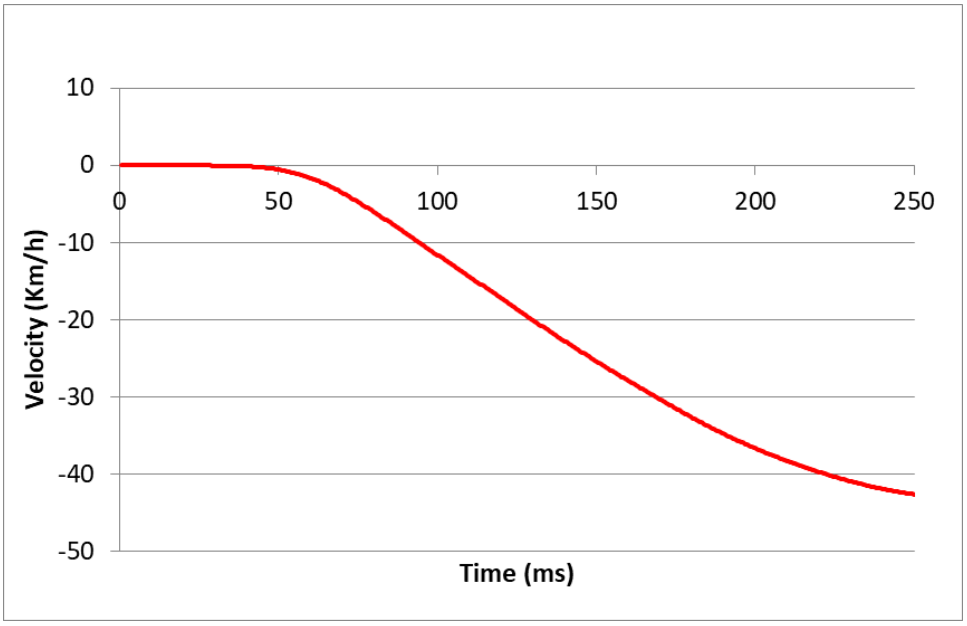

Figure 2-17: Average of the sled velocity for the 8g frontal impact.

Three transducers, mounted in moulds made specifically for each subject, were applied in three locations to measure the accelerations during the experiments. The sensors were positioned in repeatable positions on the skin of the volunteers. One was directly above T1, another was in a mouthpiece, and the last one on the top of the head. The acceleration pulses were developed by a piston propulsion system (Ewing and Thomas, 1972). The obtained T1 acceleration data were subsequently corrected using information from the recorded highspeed film data for slipping of the sensor in some of the 14g and 15g cases (Thunnissen et al., 1995). The test data was made available by the NHTSA in an online electronic database ("National Highway Traffic Safety Administration," 2012). The pointwise average of the T1 kinematics (Figure 2-18 and Figure 2-19) for each impact severity can be used as the boundary condition for the isolated head and neck system computational simulations as done previously in the literature (Fice et al., 2011; Panzer et al., 2011). The absence of headrest and previously mentioned constraints minimize the variables of the problem, making the average T1 kinematics obtained from these studies useful as boundary conditions for head-and-neck finite element models.

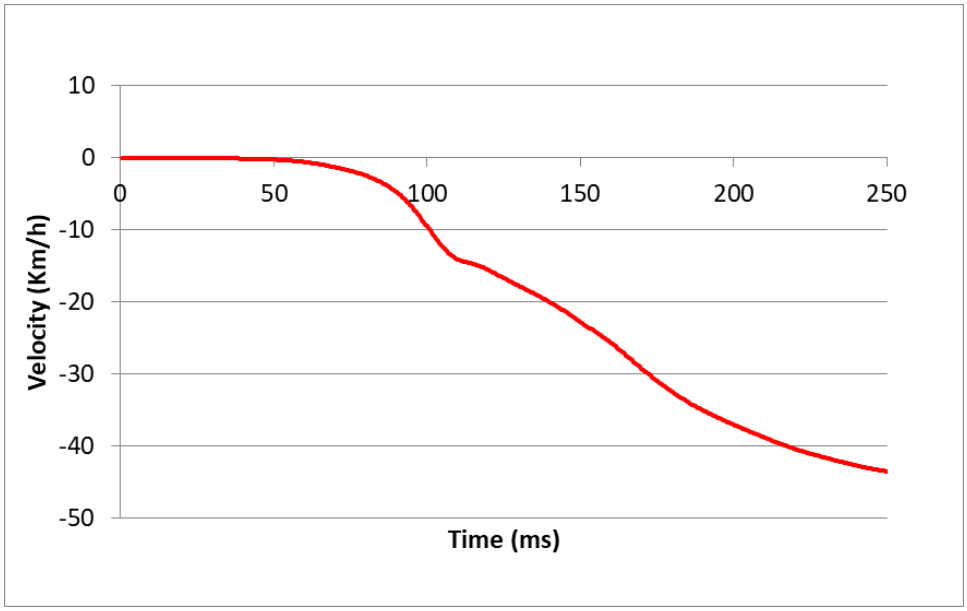

Figure 2-18: Average velocity in the X direction of the T1 in the 8g frontal impact experiments.

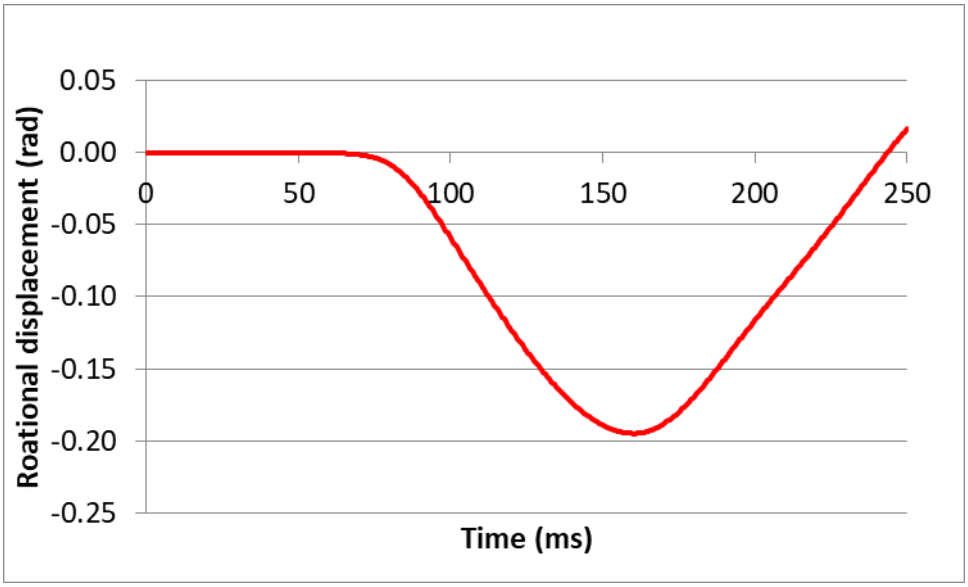

Figure 2-19: Average rotation of T1 in the Y direction for the 8g frontal impact experiments.

2.3.2 Lateral Human Volunteer Sled Test Data

Lateral impact studies were undertaken by the NBDL with human volunteers using an acceleration sled, with maximum sled accelerations ranging from 4g to 7g, and having head kinematics as the main output.

For the NBDL study, the head and T1 motions were recorded in three dimensions using accelerometers, similar to the frontal case, and high-speed photography for 72 lateral impact sled tests with 16 volunteers (Wismans et al., 1986). As the lateral and frontal tests were based on the same methodology, the short duration acceleration pulses (Figure 2-20 and Figure 2-21) were also applied while the subjects had their movement restricted by shoulder straps, an inverted V-pelvic strap, a lap belt, upper arm and wrists restraints (Wismans et al., 1986).

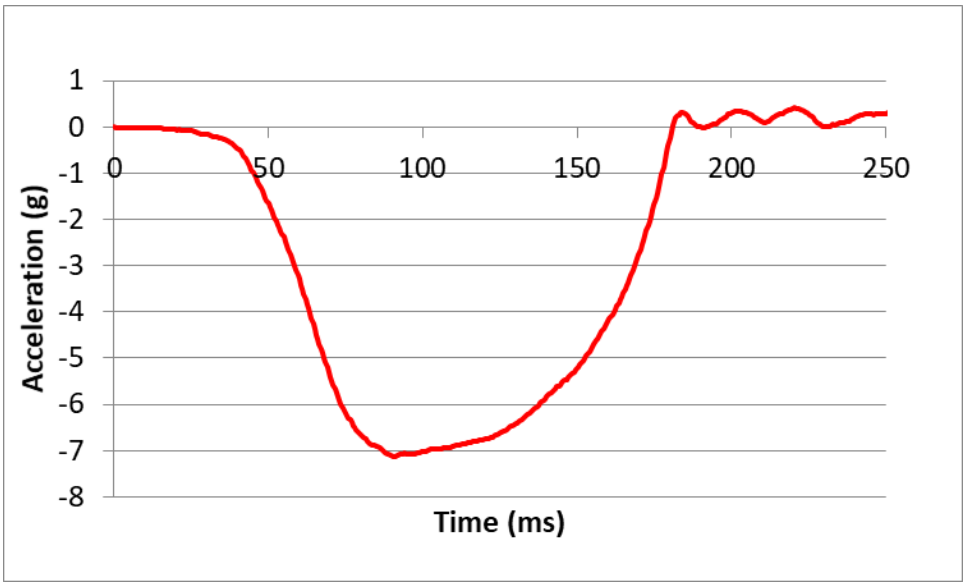

Figure 2-20: Average of the sled acceleration for the 7g lateral impact.

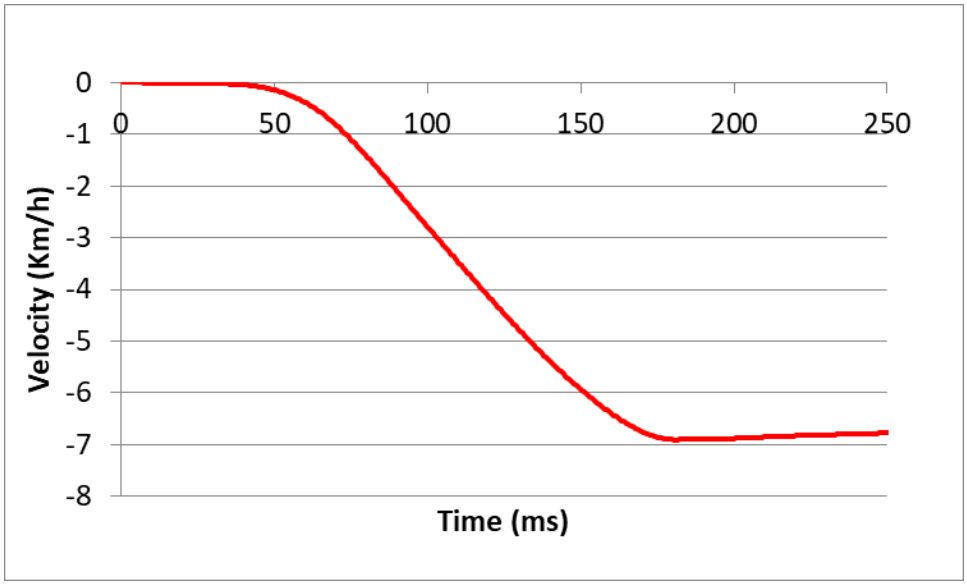

Figure 2-21: Average of the sled velocity for the 7g lateral impact.

The acceleration ranges made available by the NHTSA database were smaller than the frontal cases, but the absence of headrest and body constraints make the average T1 kinematics (Figure 2-22 and Figure 2-23) obtained from these studies useful as boundary conditions for head-and-neck finite elements models.

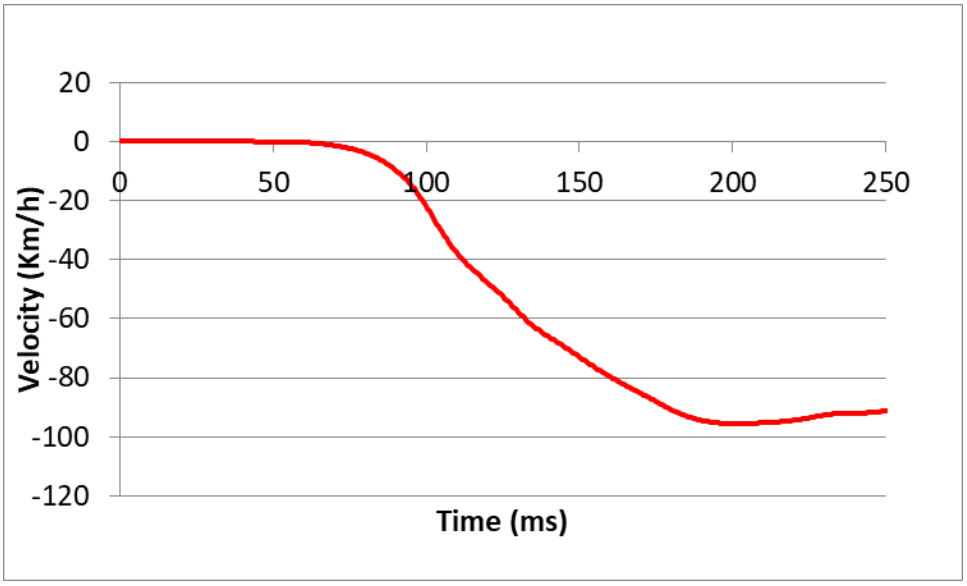

Figure 2-22: Average velocity in the Y direction of the T1 in the 7g lateral impact experiments.

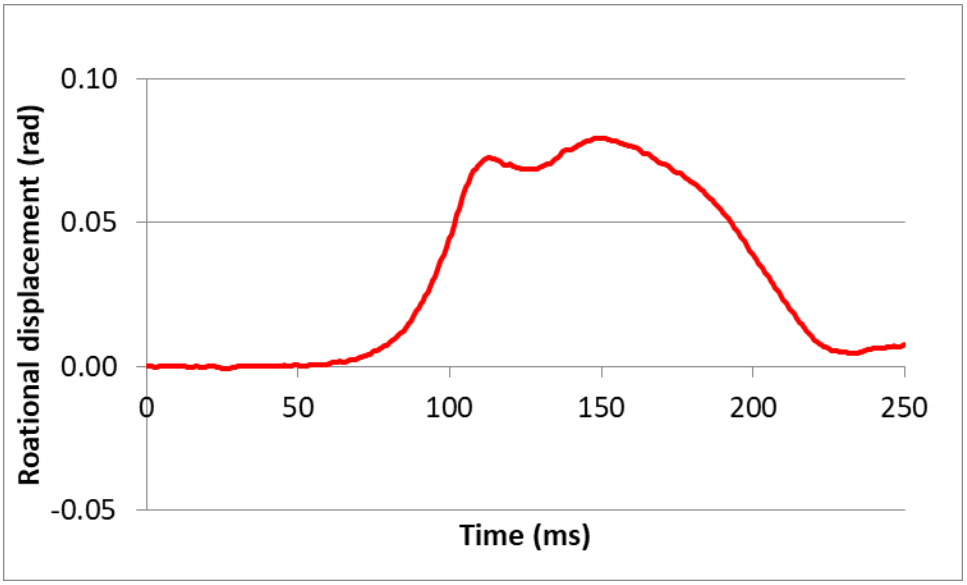

Figure 2-23: Average rotation of T1 in the X direction for the 7g lateral impact experiments.

2.3.3 Low Severity Human Volunteer Rear Impact Scenarios

Rear impact studies were undertaken by the Ono and Sato with human volunteers using an acceleration sled, with maximum sled accelerations ranging from 3g to 4g and having head kinematics as the main output.

For the Sato study, the head and T1 motions were recorded using accelerometers and high-speed photography for 12 male volunteers (Sato et al., 2014). The sled was set in inclined rails and released from the top with a hydraulic damper in the lower portion generating the different decelerations (Ono et al., 1997) (Figure 2-24 and Figure 2-25).

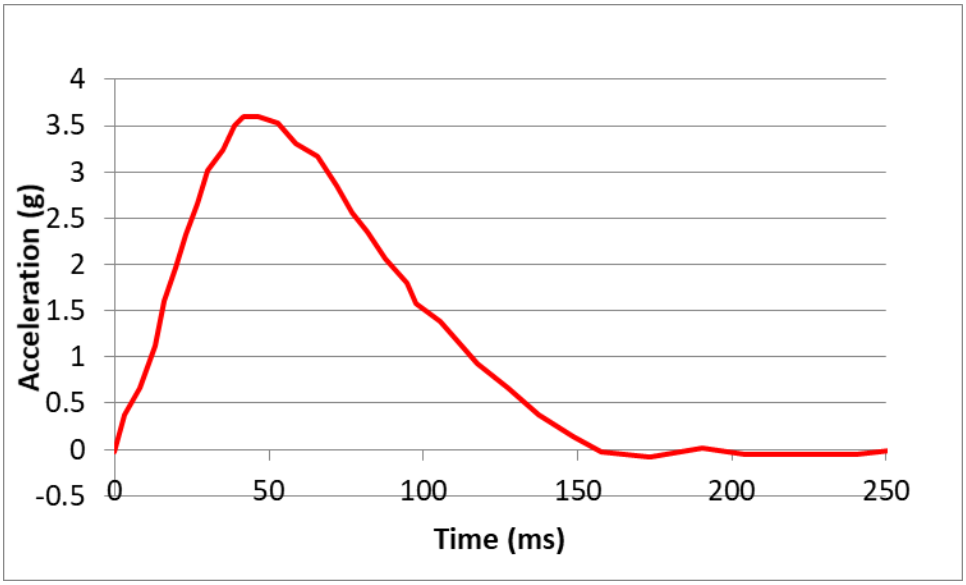

Figure 2-24: Average of the sled acceleration for the 4g rear impact.

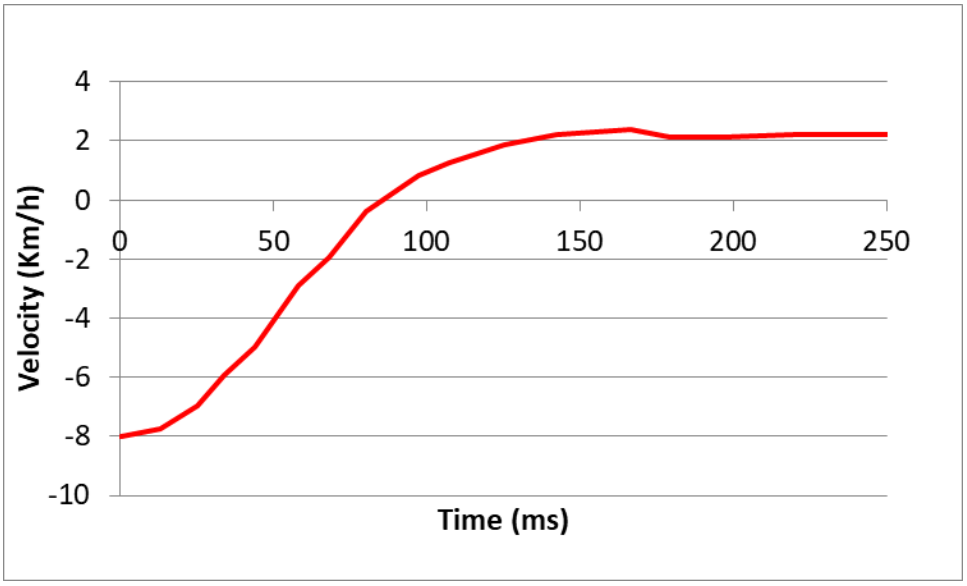

Figure 2-25: Average of the sled velocity for the 4g rear impact.

Two biaxial accelerometers were mounted on a head rig fastened to the forehead and mouth, and a third biaxial accelerometer was positioned on the skin surface of the T1 process. Also, markers were placed at the auditory canal, the skin surface of the T1 process, upper sternum, and iliac crest for the video recording. The subjects were asked to relax, and no constraint system was placed as the backseat would hold the movement in the rear-impact, but no headrest was used. Again, the acceleration ranges made available were smaller than the frontal cases, but the absence of headrest and similar methodology make the average T1 kinematics (Figure 2-26, Figure 2-27 and Figure 2-28) obtained from these studies useful as boundary conditions for head-and-neck finite elements models. The characteristic S-shape curvature of the neck during rear impacts, when the neck extends while the upper cervical spine flexes, was also observed during this experiment (Ono et al., 1997).

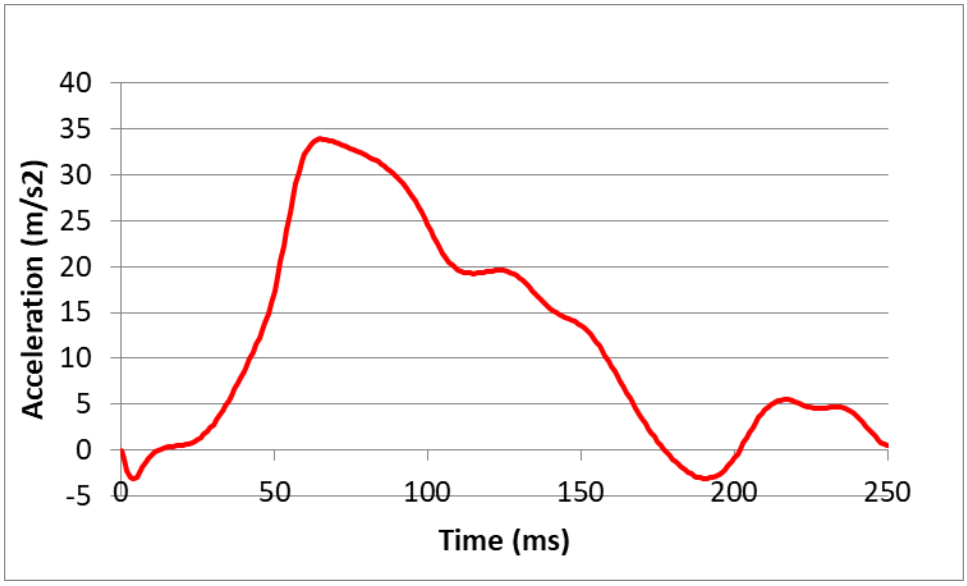

Figure 2-26: Average acceleration in the X direction of the T1 in the 4g rear impact experiments.

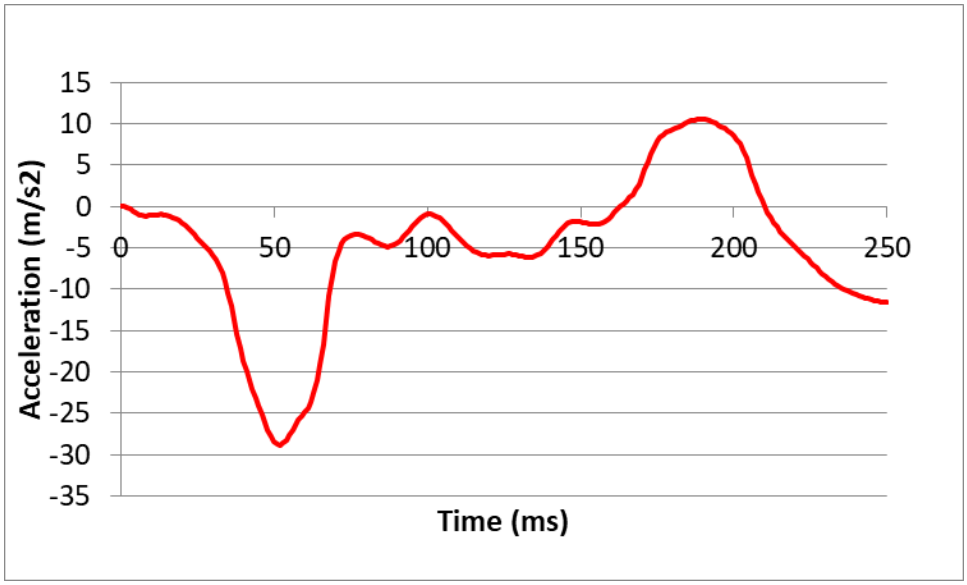

Figure 2-27: Average acceleration in the Z direction of the T1 in the 4g rear impact experiments.

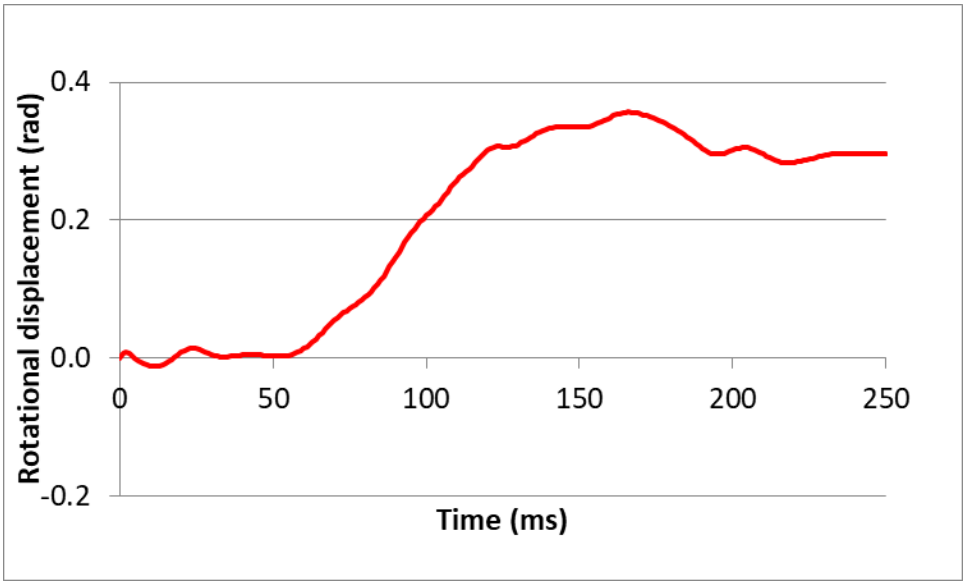

Figure 2-28: Average rotation of T1 in the Y direction for the 4g rear impact experiments.

2.4 Computational Human Body Models

For over four decades, computational HBMs of the neck have been developed to evaluate its tissue-level response (Yang et al., 2018). Generally, neck models consist of the cervical vertebrae, IVDs, ligaments and musculature (Yang et al., 2018). A group of well-recognized contemporary head-and-neck models are the models by Yang et al. (1998), Deng et al. (1999), Human Model for Safety (HUMOS), Meyer et al. (2004), Total Human Model for Safety (THUMS), University of Waterloo (UW) model, Osth et al. (2016) and the GHBMC (Yang et al., 2018). The first model was based on anatomical data from Magnetic Resonance Imaging (MRI) scans of a 50th percentile male volunteer and including T1 to C1 to T1 vertebrae, IVDs, ligaments, and muscles. The model from Deng et al. was based in detailed 3D anatomical data and presented only the ligamentous cervical spine, with no musculature. The HUMOS intended to design a more accurate model in a sitting position for injury evaluation during automotive impacts. Meyer et al. used a specific volunteer close to a mid-size male to develop a neck model. The THUMS was originally a 50th percentile male in a seated or standing

position to investigate the response of automotive occupants and has subsequently received many updates. The UW model presented vertebrae from T1 to C1, the skull and structural tissues. Osth et al. used Computed Tomography (CT) scan data to build a female ligamentous cervical spine model. The initial GHBMC model, designed to investigate automotive safety, was a 50th percentile male full body model with various anatomical regions being developed separately by different research groups across the globe.

A literature review of 22 musculoskeletal models of the cervical spine (Alizadeh et al., 2020) showed that 16 were able to simulate dynamic conditions of head and vertebral bodies kinematics. All models presented straight muscle lines and 10 incorporated frictionless via-points to consider muscle curvature around the spine like the GHBMC model. Pre-defined activation curves were used in 14 models with direct EMG curves being used in only three. The intervertebral disc stiffness, ligament forces, and facet contact were developed in independent structures, similar to the GHBMC model, only in 8 models. Also, the muscles of 18 models were implemented with Hill-type elements, and only three of the models incorporated passive muscle properties. In the GHBMC model, the active properties of the muscles were represented by one-dimensional Hill-type muscle elements and the passive properties were represented by the three-dimensional muscle elements (Figure 2-29).

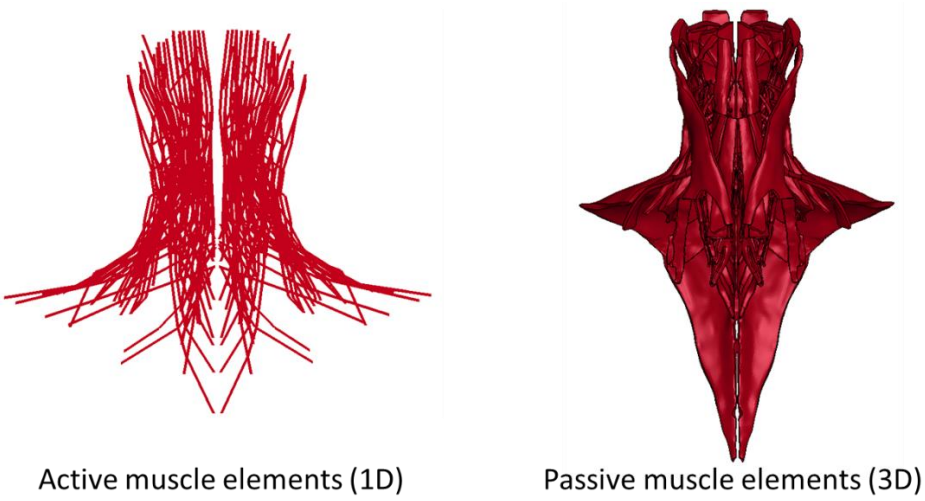

Figure 2-29: 1D Hill-type active muscle elements and 3D passive muscle tissue elements in the GHBMC neck model.

The GHBMC 50th percentile male full-detailed head-and-neck model can be extracted from the full human body model (Figure 2-30). The neck region included the muscles, vertebrae, ligaments, intervertebral discs and other soft tissues relevant to impact loading (Figure 2-30). The model was developed from MRI and CT scans of a living 26 years old adult with the anthropometrics of a mid-size male (Yang et al., 2018) and validated with experimental data at the cervical spine level (Barker et al., 2017, 2014; Lasswell et al., 2017; Mattucci et al., 2012). It obtained a good validation performance to the head and neck (Fice et al., 2011; Panzer et al., 2011). A simplified head (Figure 2-30) without the brain is available in contrast to the full detailed head to reduce the computational cost when stresses in the encephalic tissue are not relevant for the analysis. The simplified head includes the same mass and inertia as the full detailed head (Figure 2-30) and produced the same kinematics of the full-body model.

Figure 2-30: A) GHBMC 50th percentile male full human body model B) GHBMC 50th percentile male full detailed head C) GHBMC 50th percentile male simplified head

The passive properties of the muscles were implemented in 3D elements using a hyperplastic Ogden material model with viscoelastic effects fitted to experimental data. The passive elements were connected to Hill-type beam elements modelled with the active properties of the muscles, because of that, the SE and PE were not used (Correia et al., 2020). Also, to replicate the contraction pathway of the muscles, the passive elements were connected to the bones through 1D attachments.

Comparatively, the other models in the literature that incorporated musculature like the KTH, JAMA, THUMS, and simTK models (Brolin et al., 2005; Ejima et al., 2005; Iwamoto et al., 2012; Vasavada et al., 1998) did not incorporate a combination of skin, adipose tissue, 3D passive muscles and active 1D muscles like the GHBMC model, except for the THUMS model, which could change the stiffness of the head and neck system affecting the kinematics. Also, the active musculature models have been checked only with a relatively small number of lower severity events when validating against volunteer studies.

The formulation for the force generated by the 1D active muscle elements uses maximum stress instead of maximum force (Equation 8). Further, it can be observed that the contraction force is dependent on the physiological cross-sectional area of the muscle (PCSA).

$$F = \sigma_{max}.PCSA.a(t).f(\lambda_f).g(\dot{\lambda_f}) \quad \textbf{(8)}$$

The level of activation of these elements is specific for each situation and is related to the neuronal input of the muscles (Figure: 2-31).

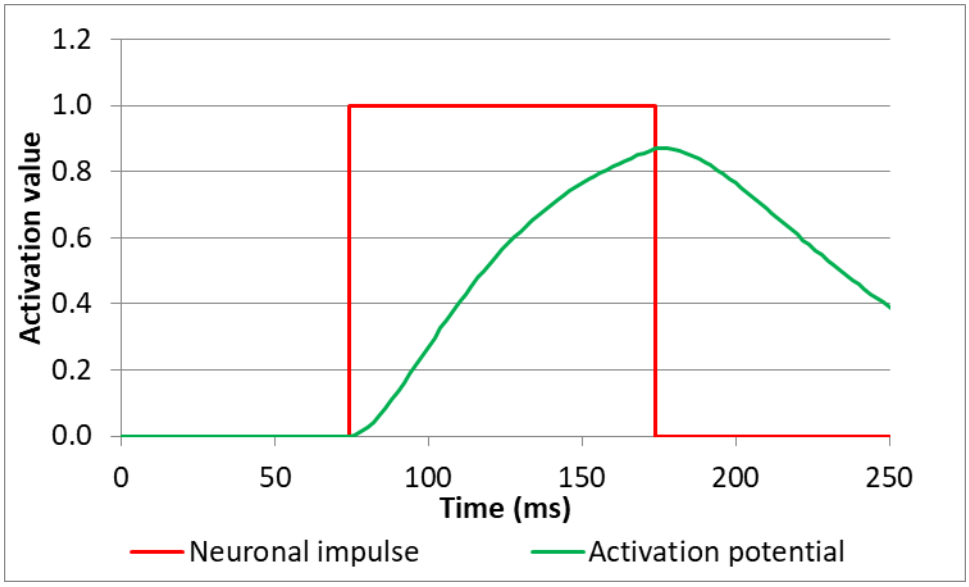

Figure: 2-31 Neuronal impulse and equivalent activation level curve for a 100 ms neuronal impulse starting at 74 ms.

This neuronal input, $\mathrm{u(t)}$, was converted in the activation curve, $a(t)$, through two time-dependent functions (Equations (**9** and (**10**) that allow modelling activation and deactivation in a single process.

$$\frac{\mathrm{d(a(t))}}{\mathrm{dt}} = \frac{\mathrm{u(t)\text{-}e(t)}}{\mathrm{t_{ne}}} \quad \textbf{(9)}$$

$$\frac{\mathrm{d(e(t))}}{\mathrm{dt}} = \frac{\mathrm{e(t)\text{-}a(t)}}{\mathrm{t_a}} \quad \textbf{(10)}$$

The idealized neural input is necessarily between 0 and 1. $\mathrm{t_{ne}}$ and $\mathrm{t_a}$ are time constants. When $\mathrm{e(t)}$ is higher than $a(t)$, the muscle is activating; in the opposite case, it is de-activating.

The cortical bone of the vertebrae was modelled using shells with a piecewise plasticity model, and the trabecular bone was generated using solid elements also with a piecewise plasticity model. The ligaments were modelled using 1D beam elements with properties obtained in tensile experiments. The intervertebral discs were designed using anisotropic fabric elements to emulate the tissue fibres and Hill foam to represent the matrix similar to a composite. The synovial fluid was modelled as an elastic fluid material. The skin was modelled using shell elements with linear viscoelastic properties, and the flesh, as well as soft tissues beneath it, were modelled using solid elements with a simplified rubber material. The trachea and surrounding soft tissues were modelled as shell elements with a simplified rubber material based on tensile experiments of the throat.

The computational head-and-neck model was validated with PMHS and volunteer experiments which included spine-level studies and sled tests. Quasi-static and high rate tests of tension, flexion and extension of the segments from C2 to T1, and the axial rotation from C0 to T1 were used to validate the segment levels while the full neck was checked against full neck tensile experiments (Elemance, 2016). At the global level, the NBDL frontal and lateral impact test with volunteers (Ewing and

Thomas, 1972), and cadaver sled tests in rear impacts (Deng et al., 2000) were used to validate the global head-and-neck model (Elemance, 2016).

2.5 Comparative Data Analysis through Correlation Ratings

A commonly employed method to compare two data sets objectively is the correlation rating analysis implemented in the Correlation and Analysis (CORA) software developed by Partnership for Dummy Technology and Biomechanics. This methodology was successfully used to quantify differences between simulated and experimental data in movements of the full neck or segments of the cervical spine (Barker et al., 2014; Feller et al., 2016).

The correlation rating methodology considers a user-defined weighted sum of a corridor rating (C) and a cross-correlation rating. The corridor rating is defined as an average of values given to each point in the simulated response curves. The values are between 0 and 1 based on the standard deviation of the experimental data. If it is inside one standard deviation, it is rated 1; if it is outside two standard deviations, it is valued as 0; and if it is between these corridors, it is a result of interpolation.

The cross-correlation rating, on the other hand, was calculated as a weighted average of the response phase (P), shape (V) and size (G) (Figure 2-32). Commonly used weights are $G_p = 0.25$, $G_v = 0.50$ and $G_g = 0.25$ (Panzer et al., 2011; Vavalle et al., 2013). The responses are given the value of 1 if they perfectly match the experimental curve, 0 if there is no overlap with the experimental curve and a value between 0 and 1 for the other cases.

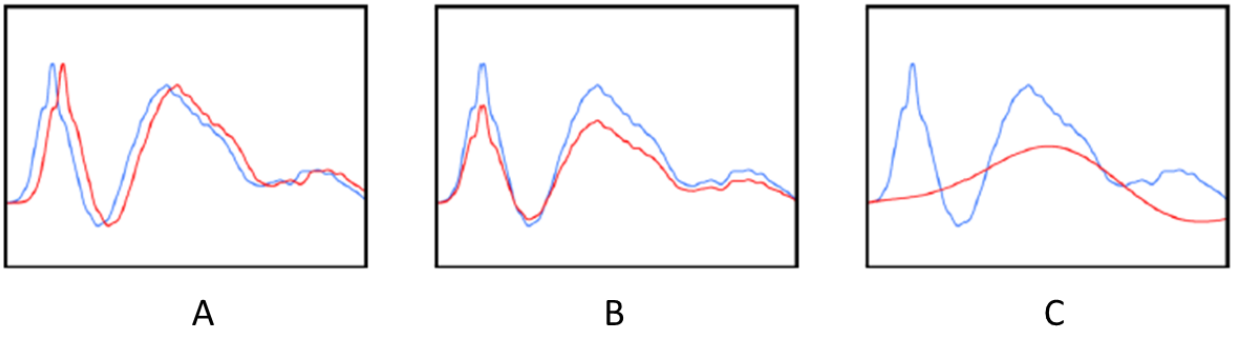

Figure 2-32: Differences of phase (A) size (B) and shape (C) responses (Image adapted from: (Thunert, 2017)).

The ISO/TR9790 defines a scale that can be used to classify the correlation ratings obtained by this methodology between excellent and unacceptable (Table 2-2) (Thunert, 2017).

Table 2-2: Classification of the correlation rating.

Overall biofidelity rating	Correlation rating
Excellent	0.86-1.00
Good	0.65-0.86
Fair	0.44-0.65
Marginal	0.26-0.44
Unacceptable	0.00-0.26

2.6 Muscle Activation Optimization

One of the most common approaches to obtain muscle activation properties in HBM are through optimization methods. In a recent literature review (Alizadeh et al., 2020), muscle force and, indirectly, activation levels were predicted by inverse dynamics optimization in four different neck models. However, optimization techniques have also been used to directly obtain the activation of the muscles in static or dynamic activities in other HBMs (Östh et al., 2015).

The change in the constraints (possible values of the variables and outputs) of the optimization may drastically alter the outcome of the process. The definition of these values is challenging, and many researchers base their methodologies on objective functions like maximum force or total work produced by the muscle (Mortensen et al., 2018). However, the muscle response, when efficiency is not the main objective, has not been adequately explored (Mortensen et al., 2018).

For the neck muscles specifically, a study optimized 22 cervical muscles activation properties and evaluated the response in gravitational and frontal impact loading conditions with results comparable to the experimental data (Dibb et al., 2013). Another study used a similar methodology derived from the previous study, a linear response surface optimization, to observe spatial tuning patterns on the head response in dynamic conditions (Ivancic and Pradhan, 2017). Although the methodology used in these studies improved the head response to the observed cases, no study was found to cover a broader look at the effects of muscle activation in different impact scenarios and severities. Therefore, a muscle activation optimization study encompassing many different scenarios bounded by the available experimental data was still necessary to help direct future research related to neck injury and automotive safety mechanisms.

Chapter 3: Methods

3.1 Methodology Overview

The head-and-neck model was extracted from an average stature male HBM M50-O v4.5, 50th percentile, GHBMC. The neck model included detailed representations of the neck musculature, represented by passive 3D and active 1D Hill-type elements. The T1 kinematics over a wide range of accelerations for frontal, lateral and rear volunteer impacts were applied to the T1 vertebra of the model and used in simulations with different muscle magnitude and onset times of muscle activation in a commercial FE software (LS-DYNA, LSTC, R.7.1.2, Livermore, CA). The head center of gravity kinematics from the simulations was compared to the experimental data through a correlation rating. After selecting the best intervals for each muscle activation parameter, optimization was carried for each impact case and the head kinematics were analyzed to verify possible trends and the hypothesis that one single activation scheme could produce reasonable kinematics for all the different acceleration directions (Figure 3-1).

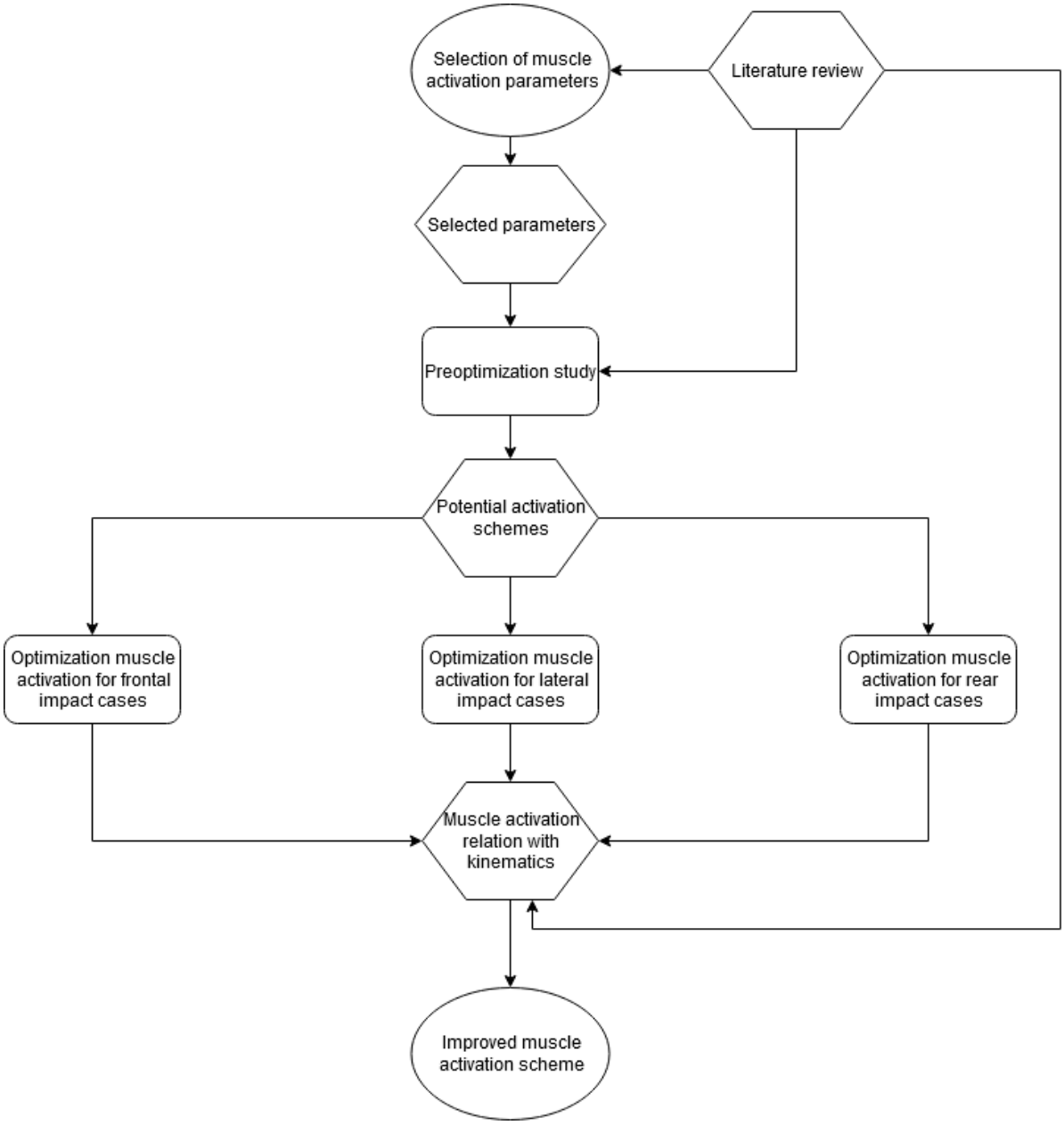

Figure 3-1: Steps of the muscle activation optimization.

For the volunteer experimental data, the frontal and lateral NBDL sled tests with volunteers previously mentioned were used to define the boundary conditions and the output head kinematics of the simulations. The frontal and lateral sled experiments were selected among other impact tests due to the volunteers being restrained firmly to the sled using a pre-tightened harness system. This was not

necessary for the rear impact due to the seat back restraining the body. For the rear impact investigations, a study conducted with 12 male volunteers sled tests (Sato et al., 2014) was used to define the boundary conditions and the output head kinematics of the simulations. For all three impact cases (frontal, lateral and rear), each subject volunteer was subjected to a controlled acceleration pulse of a specific magnitude and no headrest was used allowing for well-defined boundary conditions necessary to HBM.

The head and T1 kinematics extracted from each experimental impact severity and direction were used to construct pointwise average curves and one standard deviation corridors (Figure 3-2). The T1 kinematics were used as the boundary conditions in the simulated model and the head kinematics were used to verify the model response using correlation rating or MSE.

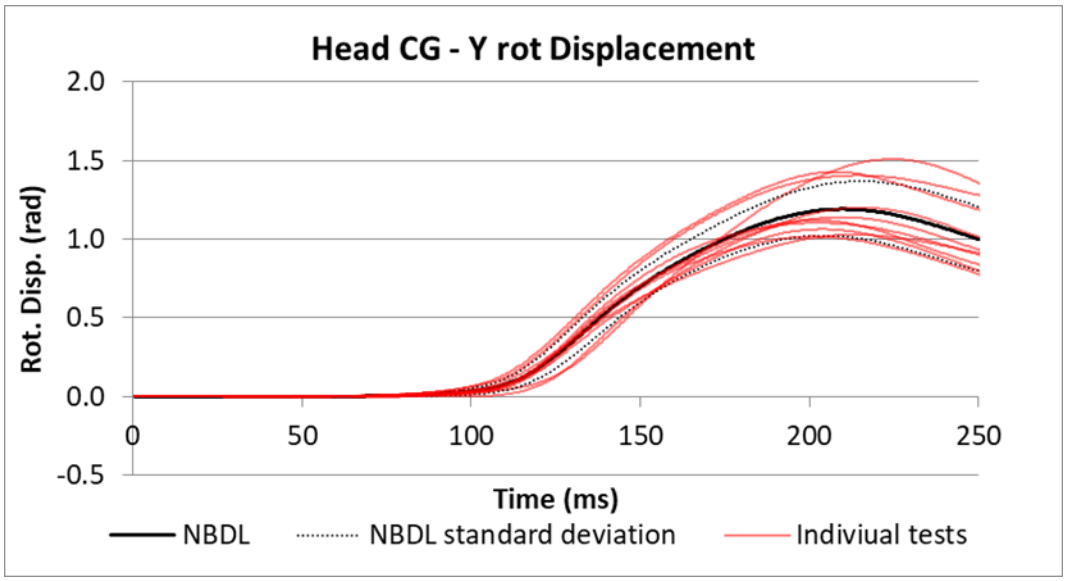

Figure 3-2: Example of experimental average and standard deviation (corridors) for head rotation in 8g frontal impact.

As the PCSA and material properties were already defined in the model based on previous studies (Panzer et al., 2011), the current analysis focused on the remaining muscle activation variable,

the activation curve. Considering constant neural input duration, two parameters needed to be determined: activation level and activation onset time. The overall shape of the activation level versus time curve (Figure: 2-31), during the impacts, was based on a neural input with 100 ms duration. This represented the time between experimental muscle activation onset time and time when the T1 acceleration was reduced in relation to the peak acceleration (Panzer et al., 2011).

3.2 Assessment of the Muscle Activation

Complex motions of the head and neck vary based on the contributions of each individual muscle; different movements will result from varied intensity and timing for each muscle. Yet, this effect is poorly understood in terms of muscle activation magnitudes, specifically in high severity impacts and in deeper muscles. As such, a simplification of the neck muscles was required for implementation within the GHBMC neck finite element model. The muscles were grouped in four quadrants based on their position and functionality: right extensor, left extensors, right flexors, and left flexors (Figure 3-3). The strongest extensor (trapezius) and flexor (sternocleidomastoid) were selected as representative of the activation of each group for comparison with the literature, based on the assumption that they would generate more force and dominate the kinematic response of the head.

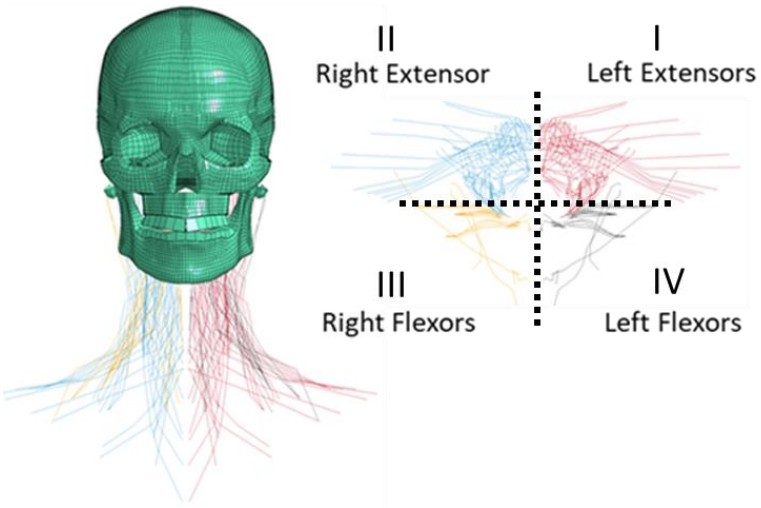

Figure 3-3: GHBMC M-50 muscles grouped in quadrants.

Table 3-1: Flexor and extensor muscle groups

Muscle groups	
Extensors	Flexors
Oblique capitis inferior	Longus capitis
Oblique capitis superior	Longus colli
Rectus captis major	Rectus capitis anterior
Rectus captis minor	Rectus capitis lateral
Iliocostalis cervicis	Anterior scalene
Longissimus capitis	Middle scalene
Longissimus cervicis	Posterior scalene
Multifidus	Sternocleidomastoid
Semisplenius capitis	Omohyoid
Semisplenius cervicis	Sternohyoid
Splenius capitis	
Splenius cervicis	
Levator scapulae	
Rhomboid minor	
Trapezius	

3.2.1 Muscle Activation Schemes

A number of muscle activation schemes have been previously identified. The scheme containing flexors and extensors 100% activated (Shen and Cronin, 2017) exists in the current GHBMC model, and it was defined as “Maximum Muscle Activation (MMA)”. Two additional activation schemes were also named: no muscle activation (NMA), containing extensors and flexors at 0% activated, and the Cocontration Muscle Activation scheme (CMA), corresponding to maintaining the head in a neutral posture. The NMA scheme could represent the response of PMHS or represent a lower bound activation scheme, while the CMA scheme was hypothesized to represent the reflex startle response in the model. The CMA scheme was obtained by an initial linear optimization for the extensor with a reduction of head movement to a minimum as the target when no impact was imposed in the model. Following the nomenclature of the other schemes, the activation obtained through optimization was called the Optimized Muscle Activation (OMA).

3.2.2 Muscle Activation Onset Time

The activation time range used in the muscle optimization was 55 to 99 ms, based on reported values for the sternocleidomastoid and trapezius in a series of rear impacts and frontal impacts sled tests conducted with volunteers (Blouin et al., 2003; Foust et al., 1973; Hernández et al., 2006; Magnusson et al., 1998; Ono et al., 1997; Siegmund et al., 2002; Snyder et al., 1975). In addition, the GHBMC M50-O neck muscles had a default activation onset time activation of 74 ms based on an average from literature. This default onset time activation was used when the pre-optimization studies were performed to determine the activation level range for the optimization.

3.2.3 Muscle Activation Magnitude

The neuronal signal was represented as a percentage of the maximum (100%), corresponding to the maximum activation level possible for a given muscle. The GHBMC M50-O neck muscles had

a default activation curve based on a neural input signal of 100% (Figure: 2-31). The activation level could be scaled by changing this percentage in the muscle groups in the model.

Initially, data from frontal impact sled tests with recorded EMG muscle activity were reviewed. As the only direct activation data available used MVC and EMG data, which has limitations on representing activation magnitudes, a pre-optimization study was conducted to define the ranges of muscle activation levels used in the optimization.

3.3 Pre-optimization of Muscle Activation for Impact Simulations

Prior to the full optimization, some understanding of the sensitivity of the head-and-neck model to the activation magnitude and onset time parameters needed to be observed to better define the process constraints. The previous understanding is necessary due to the multitude of kinematics analyzed that, in combination with the number of variables, results in many possible solutions to the same problem. The unique solution was achieved by a pre-optimization study that consisted of impact simulations of the model with variations of the parameters for the different impact scenarios. The resultant head kinematics from the simulations were compared to experimental data and culminated in the exclusion of less sensitive parameters as well as enhanced clarity in the model behaviour.

3.3.1 Frontal Impact Activation Parameter Investigation

The frontal impact (Figure 3-4) was applied in the model as X linear velocity (Figure 2-18) and Y rotational displacement (Figure 2-19) of T1 extracted from the NBDL experiments for the 2g, 3g, 6g, 8g, 10g, 12g, 13g, 14g, and 15g severities.

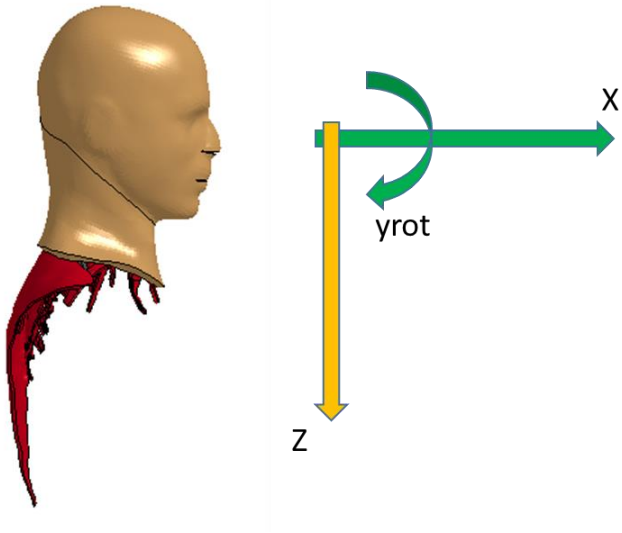

Figure 3-4: Frontal impact optimization direction of the kinematic parameters. The displacement and acceleration in the green directions were the objectives of the optimization.

A pre-optimization study was carried to define the range of muscle activation levels used during the optimization. Initially, the sensitivity of the kinematic response of the flexors was tested using frontal impact simulations with 2g, 8g, and 15g severities with this muscle group activation level varying from 0% to 100%, in intervals of 20%, and with a constant activation of the extensor muscles of 10%. This was necessary to test the hypothesis that, due to their location and low strength, the flexors would not affect the impact kinematics in frontal impact scenarios.

The next step was to simulate frontal impact with 2g, 3g, 6g, 8g, 10g, 12g, 13g, 14g, and 15g varying the extensor activation levels from 0% to 100%, in intervals of 20%, maintaining the flexor muscles with the default activation of 100%. The MMA, CMA and NMA were also simulated for all the frontal impact severities and compared to the other activation schemes.

3.3.2 Lateral Impact Activation Parameter Investigation

The lateral impact (Figure 3-5) was applied in the model as Y linear velocity (Figure 2-22) and X rotational displacement (Figure 2-23) of T1 extracted from the NBDL experiments for the 4g, 5g, 6g, and 7g severities.

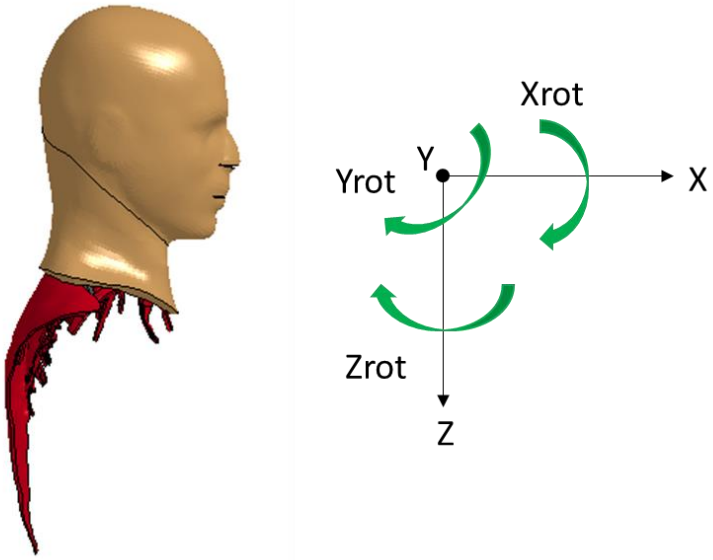

Figure 3-5: Lateral impact optimization direction of the kinematic parameters. The displacement and acceleration in the green directions were the objectives of the optimization.

Similar to the frontal case, a pre-optimization study was carried to define the range of muscle activation levels used during the optimization. Due to the higher complexity of this movement in comparison to the frontal impact, the flexors were not set to a constant activation value. Right side struck lateral impacts with 4g, 5g, 6g, and 7g were simulated using the MMA, CMA and NMA. These other activation schemes were selected after observing the response of the lateral impact without any activation and inferring what muscle groups would resist the movement. Also, these activation schemes were selected to observe the influence of varying only the extensors activation, similar to the frontal

impact. For this pre-optimization study, the muscles were divided into four groups right extensor, right flexors, left extensors and left flexors so a more detailed activation scheme could be obtained.

3.3.3 Rear Impact Activation Parameter Investigation

The rear impact (Figure 3-6) was applied in the model as X linear acceleration (Figure 2-26), Z linear acceleration (Figure 2-27) and Y rotational displacement (Figure 2-28) of T1 extracted from volunteer sled experiments for the 3g and 4g severities (Sato et al., 2014). It was necessary to use a different experimental data set as the NBDL data were conducted with PMHS which do not present muscle response and could not be used for analyzing the kinematic response to muscle activation.

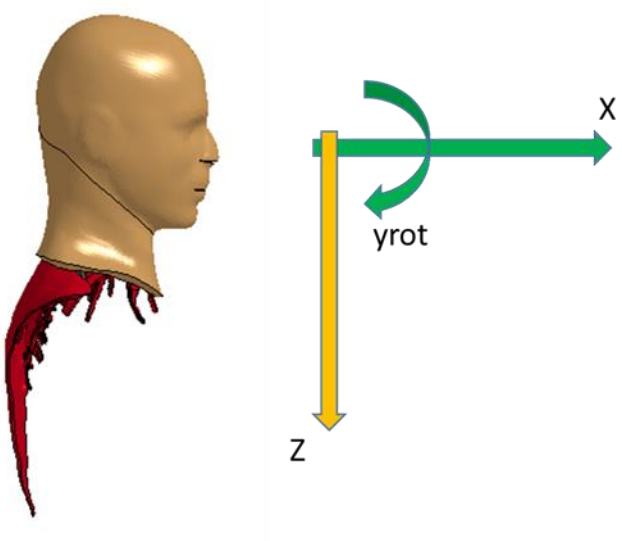

Figure 3-6: Rear impact optimization direction of the kinematic parameters. The displacement and acceleration in the green directions were the objectives of the optimization.

Similar to the frontal case, a pre-optimization study was carried to define the range of muscle activation levels used during the optimization. The 3g and 4g impacts were simulated using the MMA, CMA and NMA. These other activation schemes were selected after observing the response of the lateral impact without any activation and inferring what muscle groups would resist the movement.

Also, the contraction activation schemes with 55 ms onset time for the flexors were simulated to observe the influence of changes in activation times.

3.4 Optimization of Muscle Activation for Impact Simulations

The neck model was optimized for three different loading scenarios (frontal, lateral and rear), by varying the muscle activation onset time and activation magnitude. The optimization was undertaken using commercial software (LS-OPT, R.5.2.1, LSTC, Livermore, CA) with a linear polynomial optimization method, D-optimal point selection and domain reduction (Figure 3-7). The optimization methodology was derived from other neck muscle optimizations presented in the literature (Ivancic and Pradhan 2017; Dibb et al. 2013). The models were solved using the commercial FE software and the resulting curves of head kinematics were analyzed during this process. The muscle activation time range for the optimization, 55 to 99 ms, was based on reported values for the trapezius and sternocleidomastoid.

3.4.1 Optimization of Active Musculature for Frontal Impact Schemes

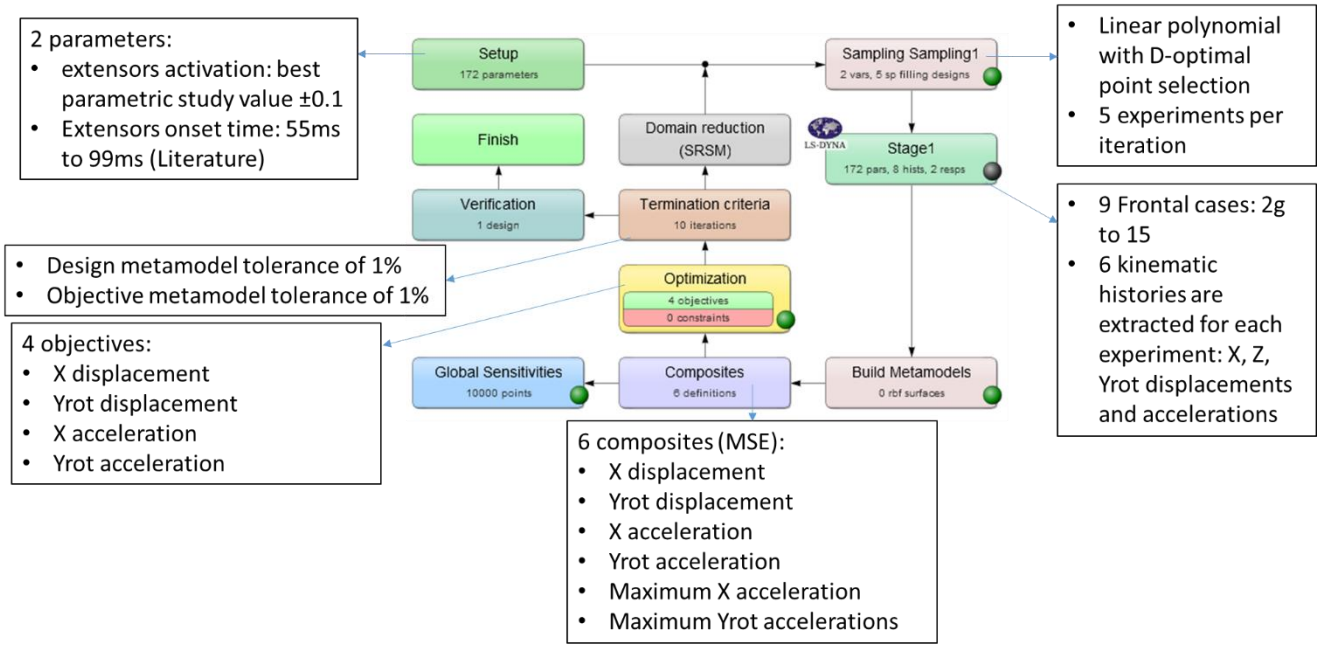

Figure 3-7: Frontal impact optimization process based on the LS-OPT user interface.

For the frontal impact, the optimization consisted of obtaining the combination of extensors activation level and onset time for each severity that produced the lowest average root mean square error (MSE) between the simulated kinematic response curves and the NBDL kinematic data.

The variation for the extensors activation was based on the results from the pre-optimization study (Table 4-1). The kinematics assessed were the X-linear displacement, Y-rotational displacement, X-linear acceleration, and Y-rotational acceleration for each of the simulations inside each optimization iteration. The optimization was considered converged when the average of the MSE values varied less than 1%.

3.4.2 Optimization of Active Musculature for Lateral Impact Schemes

The lateral impact optimization, using a similar procedure of the frontal activation, consisted of obtaining the combination of unique activation levels and onset times for each one of the four muscle

groups (right extensors, left extensors, right flexors, and left flexors) for the 4g and 7g severities that produced the lowest average MSE between the simulated kinematic response curves and the NBDL kinematic data. For the other impact severities, the parameters were interpolated and simulated.

The variation for the muscle group activations was 0 to 100%. The kinematics assessed were the X-rotational displacement, Y-rotational displacement, Z-rotational displacement, X-rotational acceleration, Y-rotational acceleration, and Z-rotational acceleration for each of the simulations inside each optimization iteration. The optimization was considered converged when the average of the MSE values varied less than 1%.

3.4.3 Optimization of Active Musculature for Rear Impact Schemes

The rear impact optimization, similarly to the frontal optimization process, consisted of obtaining the combination of unique activation levels and onset times for each one of two muscle groups (extensors and flexors) for the 3g severity that produced the lowest average MSE between the simulated kinematic response curves and the experimental kinematic data.

The response was not sensitive to changes in onset time and both muscle groups were set to start activating at 74 ms. The variation for the extensors and flexors activation was 0 to 100%. The kinematics assessed were the X-displacement and Y-rotational displacement for each of the simulations inside each optimization iteration. The accelerations were not considered as the Y-rotational acceleration was not present in the experimental data and adding the X-acceleration to the analysis could bias the optimization in this direction. The optimization was considered converged when the average of the MSE values varied less than 1%.

3.5 Assessment of Model Response using Correlation Rating

During the pre-optimization and optimization studies, the correlation of the kinematic results with the experimental data was obtained using a correlation rating software (CORA, Partnership for

Dummy Technology and Biomechanics, R. 3.6.1, Germany). For the frontal case, the parameters identified from the pre-optimization study to calculate the correlation rating were the X-linear displacement, Y-rotational displacement, Z-linear displacement, X-linear acceleration, Y-rotational acceleration and Z-linear acceleration. For the lateral case, the parameters identified from the pre-optimization study to calculate the correlation rating were the X-linear displacement, Y-rotational displacement, Z-linear displacement, X-linear acceleration, Y-rotational acceleration and Z-linear acceleration. For the rear case, the parameters identified from the pre-optimization study to calculate the correlation rating were the X-linear displacement, Y-rotational displacement, Z-linear displacement, X-linear acceleration and Z-linear acceleration. There were more kinematics used in the correlation analysis for frontal, lateral and rear were than used in the optimization, so the study response could be accessed more broadly and certified if it was improving the overall response, not only the main ones.

The final correlation rating was calculated as an average of the individual scores for each kinematic parameter (Equation (11). These individual scores considered a corridor rating (C) and a cross-correlation rating with equivalent weights. The corridors were defined as one and two standard deviations from the experimental data. The cross-correlation rating, on the other hand, was calculated as a weighted average of the response phase (P), shape (V) and size (S). Their respective weights were G_p = 0.25, G_v = 0.50 and G_s = 0.25.

$$\boldsymbol{Correlation\ rating} = \frac{\mathbf{1}}{\mathbf{2}}.\boldsymbol{C} + \frac{\mathbf{1}}{\mathbf{2}}.\left(\boldsymbol{G_v}.\boldsymbol{V} + \boldsymbol{G_s}.\boldsymbol{S} + \boldsymbol{G_p}.\boldsymbol{P}\right) \quad \textbf{(11)}$$

Chapter 4: Results

4.1 Frontal Impact Muscle Activation Strategy and Comparison to Experimental Data

4.1.1 Kinematic Sensitivity to Flexor Muscle Activation

A set of initial simulations were conducted to identify the sensitivity of the model to the flexors activation with their level varying from 0% to 100%, maintaining the extensors with constant low activation. The simulations indicated that the model response was not sensitive to the flexor activation level for impact severities above 3g. This result was reasonable as only the extensors were antagonistic to the head impact response, and the lower strength of the flexors to the extensors (Figure 4-1).

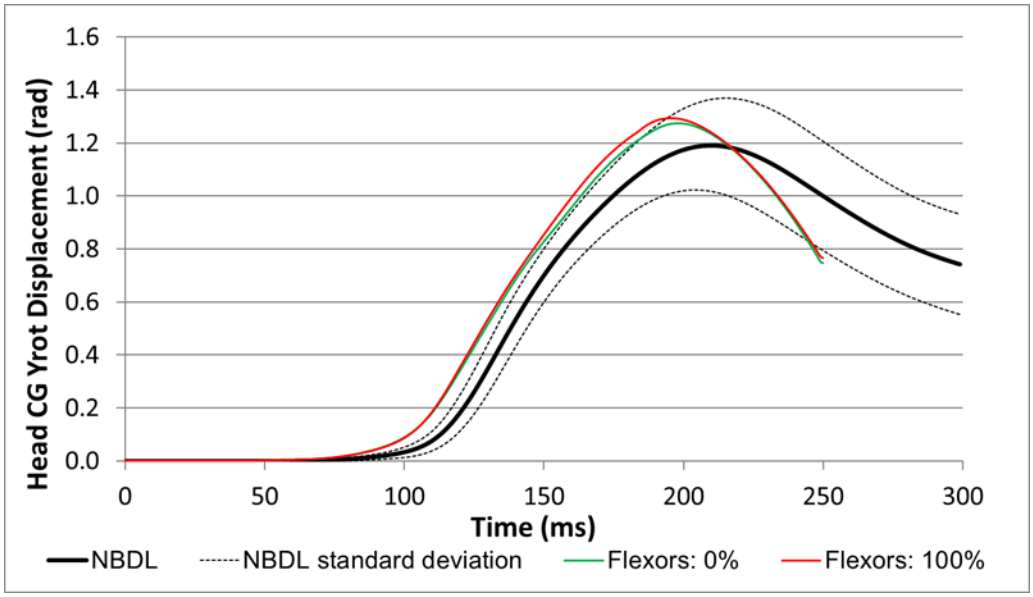

Figure 4-1: Different activation levels for the flexors with a constant activation level of 10% for the extensors in the 8g frontal impact.

For the lower impact severities, below 3g, flexor activation generated a significant contribution to the head impact global kinematic response (Figure 4-2). In addition, the extensor and flexor activation ratio with the best fit to the experimental data was 1:1 (NMA scheme) for lower impact accelerations, which is different from the one presented by the higher severity cases.

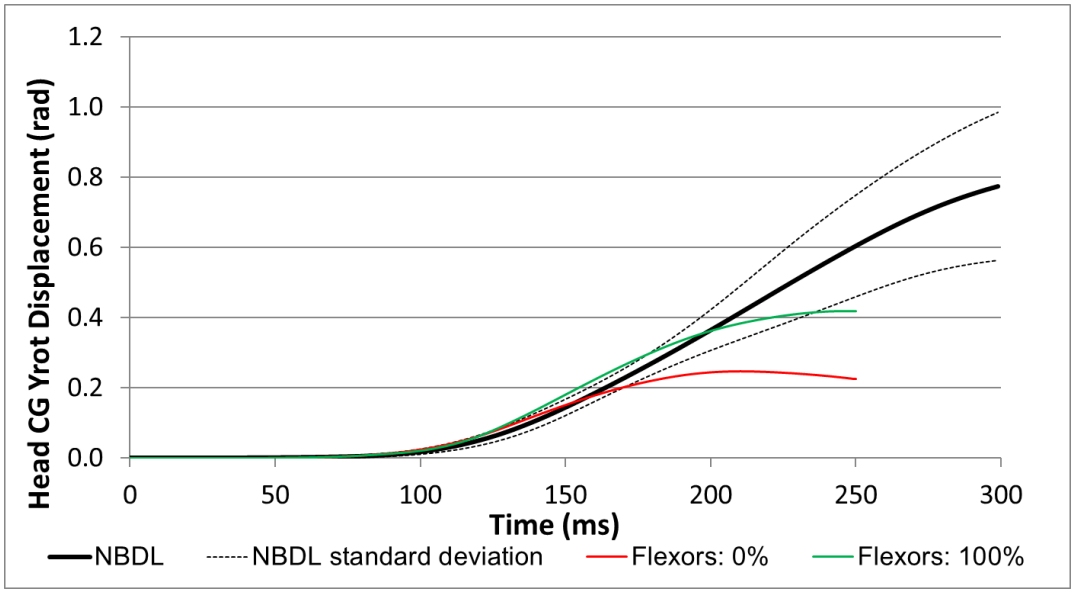

Figure 4-2: Different activation levels for the flexors with a constant activation level of 10% for the extensors in the 2g frontal impact.

4.1.2 Pre-optimization Study of Impact Kinematics

The head-and-neck model was assessed for nine frontal impact severities and compared to the human volunteer data in a series of initial pre-optimization simulations. The pre-optimization study provided approximate activation values for each impact severity and served to identify the boundary values used in the optimization study (Table 4-1).

Table 4-1: Pre-optimized muscle activation level for varying frontal impact severity.

Impact severity (g)	Extensor activation scaling	Flexor activation scaling
2	0.0	1.0
3	0.0	1.0
6	0.2	1.0
8	0.2	1.0
10	0.4	1.0
12	0.4	1.0
13	0.4	1.0
14	0.6	1.0
15	0.6	1.0

The CMA was a single activation scheme, a subset of the cases considered, where the head remained in a neutral position when the muscles were activated with no external loading applied. This activation scheme presented a good correlation with the experimental data for all the severities reinforcing the startle activation hypothesis (Figure 4-3). As predicted, the NMA had a better correlation to lower severity impacts and the MMA had a better correlation with high severity impacts. The preliminary study also indicated a possible direct relation between impact acceleration and extensor muscle activation levels.

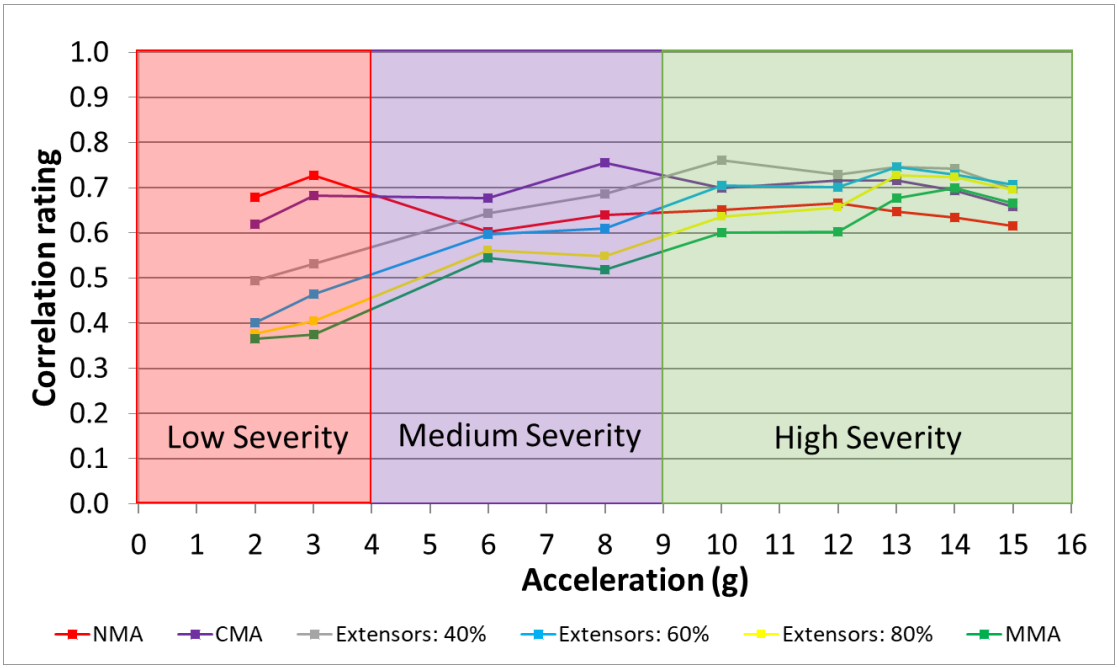

Figure 4-3: Correlation rating to the experimental data for different muscle activation schemes for frontal impacts ranging from 2g to 15g.

4.1.3 Frontal Impact Optimization Analysis

The neck model muscle activation strategy was optimized for activation level and activation onset time for the frontal impact cases. A primary output of the optimization analysis was response surfaces showing the relationship between the two variables in relation to the experimental data, expressed as MSE. The response surfaces allowed for a more in-depth understanding of the relation between the two variables analyzed: activation level and onset time. It was observed that for 2g and 8g, the OMA was at the earliest activation onset time and that the shape of the surfaces indicated a better numerical solution may stand outside the physiological time boundaries (Figure 4-4 and Figure 4-5).

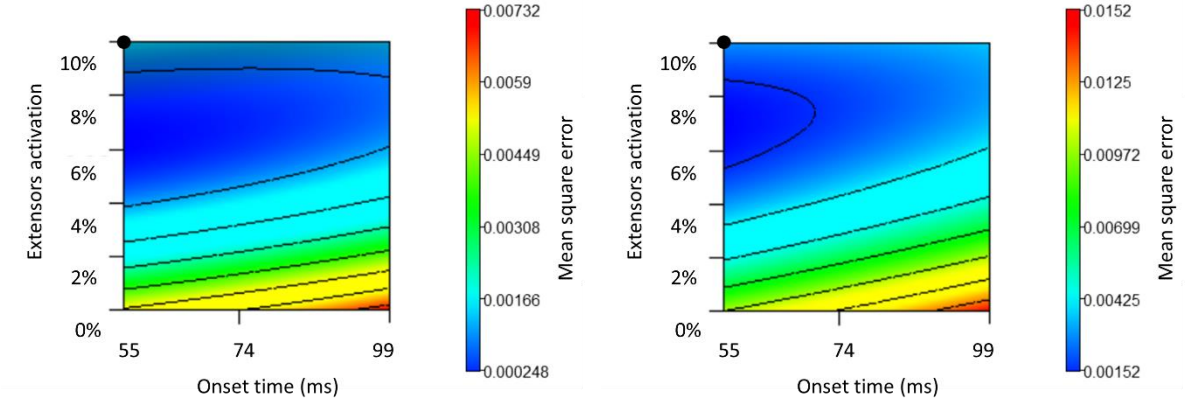

Figure 4-4: Response surfaces of X-displacement (left plot) and Y-rotational displacement (right plot) for the 2g frontal impact optimization. The black dot represents the optimum response.

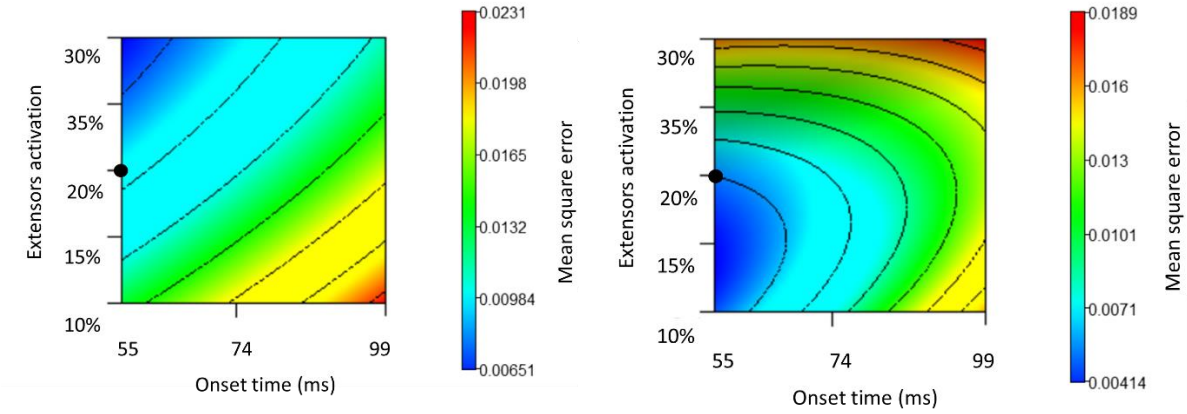

Figure 4-5: Response surfaces of X-displacement (left plot) and Y-rotational displacement (right plot) for the 8g frontal impact optimization. The black dot represents the optimum response.

However, for the 15g frontal impact, the optimum activation was at 77.85 ms onset time due to the influence of the head Y-rotation response (Figure 4-6). The X-displacement response indicated the same trend as the 2g and 8g acceleration, and a similar kinematic response for the model could still

be produced by lower onset times because of the small changes they generate in the average MSE for higher severity impacts.

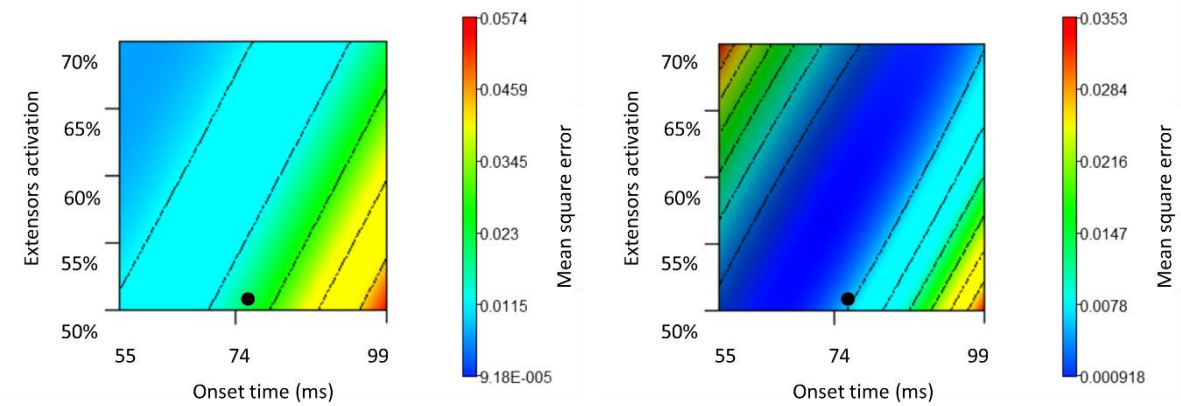

Figure 4-6: Response surfaces of X-displacement (left plot) and Y-rotational displacement (right plot) for the 15g frontal impact optimization. The black dot represents the optimum response.

It was observed that the Y-rotational acceleration response was the most affected by the changes in the activation level and onset time, and carried the most weight in defining the OMA scheme followed by the X-acceleration (Figure 4-7).

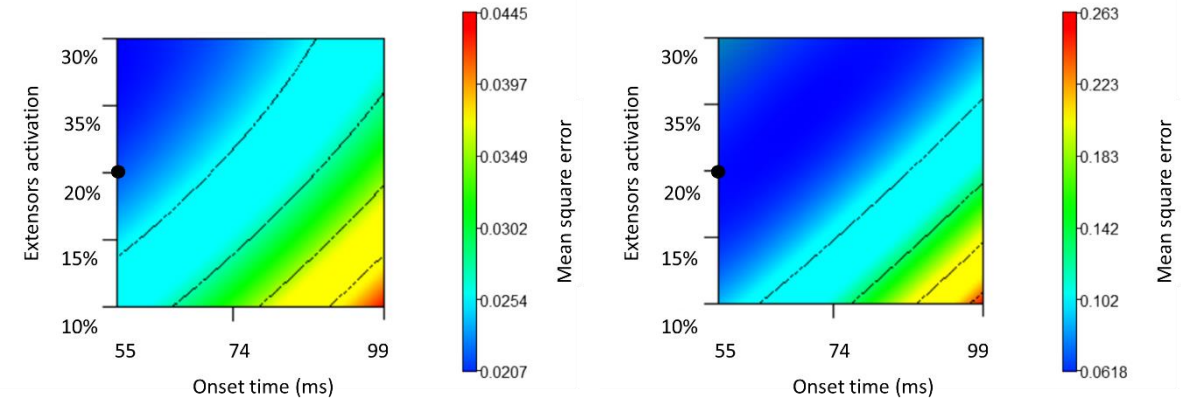

Figure 4-7: Response surfaces of the X-acceleration (left plot) and Y-rotational acceleration (right plot) for the 2g frontal impact optimization. The black dot represents the optimum response.

The global sensitivities of the model to each input variable were generated during the optimization process, reported as the percent contribution of each variable to the response. For each impact severity, the sensitivities followed a similar trend for all kinematics analyzed. It was observable that, for lower severities, the extensors activation magnitude contribution was the highest, but as the severity increased the onset time contribution also increased (Figure 4-8, Figure 4-9 and Figure 4-10).

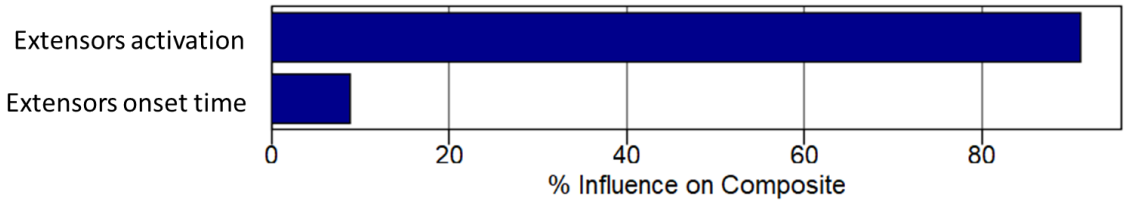

Figure 4-8: Influence of each optimization parameter in the Y-rotational displacement for the 2g frontal impact simulation.

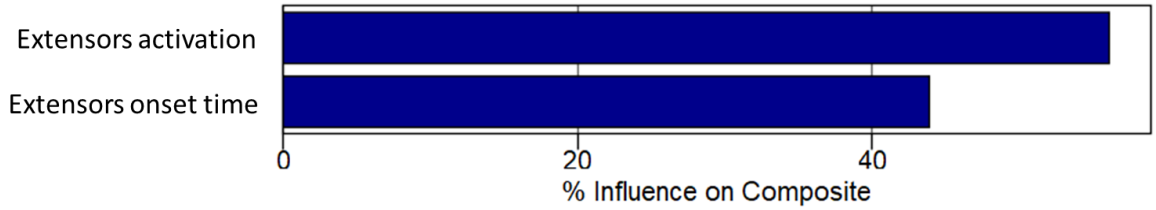

Figure 4-9: Influence of each optimization parameter in the Y-rotational displacement for the 8g frontal impact simulation.

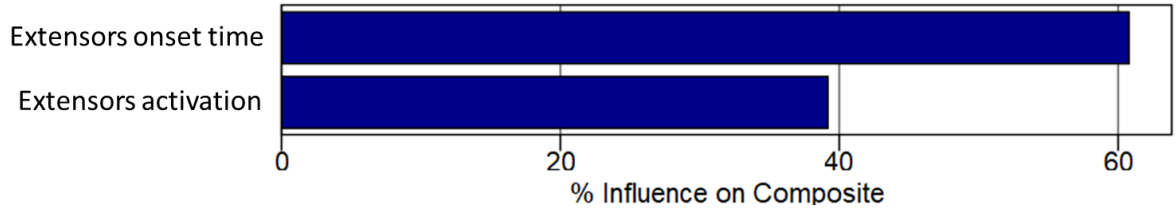

Figure 4-10: Influence of each optimization parameter in the Y-rotational displacement for the 15g frontal impact simulation.

4.1.4 Optimized Frontal Impact Muscle Activation Parameters

The optimization study was undertaken for each of the nine frontal impact severities to identify the specific extensor activation resulting in the highest correlation with the corresponding experimental result (Table 4-2).

Table 4-2: Optimized extensor muscle activation level and activation onset time for each frontal impact case (flexors level at 100% and onset time at 74 ms).

Impact severity (g)	Extensors activation scaling	Extensors onset time (ms)
2	0.10	55.00
3	0.10	55.00
6	0.24	55.00
8	0.19	55.00
10	0.30	78.38
12	0.33	68.63
13	0.40	64.04
14	0.58	81.10
15	0.51	77.85

The OMA schemes, as identified in the pre-optimization study, indicated that the extensors muscle activation increased with increasing impact severity. The increase in activation of the extensors was fit to an exponential function with a coefficient of determination (R^2) of 0.93 (Figure 4-11).

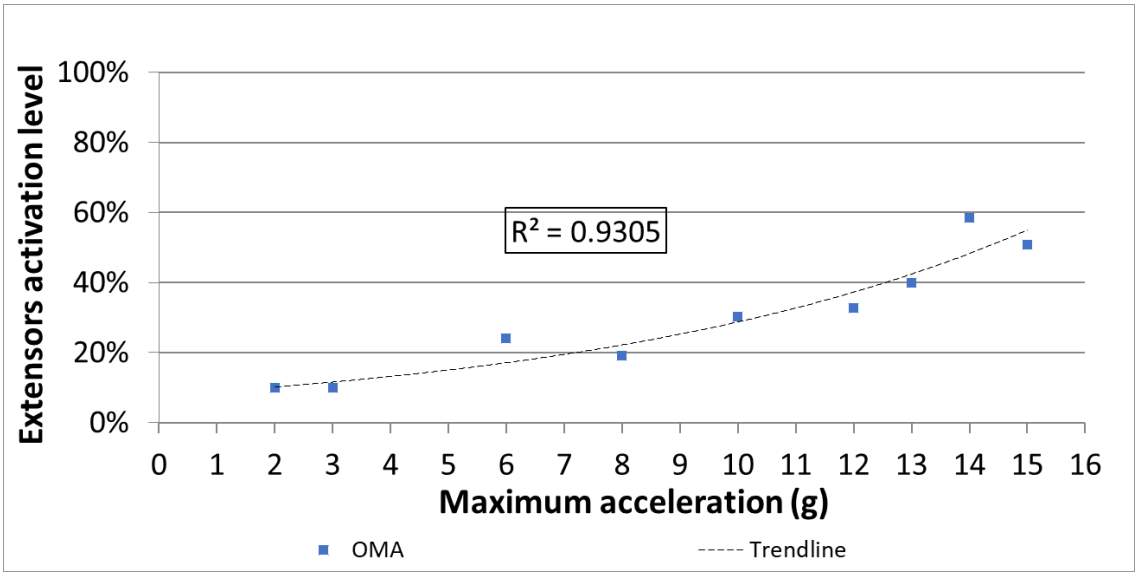

Figure 4-11: Optimized extensor muscle activation level demonstrating increasing trend in activation with increasing frontal impact severity.

All OMA onset times occurred at the lower limit of 55 ms for impact severities at or below 8g, indicating an earlier onset time was desired (Figure 4-12). However, the lower boundary was maintained at 55 ms, which was the lowest published value for measured activation time in humans. There was no observable trend for the OMA times for the higher severity impact cases, and the onset times ranged from 64 to 81 ms. This variation was attributed to the lower sensitivity of the high severity impact cases to onset time.

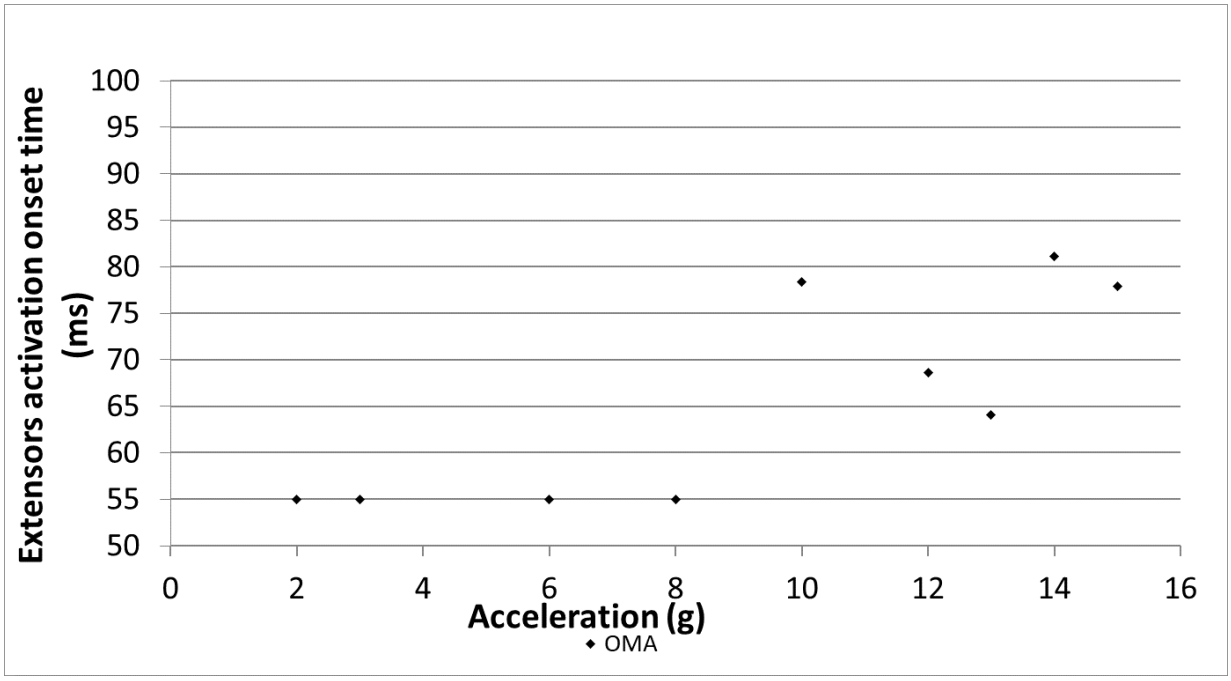

Figure 4-12: Optimized extensor muscle activation onset time.

4.1.5 Correlation of Frontal Impact Kinematics with Experimental Data

The correlation of the head center of mass kinematics using the OMA scheme with the volunteer data was higher than all other muscle activation schemes, for all severities investigated. The correlation analysis of the head kinematic response to the experimental data indicated an improvement of 23% of the CMA relative to the MMA scheme (from 0.561 to 0.691) (Figure 4-13). The OMA schemes provided an overall improvement of 35% in correlation to the activation scheme of the original model (0.561 to 0.755, respectively fair and good biofidelity according to ISO/TR9790) reaching a maximum improvement of 103% for the optimized 3g impact case.

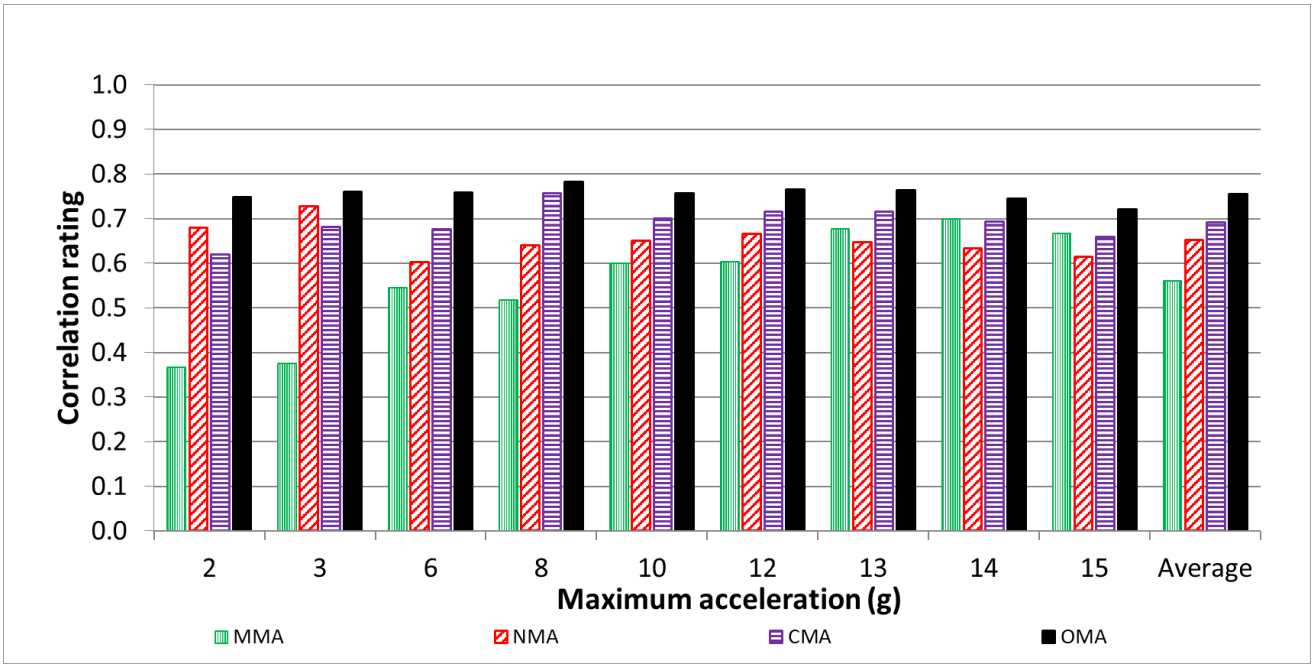

Figure 4-13: Correlation of muscle activation strategies to the experimental data for rear impacts ranging from 2g to 15g.

The NMA case presented an average correlation rating close to the CMA mainly because of the 2g and 3g responses (Figure 4-13).

4.2 Lateral Impact Muscle Activation Strategy and Comparison to Experimental Data

4.2.1 Pre-optimization Study of Impact Kinematics

The head-and-neck model was assessed for four lateral impact severities and compared to the human volunteer data. The lateral impact pre-optimization study indicated a relationship between impact acceleration and extensors activation level (Table 4-3), similar to the frontal impact study. It was also noted that the NMA scheme demonstrated a good correlation for lower severity impacts (Figure 4-14).

Table 4-3: Pre-optimization activation levels for varying lateral impact severity.

Impact severity (g)	Right extensor activation scaling	Right flexors activation scaling	Left extensor activation scaling	Left flexors activation scaling
2	0.0	0.0	0.0	0.0
3	0.0	0.0	0.0	0.0
6	0.2	1.0	0.2	1.0
8	0.4	1.0	0.4	1.0

The CMA presented a good correlation with the experimental data for the majority of the severities reinforcing the startle activation hypothesis. An alternative activation scheme, with right extensors and left flexors not activated while the left extensors were activated in 20% and the right flexors activated in 100%, presented a slight improvement in the correlation rating compared to the CMA scheme.

The apparent important contribution of all the four muscle groups, with the added complexity of the possible different combinations of onset times, made it challenging to reduce the parameter boundaries of the optimization and, because of that, the same optimization range of the activation level was used for all muscles, varying from 0 to 100% activation.

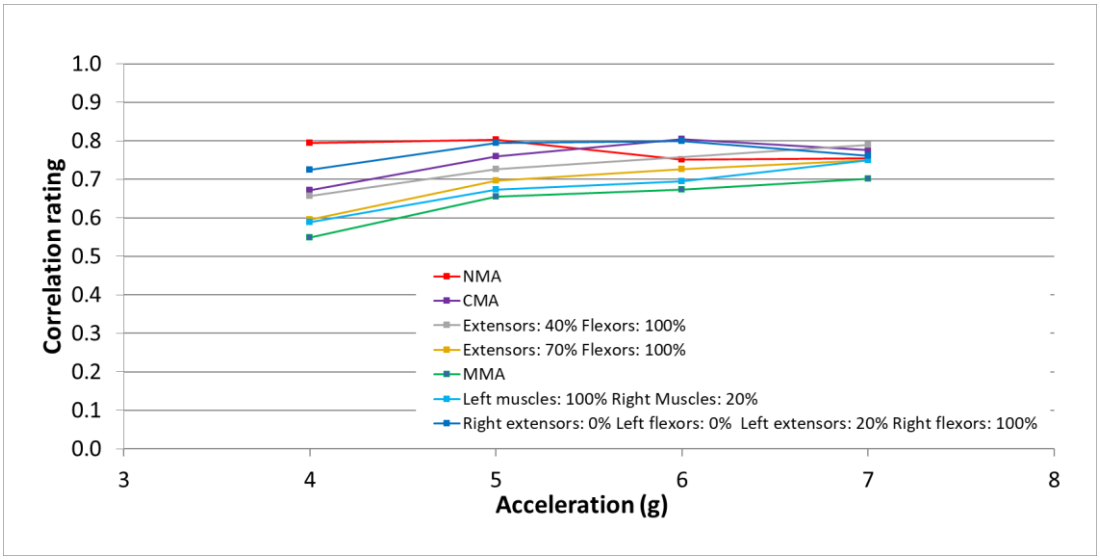

Figure 4-14: Correlation to the experimental data for different muscle activation schemes for lateral impacts ranging from 4g to 7g.

4.2.2 Lateral Impact Optimization Analysis

The neck model muscle activation strategy was optimized for activation level and activation onset time for the lateral impact cases. A primary output of the optimization analysis was response surfaces (Figure 4-15); however, due to the number of variables and kinematics for each lateral impact were more complex in shape relative to the frontal impact scenario.

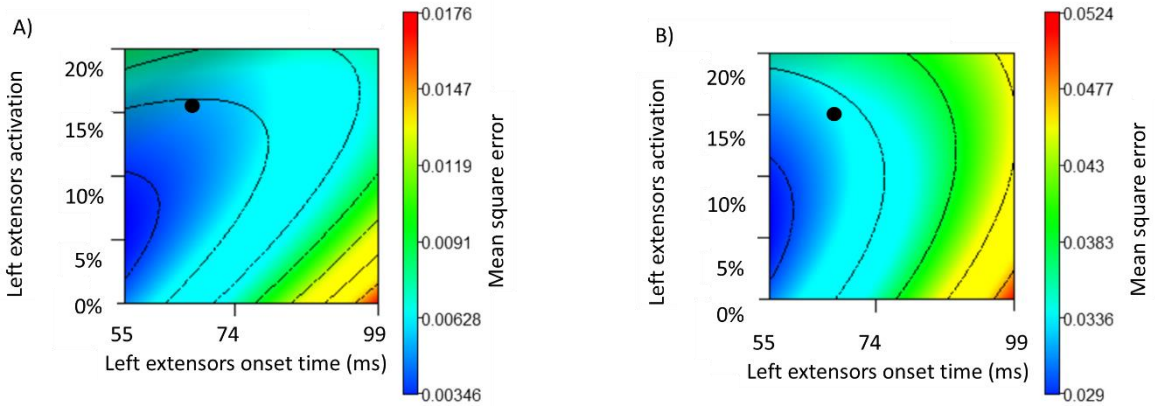

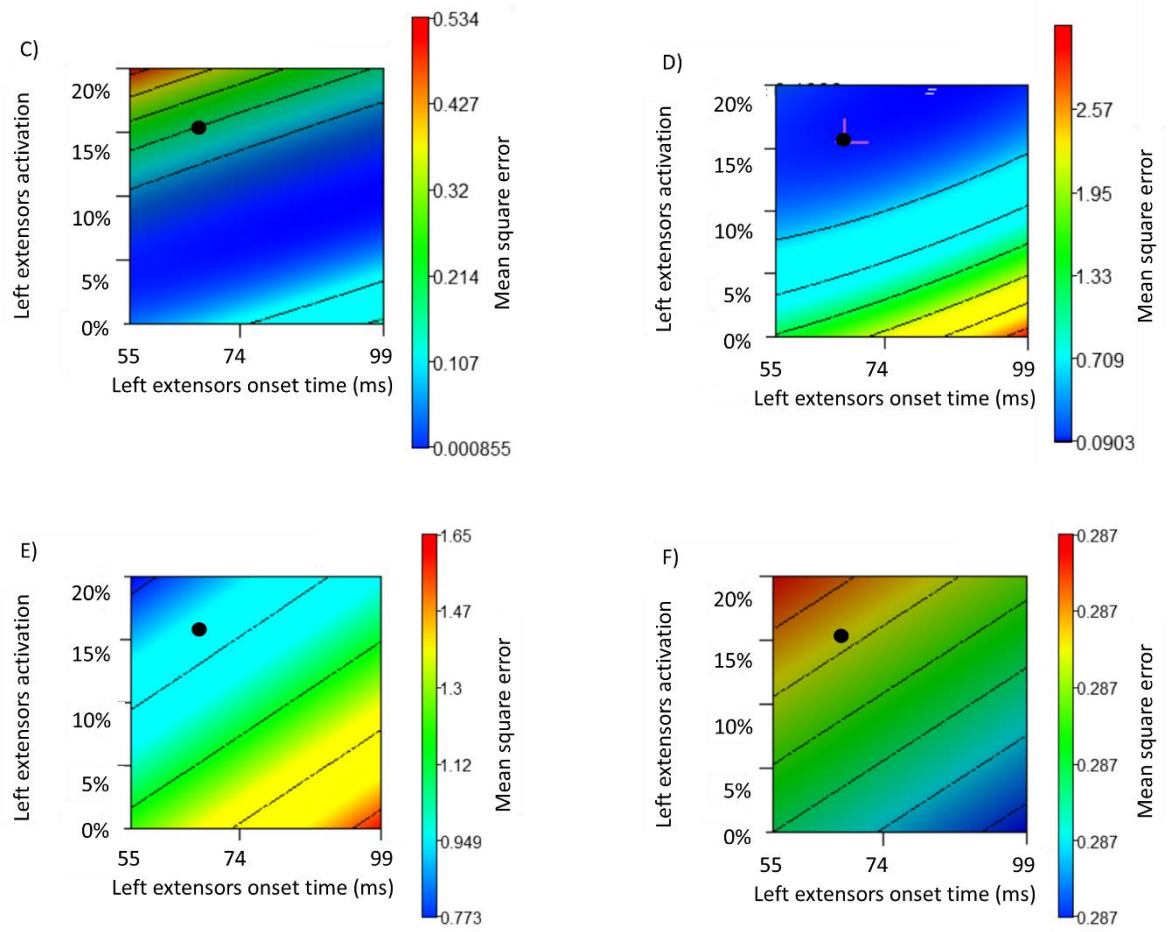

Figure 4-15: Response surfaces of X-rotational displacement (A), X-rotational acceleration (B) Y-rotational displacement (C), Y-rotational acceleration (D), Z-rotational displacement (E), and Z-rotational acceleration (F) for left extensors in 3 iterations of the 4g frontal impact optimization. The black dot represents the optimum response.

To further investigate the effect of activation magnitude and onset time on the resulting head kinematics, the global model sensitivities were generated during the optimization process. The sensitivity was quantified as the percent contribution of each variable to the response. This allows for a more in-depth understanding of the relation between the eight variables analyzed. It was observed

that for all responses the left extensors activation contribution was the highest for the Y-rotational displacement (Figure 4-16) and Y-rotational acceleration (Figure 4-17) in the 4g impact case.

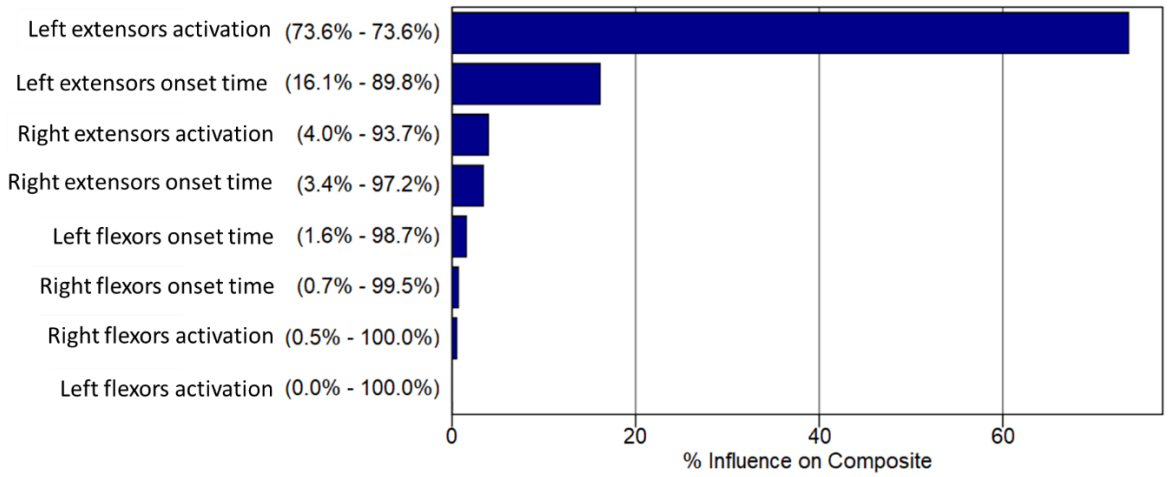

Figure 4-16: Influence of each optimization parameter on the Y-rotational displacement for the 4g lateral impact simulation

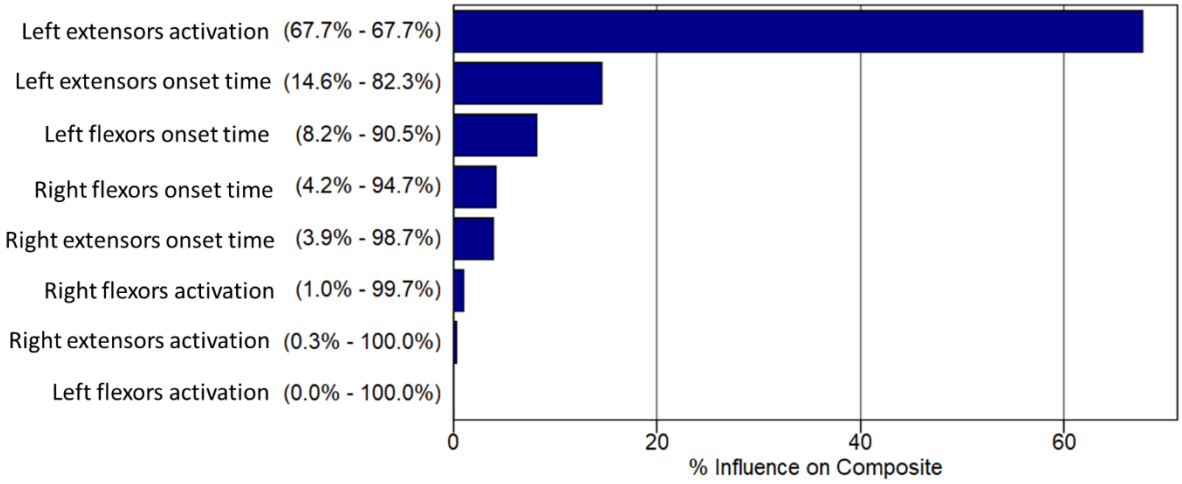

Figure 4-17: Influence of each optimization parameter on the Y-rotational acceleration for the 4g lateral impact simulation

Considering the X-rotational displacement (Figure 4-18) and X-rotational acceleration (Figure 4-19), the sensitivity was much more complex, with many of the parameters having a strong influence on the resulting kinematics.

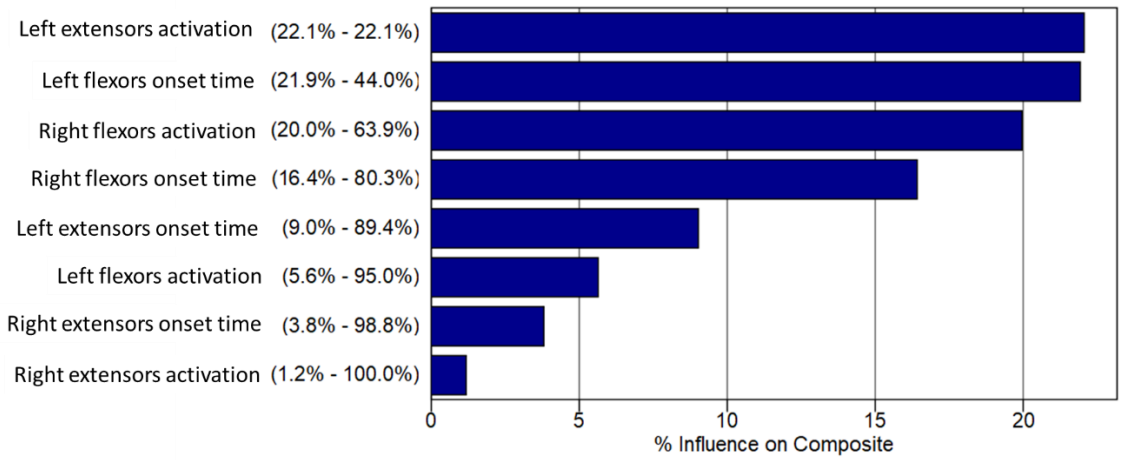

Figure 4-18: Influence of each optimization parameter on the X-rotational displacement for the 4g lateral impact simulation

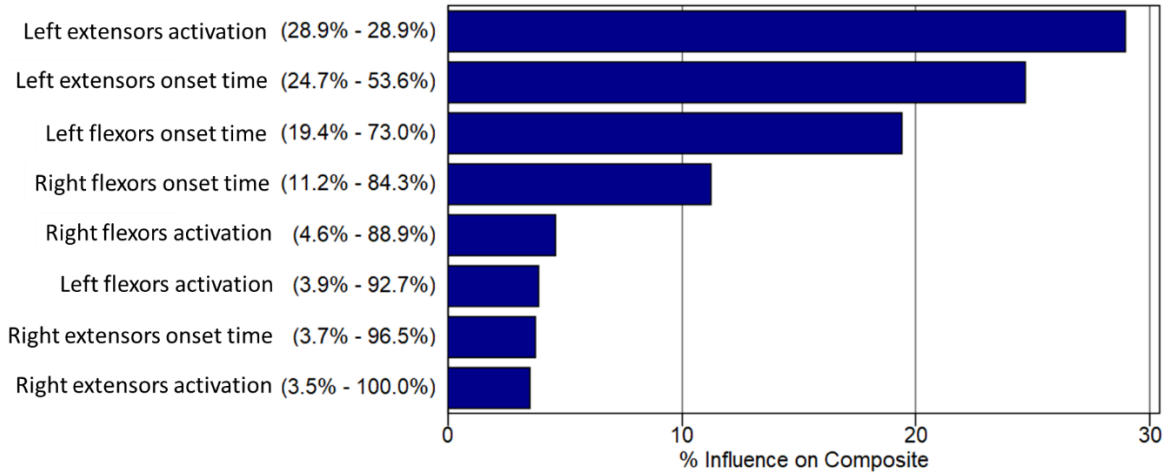

Figure 4-19: Influence of each optimization parameter on the X-rotational acceleration for the 4g lateral impact simulation

4.2.3 Optimized Lateral Impact Parameters

The optimization study was undertaken for each of the four lateral impact severities to identify the specific muscle activation resulting in the highest correlation with the corresponding experimental result (Table 4-4).

Table 4-4: Optimized muscle activation level and onset time for each lateral impact severity

Impact severity (g)	4	5	6	7
Right extensors activation scaling	0.10	0.08	0.05	0.02
Right flexors activation scaling	0.98	0.99	0.99	1.00
Left extensors activation scaling	0.11	0.12	0.13	0.14
Left flexors activation scaling	0.05	0.20	0.34	0.48
Right extensors activation onset time	64.38	61.45	58.52	55.59
Right flexors activation onset time	55.76	55.51	55.25	55.00
Left extensors activation onset time	63.19	60.65	58.11	55.57
Left flexors activation onset time	94.40	95.82	97.23	98.65

The resulting optimized OMA schemes demonstrated low extensor activation for the range of impact accelerations considered in this study. In contrast, the right flexors were highly activated in all cases, while the left flexors activation increased with increasing in impact severity (Figure 4-20). The optimized activation times were within the physiologic range reported in the literature. The activation onset times of the right and left extensors decreased with impact severity (Figure 4-21); however, the optimized flexor activation onset times were relatively constant across the range of impact severities. The left flexor activation time was approximately 95 ms, while the right flexor activation time was approximately 55 ms.

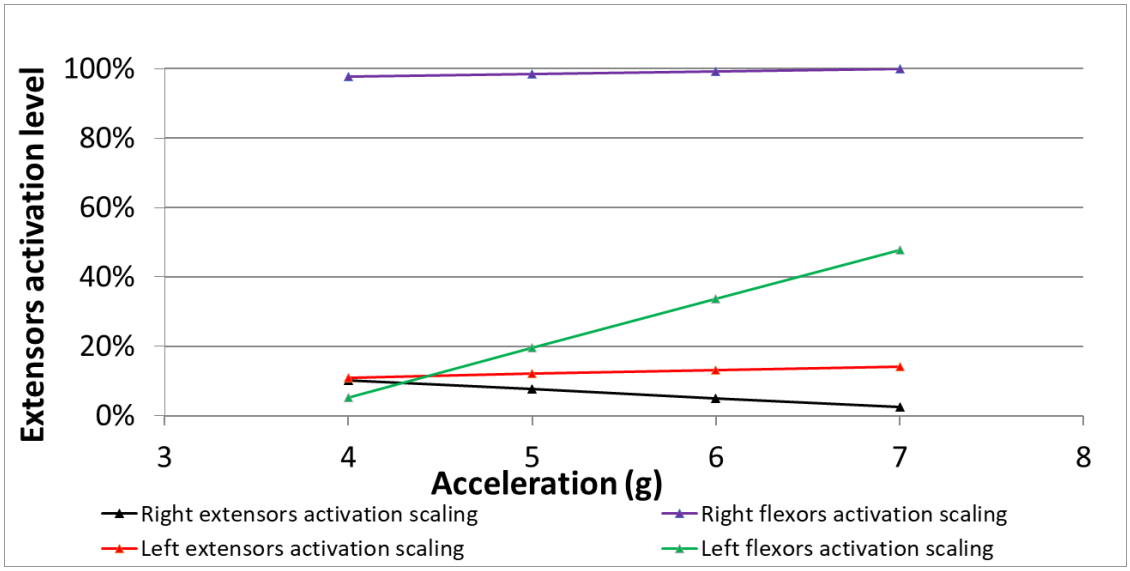

Figure 4-20: Optimized muscle groups activation level trends in lateral impact severity

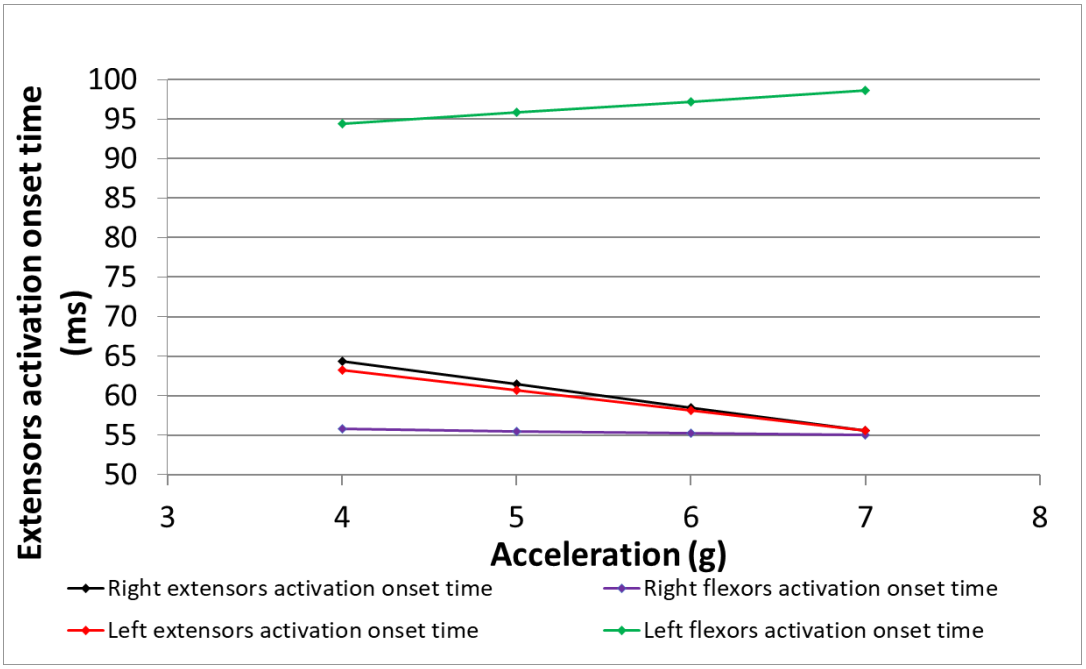

Figure 4-21: Optimized muscle groups activation onset time trends in lateral impact severity

4.2.4 Correlation of Lateral Impact Kinematics with Experimental Data

The correlation of the head center of mass kinematics with the lateral impact experimental data for the OMA scheme was higher than all other schemes for all severities simulated, as expected. The individually optimized OMA schemes provided an overall improvement of 25% in correlation relative to the MMA activation scheme (0.645 to 0.808, on average) corresponding to fair and good biofidelity according to ISO/TR9790. The maximum improvement in correlation was 46% for the optimized 4g lateral impact case.

The correlation analysis of the head kinematic response to the experimental data indicated an average improvement of 17% for the Cocotraction Muscle Activation relative to the MMA scheme (0.645 to 0.753, on average) (Figure 4-22).

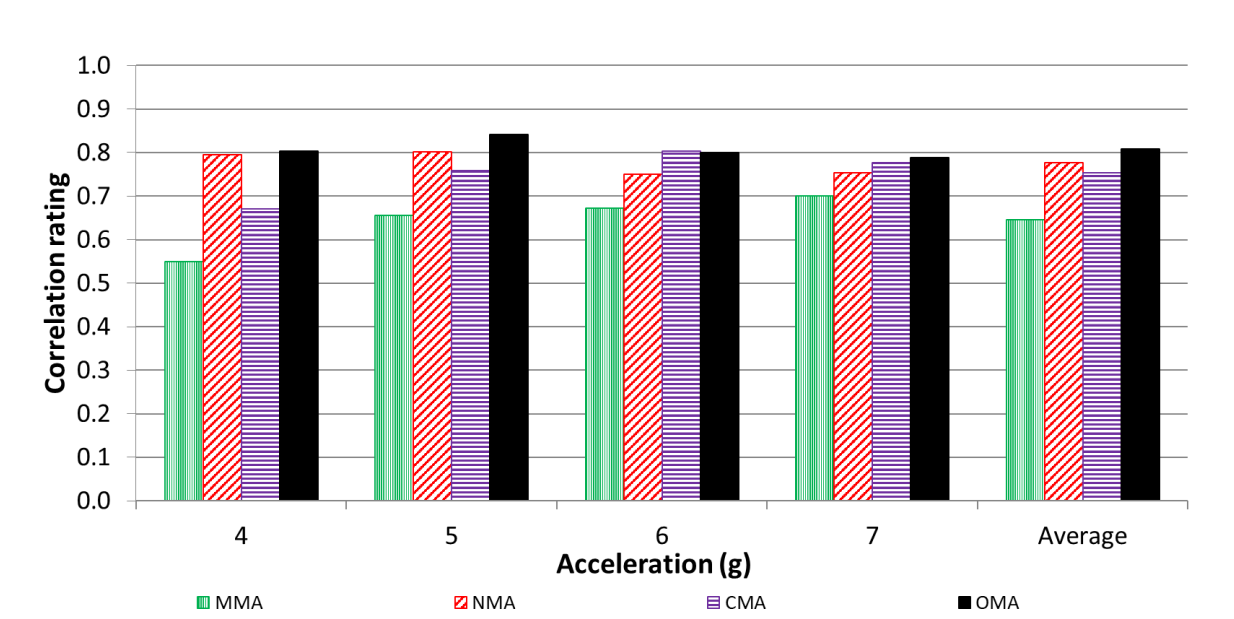

Figure 4-22: Correlation of muscle activation strategies to the experimental data for lateral impacts ranging from 4g to 7g.

The NMA (muscles not activated) case had an average correlation rating that was within 3% of the average correlation for the CMA. This small change was primarily associated with the higher

correlation of the lower severity cases and was similar to the trend observed in the frontal impact scenarios.

4.3 Rear Impact Muscle Activation Strategy and Comparison to Experimental Data

4.3.1 Kinematic Sensitivity to Flexor Activation Onset Time

A series of initial simulations were undertaken to develop an understanding of the sensitivity of the model to the flexor activation onset time varying from 55 ms to 74 ms. In this set of initial simulations, the extensor muscles had a constant low activation level (20%). The results identified that the model response presented a small sensitivity to the flexor onset time. This result was in agreement with what was observed in the lateral and frontal impact cases, where the change in onset times inside the range presented in the literature (55 to 99 ms) generated relatively small changes in the global kinematics (Figure 4-23).

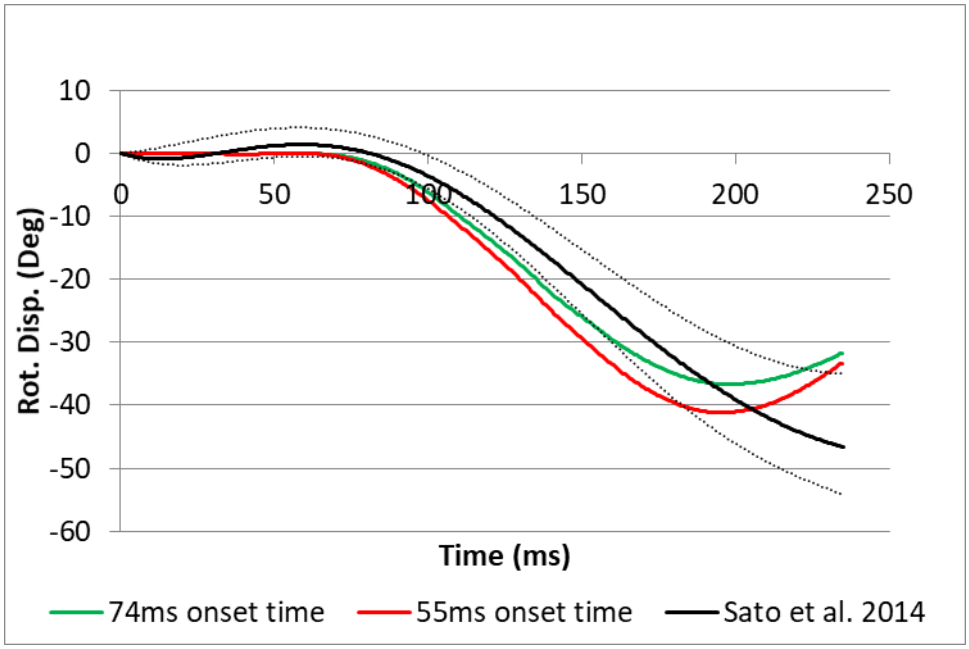

Figure 4-23: Y-rotational displacement of the head center of gravity for different flexor activation onset times, with a constant activation level of 20% for the extensors in the 3g rear impact.

4.3.2 Pre-optimization Study of Impact Kinematics

The head-and-neck model was assessed for the two rear impact severities and compared to the human volunteer data in a set of pre-optimization simulations. The initial parametric study provided approximate activation values for each impact severity (Table 4-5), but the limited number of accelerations tested did not permit an in-depth analysis of the muscle activation through different severities.

Table 4-5: Pre-optimization activation levels for two rear impact cases

Impact severity (g)	Number of individual experiments	Extensor activation scaling	Flexor activation scaling
3	12	0.0	0.0
4	10	0.0	0.0

The NMA strategy demonstrated the highest correlation rating to the experimental data, while the CMA strategy presented similar values.

4.3.3 Rear Impact Optimization Analysis

The neck model muscle activation strategy was optimized for activation level and activation onset time for the two rear impact cases. A primary output of the optimization analysis was response surfaces. In the rear impact scenarios, the X-displacement and Y-rotation were investigated as the primary kinematics and demonstrated similar MSE responses (Figure 4-24).

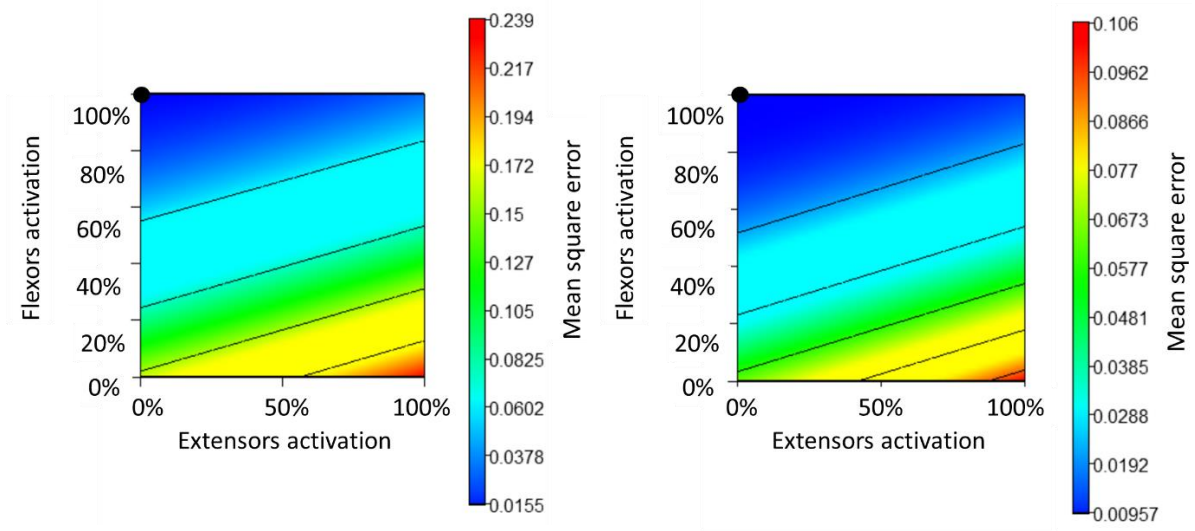

Figure 4-24: Response surfaces of the X-displacement (left plot) and Y-rotational displacement (right plot) for the 3g rear impact optimization. The black dot represents the optimum response.

The global sensitivities were generated during the optimization process measuring the percent contribution of each variable to the response was calculated (Figure 4-25). It was noted that the extensor muscles had a low contribution to the overall response (10%), compared to the flexors (90%). The sensitivities were similar for all head kinematics.

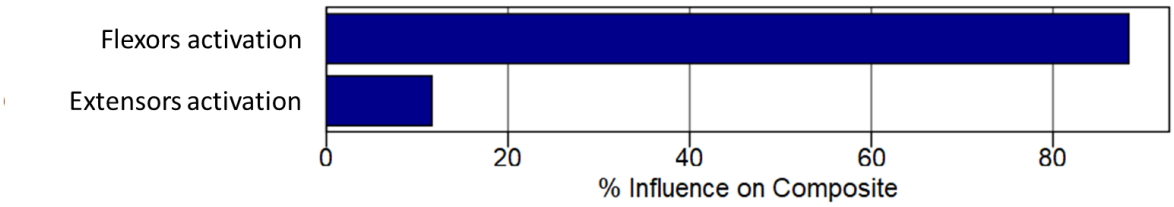

Figure 4-25: Influence of each optimization parameter in the Y-rotational displacement for the 3g rear impact simulation.

4.3.4 Optimized Rear Impact Parameters

The final optimization study was undertaken for each of the two rear impact severities to identify the specific flexor activation resulting in the highest correlation with the corresponding experimental result (Table 4-6).

Table 4-6: Optimized extensor muscle activation level for the two rear impact cases (activation onset times at 74 ms).

Impact severity (g)	Extensors activation scaling	Flexors activation scaling
3	0.00	1.00
4	0.00	1.00

For the constraints applied to the rear impact scenario, the OMA maximized the flexors activation at 100% and minimized the extensors activation (0%), which generated maximum resistance of the head to the movement rearwards in the rear impact. The OMA scheme improved the predicted displacement responses of the head as expected but did not provide the best global response since it was not optimized for acceleration. This outcome indicates the importance of making rotational acceleration from experiments available for use in the optimizations.

4.3.5 Correlation of Rear Impact Kinematics with Experimental Data

The correlation of the head center of mass kinematics with the rear impact experimental data for the OMA scheme was similar to all the other schemes for all severities simulated. The MMA scheme for the 3g impact demonstrated a lower correlation due to the activation of the extensors.

The correlation analysis of the head kinematic response to the experimental data indicated an improvement of 7% of the CMA relative to the MMA scheme (from 0.699 to 0.743, on average) (Figure 4-26). The OMA schemes provided an overall improvement of 4% in correlation to the MMA scheme (0.699 to 0.721, on average), resulting in a rating of fair biofidelity according to ISO/TR9790). The maximum individual improvement was 18% for the NMA compared to the MMA in the 3g impact case.

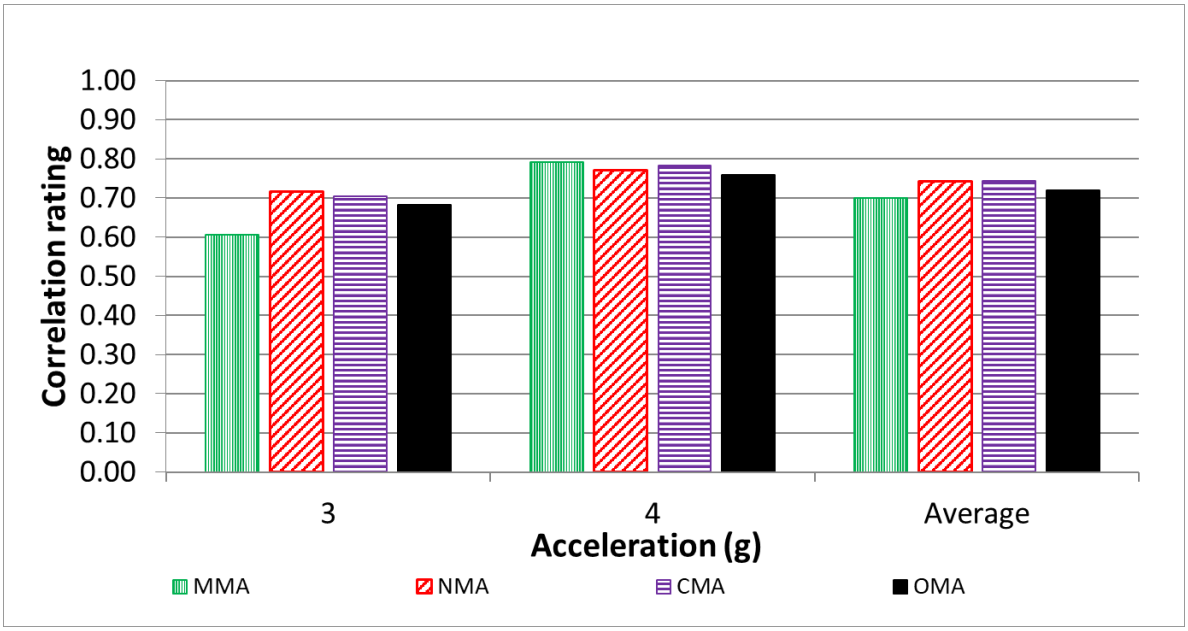

Figure 4-26: Correlation of muscle activation strategies to the experimental data for rear impacts ranging from 3g to 4g.

The NMA (muscles not activated) strategy presented the best correlation to the experimental data similar to the lower severities in frontal and lateral impacts. Due to the limited amount of impact

severities available from the literature for the rear impact scenario it was not possible to identify if this trend would be applicable at higher severity impacts.

Chapter 5: Discussion

5.1 Muscle Activation in Frontal Impact Scenarios

Rising interest to develop active safety systems in the automotive industry has increased the need for improved understanding of the physiological response of the human body under a range of impact scenarios, from low severity sudden stops in autonomous braking to high severity frontal impacts. The current study investigated muscle activation levels for a FE head-and-neck model in a contemporary HBM using human volunteer test data over a range of frontal impact severities. Moreover, this was the first study to optimize muscle activation levels and onset times for a broad range of frontal impact severities.

The optimization method for the muscle activation presented in this study for frontal impact improved the correlation of the kinematic response of the model with the experimental data for all severities. The OMA strategy increased the correlation (0.755), across all impact severities examined on average, by 35% relative to the MMA strategy (0.561), increasing the correlation from fair to good biofidelity according to ISO/TR9790. The maximum improvement in correlation was 103% for the optimized 3g impact case. The early onset times of the optimized responses relative to the MMA may be attributed to muscle tonus prior to impact in the human volunteer experiments that were not present in the current GHBMC neck model.

The extensors were activated earlier than the flexors for the OMA, which is in agreement with the literature (Foust et al., 1973). However, it could be argued that the time between onset and the peak activation was simplified, with the same time used for all muscle groups. Measurements from rear sled impacts with human volunteers (Magnusson et al., 1998) indicated that the muscle activation curves may differ for different muscles, and this may affect the optimum activation times. However, the low sensitivity of the head kinematics to flexor activation during the impacts suggests that this

simplification was reasonable for the present study. The lower sensitivity of the head kinematics for medium and high severity frontal impacts is explained by the lower force produced by the flexors in relation to the extensors, and the fact they are inserted in regions of the neck with a low or negative contribution to resisting to forward motion of the head. The force produced by the muscles is proportional to their volume, where the flexors represent 22% and the extensors 78% of the total muscle volume in the neck, which results in the much higher sensitivity of the head kinematics to the extensors.

Considering experimental data from low severity (1g) impact experiments (Hedenstierna et al., 2009), the maximum voluntary contraction of the trapezius in low severity experiments was 10%. This activation level was similar to the OMA for the extensors in the 2g and 3g impacts. The fixed activation of the flexors of 100% in the present model (MMA and CMA) was much higher than the 40% normalized electromyography level presented in the literature (Hedenstierna et al., 2009), but the flexor muscles did not strongly affect the head kinematics for the higher severity impacts (>3g). For these lower severities impacts, the NMA scheme presented a similar correlation to the optimized case, which may indicate that other soft tissues (adipose tissue and skin) present in the model are too stiff and produce increased resistance to the forward movement of the head, effectively decreasing the required activation levels. Future research will continue to investigate the effect of skin and adipose tissue on low severity impact response.

Another low severity frontal impact (1.4g) study with volunteers presented a peak normalized EMG of 78%, and an average of 20% for the extensors and a peak normalized EMG of 28% and an average of 5% for the flexors (Kumar et al., 2003). The study results differed from the present work as well as other published human volunteer tests (Hedenstierna et al., 2009). The differences in the Kumar study could be attributed to non-unique muscle activation schemes for frontal impacts as well as the surface electrode methodology used, which may differ from indwelling electrodes.

The extensor activation level (10%) for 2g and 3g impacts of the simulated OMA was similar to the activation levels reported for the trapezius (0 to 8.5% activation) in the optimization of the muscles for a co-activation isometric contraction of the head (Mortensen et al., 2018). Also, in the same study, the activation ratio between flexors and extensors were similar to the OMA for lower impact severities. However, the model used in the study by Mortensen was simplified and generated lower moments in flexion compared to experimental data. A study on diverse activation schemes for computational models (Dibb et al., 2013) optimized 21 neck muscles to an isometric contraction using different strategies and was higher than the activation magnitude of the flexors. The muscle activation schemes may also be non-unique, requiring more detailed experimental data of different muscles in impact situations. The resulting head kinematics presented similar values to the experimental sled tests. The discrepancies in activation magnitudes between the studies may be related to the different optimization methodologies, model complexities, and level of discretization of the muscle groups. The model was also run with the NMA scheme resulting in an overall correlation of 0.651. Although this correlation was higher than the MMA, some muscle activation is always present in a living person; therefore, this was not considered an improved overall activation strategy for the model.

Considering the hard tissues in the neck model, the C6 and C7 maximum strain levels predicted for the NMA and CMA cases exceeded the critical strain threshold for trabecular (9.5%) and cortical bone (1.78%) of the vertebrae, which results in erosion of affected elements, indicating the potential for tissue failure for the higher severity cases (>12g) (Figure 5-1). Partial failure was also predicted in the interspinous ligaments from C4 to C7 in the higher severity cases but could be associated with the T1 boundary conditions. Considering the NBDL human volunteer tests, injuries were not reported.

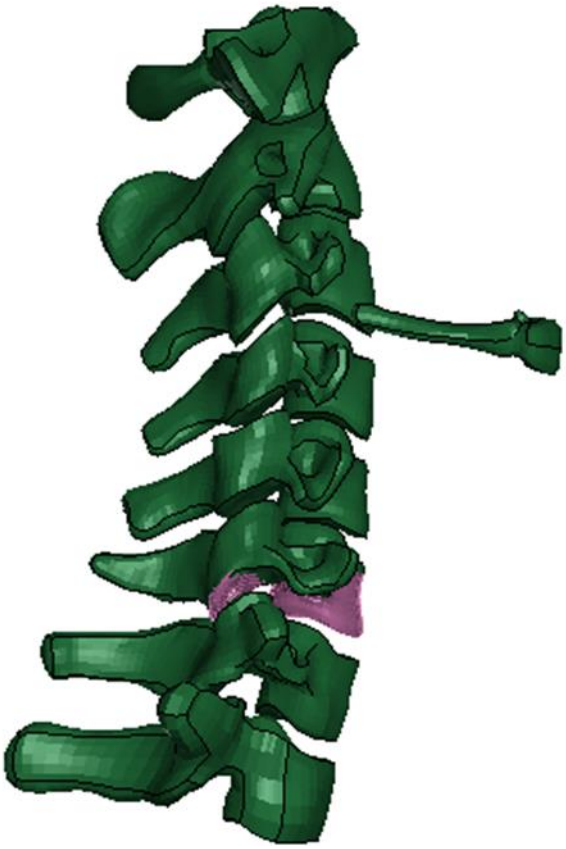

Figure 5-1: Predicted trabecular bone failure (purple) in C6 for the 15g frontal impact.

The OMA schemes were, on average, just 6% better correlated to the kinematic data than the CMA (Figure 5-2), which may indicate that two mechanisms are acting in the neck during the crash: (1) an almost constant response (CMA) with higher contribution to the kinematics and (2) an activation related to the magnitude of the head acceleration with a lower contribution to the kinematics. These inferences are in agreement with the literature (Happee et al., 2017), which shows that there are two main mechanisms related to neck stabilization, the vestibulocollic and cervicocollic reflex. However, the contribution of these two mechanisms is almost the same in that study, which could be attributed to the slower accelerations compared to the ones from the impacts that were used. The optimized scheme

could help guide future research on activation strategies for frontal impact scenarios while providing an improved kinematic response for the current model.

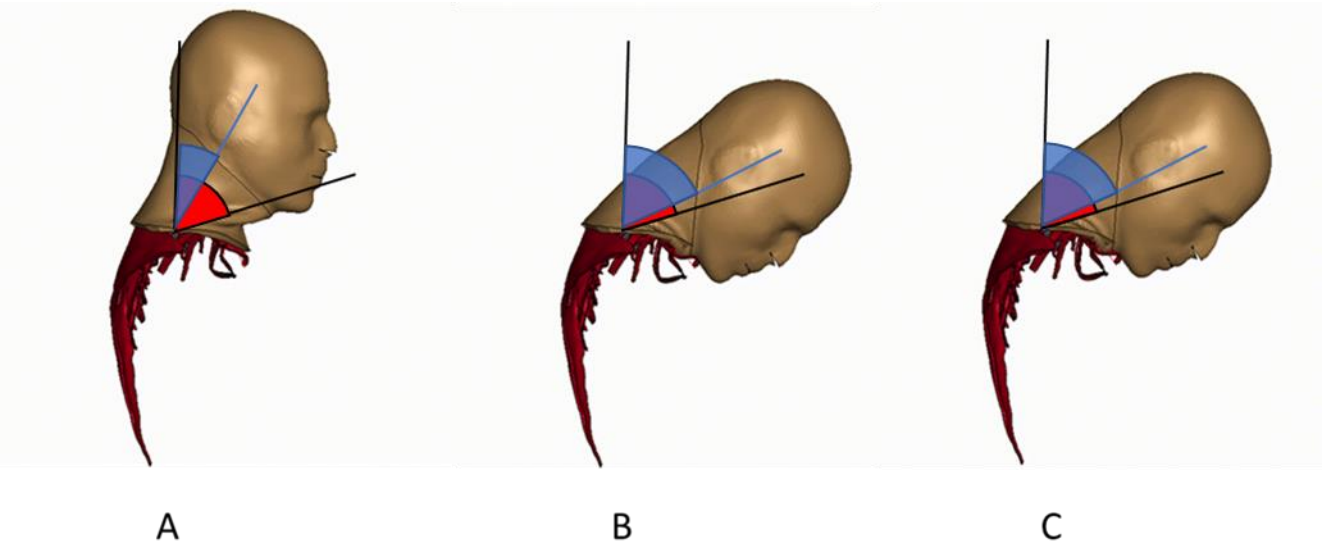

Figure 5-2: Maximum flexion of the model during the 8g front impact (blue line) for MMA (A), CMA (B) and OMA (C). The average maximum head rotation of the 8g sled test is presented as black lines.

Another contribution of this study is the deeper comprehension of the parameters affecting the impact response and how they should be handled during the development of closed-loop or open-loop motor control for muscle activation. For example, the results indicate that the flexors have little effect on the neck kinematic response in high severity frontal impacts, which was expected as this muscle group cannot generate forces counteracting the forward motion of the head.

The improved overall correlation rating with the experimental data of the CMA scheme agrees with the initial hypothesis that a single activation scheme, during frontal impacts, could be used to obtain a head kinematic response with a good correlation to the experimental data.

5.2 Muscle Activation in Lateral Impact Scenarios

The optimization method presented in this study for the OMA muscle activation in lateral impact improved the correlation of the kinematic response of the model (0.809) with the experimental data by 27% on average for all impact severities, relative to the original MMA strategy (0.644). This improvement resulted in the model response improving from fair to good biofidelity according to ISO/TR9790 ratings. The maximum improvement was 46% for the optimized 4g lateral impact case. As the impact severity increased, the optimized OMA onset times decreased for the extensors and right flexors and increased for the left flexors. The early onset time of the extensors was observed in volunteer rear impact tests (Foust et al., 1973) and, for low severity lateral left impacts, the muscles in the same (left) side of the impact had their activation onset times reduced, while the contralateral muscles had their activation increased with increasing impact severity (Kumar et al., 2004b). However, another right-side impact test by the same authors presented a decrease of all muscle onset times with increasing impact severity (Kumar et al., 2004a). From this data, the optimized right extensors and flexors agreed with the literature for the right-side impact case investigated, but further analysis is still required to verify if the left extensors and flexors are in agreement with the experimental results.

When no muscle was activated, the head moved in the antero-right direction was as observed in the experiments. For the OMA activation scenario, the resulting head kinematics were the most sensitive to the left extensors parameters for the OMA as this is the antagonist muscle group to the movement (Figure 5-3). The head kinematics had a low sensitivity to the flexor muscle activation, similar to what was observed in the frontal impact, attributed to the lower force generated by these muscle groups. The sensitivity of the kinematics for the right extensors, even with their higher volume and stronger force, was low, indicating that the parameters of the muscle groups that are not relevant antagonists to the movement in high severity impacts did not significantly affect the head displacement in the model regardless of their size.

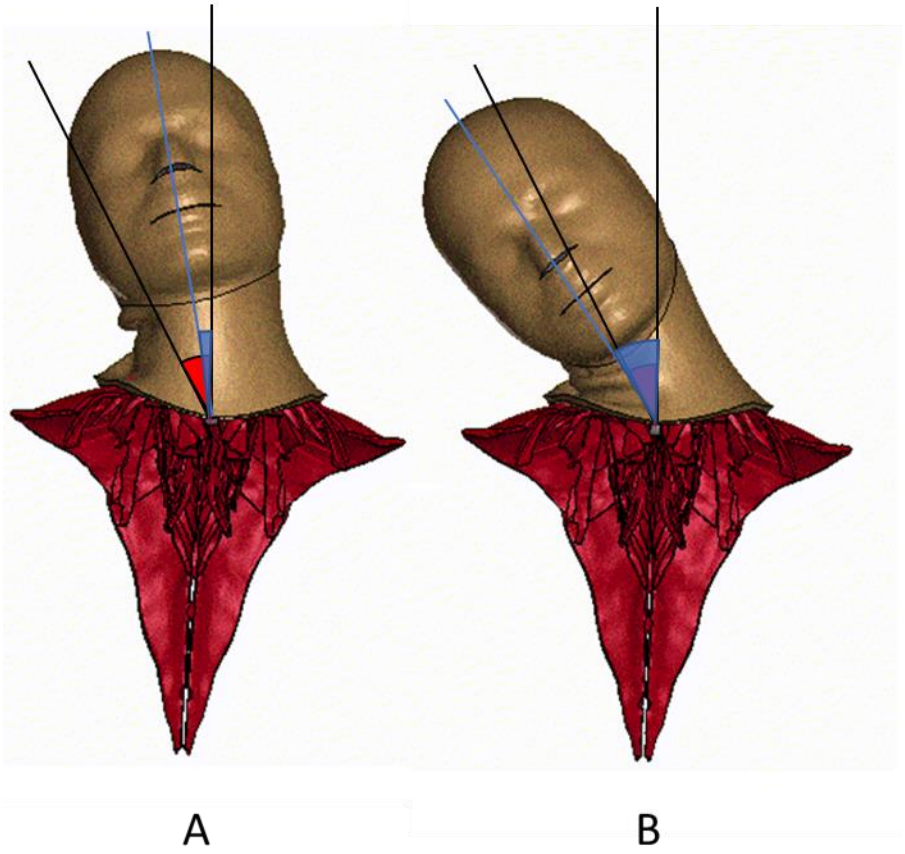

Figure 5-3: Head position after 250 ms in the 7g lateral right side-impact (head X-rotational displacement of the model in blue) for the MMA (A) and the OMA (B). The average head X-rotational displacement of the 7g sled test after 250 ms is presented as black lines.

Considering experimental data from low severity (1g) impact experiments (Hedenstierna et al., 2009), the measured activation using electromyography was 25% of the maximum voluntary contraction in the trapezius (Hedenstierna et al., 2009). Similarly, the CMA included a 20% activation for the extensors. The flexors activation for the CMA parameters was 100%, which was higher than the 84% normalized electromyography level presented in the literature (Hedenstierna et al., 2009), but indicates that the assumption of a Cocontraction mechanism with higher activated flexors is plausible. As suggested for the frontal impact scenarios, the difference in magnitude between the CMA and OMA

activate schemes may be, in part, due to the stiffness of the passive muscle, skin and adipose tissue in the computational model. These tissues have been reported to be overly stiff at low deformation rates.

Another low severity (1.3g) lateral impact study with volunteers presented a peak normalized EMG of 59% and an average of 20% for the extensors, and a peak normalized EMG of 61% and an average of 5% for the flexors (Kumar et al., 2004b). The OMA activation in this study was in agreement with the average activation of the flexors presented in the experimental study. The OMA left flexors in the simulations, as well as the average extensors activation, were similar to the study by Kumar et al. (Kumar et al., 2004b), but differed from Hedenstierna et al. (Hedenstierna et al., 2009) work and the simulated OMA right flexors. The differences in the Kumar et al. study could be attributed to non-unique muscle activation schemes for lateral impacts as well as the surface electrode methodology, which may differ from results reported for indwelling electrodes.

The increased complexity of the lateral impact kinematics and muscle activation, relative to the frontal impact scenarios, makes it challenging to assert that a simple CMA ratio between flexors and extensors represents the real response of the muscles during lateral impact. Notwithstanding, the CMA strategy presented good correlations with the experiments suggesting that this constant ratio may be intrinsic to the head-neck reflex mechanism.

The model was also run with the NMA scheme resulting in an overall correlation of 0.776. The NMA correlation was higher than the MMA and similar to the CMA correlation of 0.753, indicating that the ratio between extensors and flexors may be more relevant to the head global kinematics than the specific activation magnitude of the muscles.

Considering the hard tissues in the neck model, the odontoid process and C6 maximum strain levels for the trabecular and cortical bone of the vertebra exceeded the threshold values for the GHBMC model in the 7g lateral impact when using the NMA and CMA muscle activation strategies. These high strains indicated the potential for hard tissue failure for the highest severity case (7g). In addition, failure

was also predicted to occur in the capsular ligaments at C6-C7 for the 7g lateral impact. Hard tissue failures or ligament damage were not reported in the NBDL volunteer tests. However, the bone failure for the MMA affected a larger area and also included C3 and C4 when compared to the CMA, indicating the improvement in the biofidelity of lower muscle activation in the CMA strategy. In general, the predicted bone failures were localized within the model and did not suggest the presence of large scale traumatic fracture of the hard tissues.

Figure 5-4: Predicted odontoid process and C6 trabecular bone failure (purple) in the 7g lateral impact.

The OMA schemes were, on average, just 7.9% better correlated to the kinematic data than the CMA, which is similar to what was found for frontal activation and may indicate that two mechanisms are acting in the neck during the crash: the CMA and an activation related to the magnitude of the head

acceleration. Again, these inferences are in agreement with the literature (Happee et al., 2017), which shows that there are two main mechanisms related to neck stabilization, the vestibulocollic and cervicocollic reflex. The optimized scheme could help guide future research on activation strategies for lateral impact scenarios while providing an improved kinematic response for the current model.

The improved overall correlation rating of the CMA strategy with the experimental data agrees with the initial hypothesis that a single activation scheme, during lateral impacts, could be used to obtain a head kinematic response with a good correlation to the experimental data.

5.3 Muscle Activation in Rear Impact Scenarios

The optimization method presented in this study for the OMA muscle activation in rear impact improved the correlation of the kinematic response of the model (0.721) with the experimental data on average by 4% on average, relative to the MMA strategy (0.699). Both strategies were rated as good in terms of biofidelity according to ISO/TR9790. The maximum improvement was 17% for the optimized 3g impact case relative to the MMA. For the rear impact, the optimization did not generate the best-correlated kinematics, and this was attributed to the simplifications applied in the optimization strategy. In particular, the Y-rotational acceleration was not used in the optimization as it was not recorded during the volunteer experiments and deriving it from the displacement would generate not reliable data due to the large error propagation. The importance of Y-rotational acceleration suggests the importance of using the acceleration curves along with the displacements for muscle activation scheme optimization. In addition, the onset times were not optimized in the rear impact since the head kinematics presented low sensitivity to that parameter.

The lower sensitivity of the head kinematics for the rear impacts to muscle activity may be explained by the lower force produced by the flexor muscle group, which did not contribute to the head kinematics. The force produced by the muscles is proportional to their PCSA, which resulted in the

much higher sensitivity of the head kinematics to the extensors even though they are not antagonists to the movement in the rear impact.

Considering experimental data from low severity (1g) impact experiments (Hedenstierna et al., 2009), the measured activation using electromyography was 6% of the maximum voluntary contraction in the trapezius muscles. This result supports the low activation identified for the OMA, and the good correspondence with the NMA strategies. The flexors activation was 100% in the OMA and CMA, while the literature study reported 40% of the maximum voluntary contraction from the normalized electromyography data (Hedenstierna et al., 2009).

Another low severity (1.4g) frontal impact study with volunteers presented a peak normalized EMG of 33% and an average of 10% for the trapezius, and a peak normalized EMG of 113% and an average of 18% for the flexors (Kumar et al., 2002). The OMA activation in this study and values presented in other studies (Hedenstierna et al., 2009) differed from those presented by Kumar et al. In general, there were noticeable differences between activation of the flexors and extensors reported in the literature as well as compared to the OMA strategy, suggesting further research is needed in this area. The MMA presented a lower correlation to the experiments, compared to the other strategies, for the 3g rear impact but presented a similar correlation for the 4g rear impact (Figure 5-5). This result suggests that, as the impact severity increases from 3 to 4g, the sensitivity of the response to extensors activation is reduced and may extend to higher accelerations. As only two accelerations were available for the rear impact, further studies are necessary to support this inference.

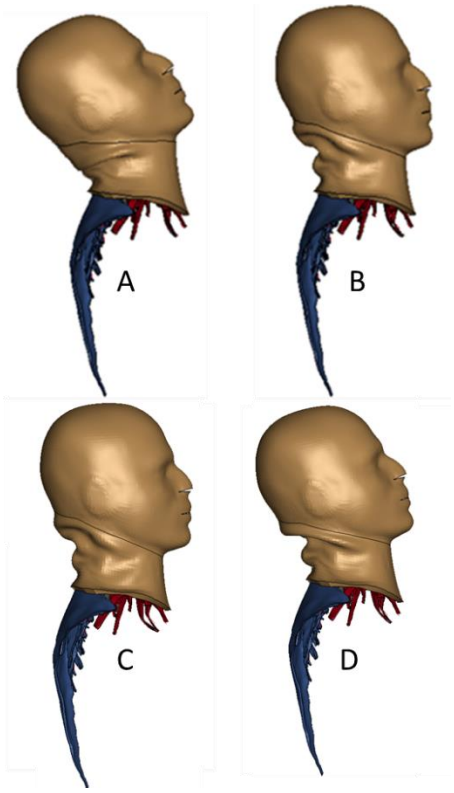

Figure 5-5: Maximum angular displacement of the head for the MMA 3g rear impact (A), OMA 3g rear impact (B), MMA 4g rear impact (C), and OMA 4g rear impact (D).

The model was also run with the NMA scheme resulting in an overall correlation of 0.744 with the experimental data. Although this correlation was similar to the other schemes, some muscle activation is always expected in a living person; therefore, it was hypothesized that the NMA does not represent the muscle activation levels present in the volunteers. This was also supported by experimental studies where EMG measurements were reported for the muscles in the neck.

Considering the hard tissues in the neck model, in contrast to the frontal and lateral impacts, the strain levels of the trabecular and cortical bone of the vertebrae did not reach threshold values and therefore no hard tissue fracture was predicted. In addition, no failure was predicted for the ligaments during the rear impacts. These results indicating no hard or soft tissue failure were in accordance with the volunteer tests.

The OMA schemes, on average and for each impact severity, presented the similar correlation values to the NMA and CMA schemes. Although this result indicates that the CMA can be used in the rear impacts to obtain improved global head kinematics similarly to the frontal and lateral cases, it does not clarify if the same two reflex mechanisms proposed for frontal and lateral are applicable to muscle activation in rear impacts. One limitation of the rear impact simulations was the small number of impact severities investigated. The similar correlation between activation schemes could indicate that the muscles resisting the movement, mainly the flexors, did not produce enough force to alter head kinematics. Again, this result points to the importance of the difference in muscle volume between flexor and extensor muscles, and therefore the force generated during impacts.

Another contribution of this study is the evidence that rear impacts may not be ideal for the development and validation of motor control for muscle activation schemes due to the low sensitivity of the global head kinematics to the variations of magnitude of muscle activation.

The improved overall correlation rating with the experimental data of the CMA scheme agrees with the initial hypothesis that a single activation scheme, during rear impacts, could be used to obtain a head kinematic response with a good correlation to the experimental data.

5.4 Cocontraction or Startle Muscle Activation Scheme

The startle reflex, as experimental data have shown, is evoked by significant and unexpected tactile, acoustic, or vestibular stimuli (Yeomans et al., 2002). The reflex initiated after an acoustic stimulus generated evidence that the startle mechanism could be the result of a combination of an initial generalized neck muscle activation and an alternative later activation mechanism (Siegmund et al., 2001b). The proposed CMA scheme, representing the startle reflex, and corresponding head kinematics presented a good correlation to all severities in frontal, lateral and rear impacts, reinforcing the hypothesis that a generalized muscle activation from the startle reflex is present during unanticipated

impacts. Also, the OMA scheme kinematics presented only a slightly higher correlation to the experimental data than the CMA, indicating that the CMA captures a large aspect of the active muscle response. Also, the increasing extensors activation of the OMA when the impact severity increases could be attributed to the alternative later activation mechanism observed by Siegmund et al., 2001b.

The startle activation is not the only possible mechanism related to the head-neck reflex in impacts. The vestibulocollic and cerviculocollic reflex could also explain the two different mechanisms presented in simulated muscle activation, as described in Section 5.2. As the NBDL data does not contain information on successive sled impacts with the same subjects and the impacts were not expected by the volunteers, a further distinction between the startle and the other reflexes is not possible. Further studies are necessary to correlate the constant CMA to one specific mechanism.

5.5 Study Limitations

Future studies should consider the potential impact due to subject variability as the current study only optimized muscle activation to the average subject response. Another limitation of this study was that the muscles were divided into only two groups, and each group had all the bulk elements activated in the same manner. This was an oversimplification of the problem; muscles in the same group do not necessarily activate similarly, and muscles may not act exclusively in one group during neck movements. However, as the improved correlation score shows, the hypothesis that the response of the muscle groups is dominated by the strongest muscles (sternocleidomastoid and trapezius) is reasonable for global kinematic studies.

Another possibility of improvement in the muscle activation strategy may include investigation of the local intervertebral joints Y-rotation. During the rear impact simulations, the characteristic S-shape curvature of the neck observed in whiplash injury was not reproduced by the model. As expected, this is an indication that to obtain accurate localized stresses and strains in the neck tissues, an analysis

that observes individual vertebrae kinematics is necessary, in addition to the head kinematics. However, due to the scarcity of EMG data for higher impact severities and challenges in defining the magnitude of the muscle activation using currently available techniques, indirect methods, such as the one presented in this work, could guide future development of HBM to obtain reasonable global kinematics and help elucidate the muscle reflex mechanisms acting in impact situations.

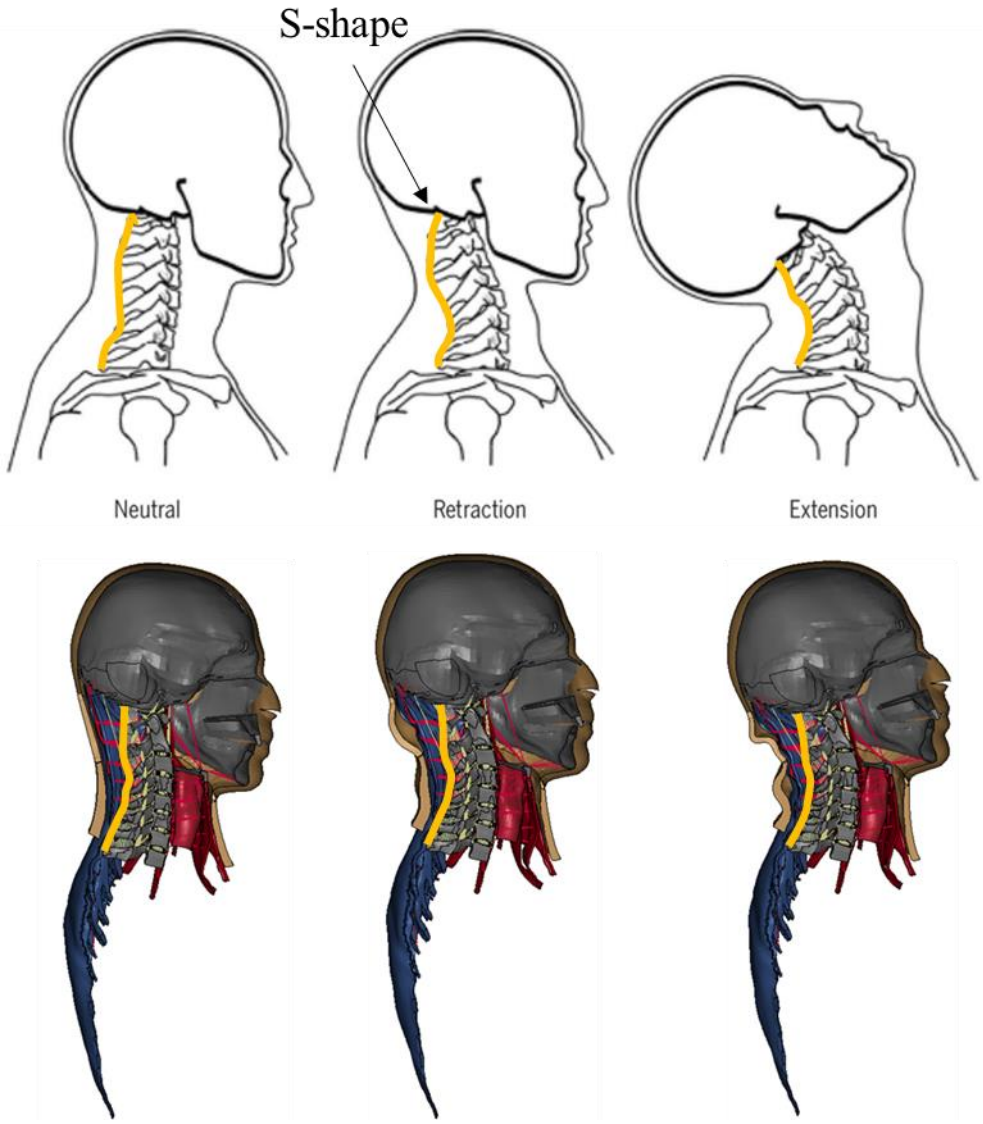

Figure 5-6: Idealized curvature of the spine during a rear impact (top) and simulated result for the CMA 4g rear impact (bottom). (Adapted from (Stemper and Corner, 2016))

The S-shape curvature of the spine was not observed in the GHBMC model during rear impacts and was attributed to a reduction in shear between the vertebrae. This was possibly related to the relatively high stiffness of the skin and adipose tissue used in the model compared to that of human tissues. The effect of material properties of these soft tissues in relation to muscle activation is the object of future work.

It is important to note that different optimization methodologies could arrive at different muscle activations. As the optimization presented in this work was simplified to a linear problem, the objectives converged in all cases, but this may not be the case if other more sensitive methods were applied.

5.6 Significance and Impact of the Study

HBMs provide an opportunity to predict the potential for injury risk and vehicle occupant response in impact events (Barker et al., 2017). Muscle contraction may be important for predicting injury risk and pre-crash intervention kinematic response, for example, during autonomous braking (Ólafsdóttir et al., 2013; Östh et al., 2015).

This study was the first to optimize muscle activation schemes of the neck to a wide range of frontal, lateral and rear impacts confirming a hypothesis that a unique scheme was capable of generating head kinematics with a good correlation with the experimental data to all impacts. This unique CMA scheme was used to improve the GHBMC M-50 model head kinematic response. Further, the methodology presented in this thesis could be used as a guideline to improve muscle activation schemes in other HBM. The open-loop activation schemes and analysis established could be used as a frame of reference in the future development of closed-loop controls for the cervical muscles in impact scenarios and could be used to help identify the mechanism acting in crash scenarios.

Chapter 6: Conclusions

The current study investigated neck muscle activation levels for human volunteer tests over a range of frontal, lateral and rear impact severities using a detailed FE head-and-neck model from a contemporary HBM. This was the first study to optimize muscle activation levels and onset times for a broad range of impact severities and directions.

The findings of this study provide new insight into the role of muscle activation on the frontal, lateral and rear impact kinematic response of the head and neck. The individual OMA schemes provided an optimized trajectory-based activation scheme for the GHBMC M50 HBM; however, this scheme is dependent on the impact severity and impact direction. These results could be used to further elucidate the influence of muscle activation and onset time of the flexors and extensors in head kinematics for other impact scenarios. In contrast, the single cocontraction muscle activation strategy presented a good correlation with all frontal, lateral and rear impact tests confirming the initial hypothesis that a single unique activation scheme could be used to achieve good correlated global head kinematics with the experimental data. It is important to note that the rear impacts were less sensitive to the muscle activation schemes compared to frontal and lateral impacts. This lower sensitivity in rear impact could be attributed to the weaker flexors, which were antagonistic to the head movement.

A more focused analysis is necessary to define if the constant muscle activation component is related to the startle reflex or the vestibulocollic and cervicocollic reflexes. The head kinematics during the impacts were more sensitive to the activation magnitude of the extensors than the one of the flexors, even in the rear impact, in which that muscle group did not act antagonistically to the movement. This result indicated that the strength difference between the two muscle groups is potentially quite large; the extensors could exhibit a much lower activation level than the flexors to stabilize the neck for example.

In conclusion, new schemes and understanding of neck musculature activation during impact developed in this thesis could be used as a foundation to improve muscle activation schemes to better predict injury risk using contemporary HBM. Future work should continue to improve effective generalization of the muscle activation schemes through the development of closed-loop controls for activation of the neck musculature during impact.

Bibliography

Albert, D.L., Beeman, S.M., Kemper, A.R., 2018. Evaluation of Hybrid III and THOR-M neck kinetics and injury risk under various restraint conditions during full-scale frontal sled tests. Traffic Inj. Prev. 19, S40–S47. https://doi.org/10.1080/15389588.2018.1524141

Albert, M., McCaig, L.F., 2015. Emergency department visits for motor vehicle traffic injuries: United States, 2010-2011. NCHS Data Brief 1–8.

Alizadeh, M., Knapik, G.G., Mageswaran, P., Mendel, E., Bourekas, E., Marras, W.S., 2020. Biomechanical musculoskeletal models of the cervical spine: A systematic literature review. Clin. Biomech. 71, 115–124. https://doi.org/10.1016/j.clinbiomech.2019.10.027

Amell, T., 2002. Electromyography of superficial cervical muscles with exertion in the sagittal , coronal and oblique planes 27–37. https://doi.org/10.1007/s005860100318

Anderson, J., Li, Z., Goubel, F., 2002. Models of skeletal muscle to explain the increase in passive stiffness in desmin knockout muscle. J. Biomech. 35, 1315–1324. https://doi.org/10.1016/S0021-9290(02)00170-7

Arbogast, K.B., Balasubramanian, S., Seacrist, T., Maltese, M.R., García-España, J.F., Hopely, T., Constans, E., Lopez-Valdes, F.J., Kent, R.W., Tanji, H., Higuchi, K., 2009. Comparison of kinematic responses of the head and spine for children and adults in low-speed frontal sled tests. Stapp Car Crash J. 53, 329–72. https://doi.org/10.1093/brain/awg034

Barker, J.B., Cronin, D.S., Chandrashekar, N., 2014. High Rotation Rate Behavior of Cervical Spine Segments in Flexion and Extension. J. Biomech. Eng. 136, 1–10. https://doi.org/10.1115/1.4028107

Barker, J.B., Cronin, D.S., Nightingale, R.W., 2017. Lower Cervical Spine Motion Segment

Computational Model Validation: Kinematic and Kinetic Response for Quasi-Static and Dynamic Loading. J. Biomech. Eng. 139, 061009. https://doi.org/10.1115/1.4036464

Bensamoun, S., Stevens, L., Fleury, M.J., Bellon, G., Goubel, F., Ho Ba Tho, M.C., 2006. Macroscopic-microscopic characterization of the passive mechanical properties in rat soleus muscle. J. Biomech. 39, 568–578. https://doi.org/10.1016/j.jbiomech.2004.04.036

Betts, J.G., Young, K.A., Wise, J.A., Johnson, E., Poe, B., Kruse, D.H., Korol, O., Johnson, J.E., Womble, M., DeSaix, P., 2013. Anatomy and Physiology. Houston.

Blouin, J.S., Descarreaux, M., Bélanger-Gravel, A., Simoneau, M., Teasdale, N., 2003. Attenuation of human neck muscle activity following repeated imposed trunk-forward linear acceleration. Exp. Brain Res. 150, 458–464. https://doi.org/10.1007/s00221-003-1466-9

Brolin, K., Halldin, P., Leijonhufvud, I., 2005. The effect of muscle activation on neck response. Traffic Inj. Prev. 6, 67–76. https://doi.org/10.1080/15389580590903203

Carlsson, A., GP, S., Linder, A., Svensson, M., 2010. Motion of the head and neck of female and male volunteers in rear impact car-to-car tests at 4 and 8 km/h. IRCOBI Conf. Hanover, Ger. Sept. 2010 29–40.

Correia, M.A., McLachlin, S.D., Cronin, D.S., 2020. Optimization of muscle activation schemes in a finite element neck model simulating volunteer frontal impact scenarios. J. Biomech. https://doi.org/10.1016/j.jbiomech.2020.109754

Cowin, S.C., 2001. Bone Mechanics Handbook. CRC Press, Boca Raton. https://doi.org/10.1201/b14263

De Luca, C.J., Donald Gilmore, L., Kuznetsov, M., Roy, S.H., 2010. Filtering the surface EMG signal: Movement artifact and baseline noise contamination. J. Biomech. 43, 1573–1579.

https://doi.org/10.1016/j.jbiomech.2010.01.027

Dehner, C., Schick, S., Kraus, M., Scola, A., Hell, W., Kramer, M., 2013. Muscle Activity Influence on the Kinematics of the Cervical Spine in Frontal Tests. Traffic Inj. Prev. 14, 607–613. https://doi.org/10.1080/15389588.2012.734937

Deng, B., Begeman, P.C., Yang, K.H., Tashman, S., King, A.I., 2000. Kinematics of Human Cadaver Cervical Spine During Low Speed Rear-end Impacts.

Dibb, A.T., Cox, C.A., Nightingale, R.W., Luck, J.F., Cutcliffe, H.C., Myers, B.S., Arbogast, K.B., Seacrist, T., Bass, C.R., 2013. Importance of Muscle Activations for Biofidelic Pediatric Neck Response in Computational Models. Traffic Inj. Prev. 14. https://doi.org/10.1080/15389588.2013.806795

Ejima, S., Ono, K., Kaneoka, K., Fukushima, M., 2005. Development and Validation of the Human Neck Muscle Model Under Impact Loading. Ircobi 245–255.

Elemance, L., 2016. User Manual : M50 Detailed Occupant, Version 4.5 for LS-DYNA.

Ewing, C.L., Thomas, D.J., 1972. Human Head and Neck Response To Impact Acceleriation. DTIC Doc.

Fanta, O., Hadraba, D., Lopot, F., Kubový, P., Bouček, J., Jelen, K., 2013. Pre-activation and muscle activity during frontal impact in relation to whiplash associated disorders. Neuroendocrinol. Lett. 34, 708–716.

Fehrenbach, M., Herring, S., 2016. Illustrated Anatomy of the Head and Neck, 5th ed. Saunders.

Feller, L., Kleinback, C., Fehr, J., Schmitt, S., 2016. Incorporating Muscle Activation Dynamics into the Global Human Body Model. IRCOBI Conf. 512–523.

Fice, J.B., Cronin, D.S., Panzer, M.B., 2011. Cervical spine model to predict capsular ligament

response in rear impact. Ann. Biomed. Eng. 39, 2152–2162. https://doi.org/10.1007/s10439-011-0315-4

Fice, J.B., Siegmund, G.P., Blouin, J.S., 2018. Neck muscle biomechanics and neural control. J. Neurophysiol. 120, 361–371. https://doi.org/10.1152/jn.00512.2017

Foust, D.R., Chaffin, D.B., Snyder, R.G., Baum, J.K., 1973. Cervical range of motion and dynamic response and strength of cervical muscles. SAE Int. https://doi.org/10.4271/730975

Gasser, H.S., Hill, A.V., 1924. The dynamics of muscular contraction. Proc. R. Soc. London 96, 398–437.

Gille, U., 2007. Fiederung eines Muskels [WWW Document]. URL https://commons.wikimedia.org/wiki/File:Fiederung.svg

Gordon, A., Huxley, A., Julian, F., 1966. The variation in isometric tension with sarcomere. E.Guigon.Free.Fr 170–192.

Gray, H., 1918. Anatomy of the human body. Lea & Febiger, Philadelphia.

Happee, R., de Bruijn, E., Forbes, P.A., van der Helm, F.C.T., 2017. Dynamic head-neck stabilization and modulation with perturbation bandwidth investigated using a multisegment neuromuscular model. J. Biomech. 58, 203–211. https://doi.org/10.1016/j.jbiomech.2017.05.005

Hedenstierna, S., Halldin, P., Brolin, K., 2008. Evaluation of a combination of continuum and truss finite elements in a model of passive and active muscle tissue. Comput. Methods Biomech. Biomed. Engin. 11, 627–639. https://doi.org/10.1080/17474230802312516

Hedenstierna, S., Halldin, P., Siegmund, G.P., 2009. Neck Muscle Load Distribution in Lateral , Frontal , and Rear-End Impacts A Three-Dimensional Finite Element Analysis. Spine (Phila. Pa. 1976). 34, 2626–2633. https://doi.org/10.1097/BRS.0b013e3181b46bdd

Hellmuth, R., 2010. Hill muscle model [WWW Document]. URL https://commons.wikimedia.org/wiki/File:Hill_muscle_model.svg (accessed 8.27.19).

Hendriks, E.J.M., Scholten-Peeters, G.G.M., Van Der Windt, D.A.W.M., Neeleman-Van Der Steen, C.W.M., Oostendorp, R.A.B., Verhagen, A.P., 2005. Prognostic factors for poor recovery in acute whiplash patients. Pain 114, 408–416. https://doi.org/10.1016/j.pain.2005.01.006

Hernández, I.A., Fyfe, K.R., Heo, G., Major, P.W., 2006. The role of sternocleidomastoid muscle in simulated low velocity rear-end impacts. Eur. Spine J. 15, 876–885. https://doi.org/10.1007/s00586-005-0956-9

Ivancic, A., Pradhan, V., 2017. The influence of isometrically derived neck muscle spatial tuning patterns on head response in dynamic conditions.

Iwamoto, M., 2018. Modeling Passive and Active Muscles, Basic Finite Element Method as Applied to Injury Biomechanics. Elsevier Inc. https://doi.org/10.1016/B978-0-12-809831-8.00011-8

Iwamoto, M., Nakahira, Y., Kimpara, H., Sugiyama, T., Min, K., 2012. Development of a human body finite element model with multiple muscles and their controller for estimating occupant motions and impact responses in frontal crash situations. Stapp Car Crash J. 56, 231–68.

Joodaki, H., Panzer, M.B., 2018. Skin mechanical properties and modeling: A review. Proc. Inst. Mech. Eng. Part H J. Eng. Med. 232, 323–343. https://doi.org/10.1177/0954411918759801

Keaveny, T.M., Morgan, E.F., Niebur, G.L., Yeh, O.C., 2001. Biomechanics of Trabecular Bone. Annu. Rev. Biomed. Eng. 3, 307–333.

Khodaei, H., Mostofizadeh, S., Brolin, K., Johansson, H., Osth, J., 2013. Simulation of active skeletal muscle tissue with a transversely isotropic viscohyperelastic continuum material model. Proc. Inst. Mech. Eng. Part H J. Eng. Med. 227, 571–580. https://doi.org/10.1177/0954411913476640

Kumar, S., Ferrari, R., Narayan, Y., 2004a. Cervical muscle response to whiplash-type right anterolateral impacts. Eur. Spine J. 13, 398–407. https://doi.org/10.1007/s00586-004-0700-x

Kumar, S., Ferrari, R., Narayan, Y., 2004b. Electromyographic and Kinematic Exploration of Whiplash-Type Neck Perturbations in Left Lateral Collisions. Spine (Phila. Pa. 1976). 29, 650–659. https://doi.org/10.1097/01.BRS.0000115136.24824.DF

Kumar, S., Narayan, Y., Amell, T., 2003. Analysis of low velocity frontal impacts. Clin. Biomech. 18, 694–703. https://doi.org/10.1016/S0268-0033(03)00137-2

Kumar, S., Narayan, Y., Amell, T., 2002. An electromyographic study of low-velocity rear-end impacts. Spine (Phila. Pa. 1976). 27, 1044–1055. https://doi.org/10.1097/00007632-200205150-00009

Lasswell, T.L., Cronin, D.S., Medley, J.B., Rasoulinejad, P., 2017. Incorporating ligament laxity in a finite element model for the upper cervical spine. Spine J. 17, 1755–1764. https://doi.org/10.1016/j.spinee.2017.06.040

Lee, D., Glueck, M., Khan, A., Fiume, E., Jackson, K., 2011. Modeling and simulation of skeletal muscle for computer graphics: A survey, Foundations and Trends in Computer Graphics and Vision. https://doi.org/10.1561/0600000036

Lindahl, O., 1976. Mechanical properties of dried defatted spongy bone. Acta Orthop. 47, 11–19. https://doi.org/10.3109/17453677608998966

Livermore Software Technology Corporation, 2016. VOLUME II Material Models, LS-DYNA Keyword User's Manual Volume II Material Models.

Magnusson, M.L., Pope, M.H., Hasselquist, L., Bolte, K.M., Ross, M., Goel, V.K., Lee, J.S., Spratt, K.F., Clark, C.R., Wilder, D.G., 1998. Cervical electromyographic activity during low-speed

impact 118–125.

Mang, D.W.H., Siegmund, G.P., Brown, H.J., Goonetilleke, S.C., Blouin, J.S., 2015. Loud preimpact tones reduce the cervical multifidus muscle response during rear-end collisions: A potential method for reducing whiplash injuries. Spine J. 15, 153–161. https://doi.org/10.1016/j.spinee.2014.08.002

Martin, R.B., Burr, D.B., Sharkey, N.A., Fyhrie, D.P., 2015. Skeletal Tissue Mechanics. Springer New York, New York, NY. https://doi.org/10.1007/978-1-4939-3002-9

Mathews, E.A., Balasubramanian, S., Seacrist, T., Maltese, M.R., Sterner, R., Arbogast, K.B., 2013. Electromyography responses of pediatric and young adult volunteers in low-speed frontal impacts. J. Electromyogr. Kinesiol. 23, 1206–1214. https://doi.org/10.1016/j.jelekin.2013.06.010

Mattucci, S.F.E., Cronin, D.S., 2015. A method to characterize average cervical spine ligament response based on raw data sets for implementation into injury biomechanics models. J. Mech. Behav. Biomed. Mater. 41, 251–260. https://doi.org/10.1016/j.jmbbm.2014.09.023

Mattucci, S.F.E., Moulton, J.A., Chandrashekar, N., Cronin, D.S., 2012. Strain rate dependent properties of younger human cervical spine ligaments. J. Mech. Behav. Biomed. Mater. 10, 216–226. https://doi.org/10.1016/j.jmbbm.2012.02.004

McElhaney, J.H., 1966. Dynamic response of bone and muscle tissue. J. Appl. Physiol. 21, 1231–1236. https://doi.org/10.1152/jappl.1966.21.4.1231

Meyer, G.A., McCulloch, A.D., Lieber, R.L., 2011. A nonlinear model of passive muscle viscosity. J. Biomech. Eng. 133, 1–9. https://doi.org/10.1115/1.4004993

Morimoto, K., Sakamoto, M., Fukuhara, T., Kato, K., 2013. Electromyographic Study of Neck

Muscle Activity According to Head Position in Rugby Tackles. J. Phys. Ther. Sci. 25, 563–566. https://doi.org/10.1589/jpts.25.563

Mortensen, J., Trkov, M., Merryweather, A., 2018. Exploring novel objective functions for simulating muscle coactivation in the neck. J. Biomech. 71, 127–134. https://doi.org/10.1016/j.jbiomech.2018.01.030

Mukund, K., Subramaniam, S., 2020. Skeletal muscle: A review of molecular structure and function, in health and disease. Wiley Interdiscip. Rev. Syst. Biol. Med. 12, 1–46. https://doi.org/10.1002/wsbm.1462

Nalla, R.K., Kinney, J.H., Ritchie, R.O., 2003. Mechanistic fracture criteria for the failure of human cortical bone. Nat. Mater. 2, 164–168. https://doi.org/10.1038/nmat832

National Highway Traffic Safety Administration [WWW Document], 2012. . NBDL Hum. Volunt. sled tests without car body 1522 to 1651. URL https://www-nrd.nhtsa.dot.gov/database/VSR/bio/QueryTest.aspx

Ólafsdóttir, J.M., Östh, J.K.H., Davidsson, J., Brolin, K.B., 2013. Passenger Kinematics and Muscle Responses in Autonomous Braking Events with Standard and Reversible Pre-tensioned Restraints. Int. Res. Counc. Biomech. Inj. Conf. 46, 602–617.

Olszko, A. V, Beltran, C.M., Vasquez, K.B., McGhee, J.S., Chancey, V.C., Yoganandan, N., Pintar, F.A., Baisden, J.L., 2018. Initial analysis of archived non-human primate frontal and rear impact data from the biodynamics data resource. Traffic Inj. Prev. 19, S44–S49. https://doi.org/10.1080/15389588.2017.1390570

Ono, K., Kaneoka, K., Wittek, A., Kajzer, J., 1997. Cervical Injury Mechanism Based on the Analysis of Human Cervical Vertebral Motion and Head-Neck-Torso Kinematics During Low Speed

Rear Impacts. SAE Tech. Pap. Ser. 1, 339–356. https://doi.org/10.4271/973340

Östh, J., Davidsson, J., Pipkorn, B., Jakobsson, L., 2015. Muscle Activation Strategies in Human Body Models for the Development of Integrated Safety. ESV - 24th Int. Tech. Conf. Enhanc. Saf. Veh. 1–15.

Panzer, M.B., Fice, J.B., Cronin, D.S., 2011. Cervical spine response in frontal crash. Med. Eng. Phys. 33, 1147–1159. https://doi.org/10.1016/j.medengphy.2011.05.004

Pramudita, J.A., Ono, K., Ejima, S., Kaneoka, K., Shiina, I., Ujihashi, S., 2007. Head / Neck / Torso Behavior and Cervical Vertebral Motion of Human Volunteers During Low Speed Rear Impact : Mini-sled Tests with Mass Production Car Seat, in: 2007 International IRCOBI Conference on the Biomechanics of Injury. pp. 201–217.

Richfield, D., 2014. Medical gallery of David Richfield 2014. WikiJournal Med. 1, 9. https://doi.org/10.15347/wjm/2014.009

Robi, K., Jakob, N., Matevz, K., Matjaz, V., 2013. The Physiology of Sports Injuries and Repair Processes, in: Current Issues in Sports and Exercise Medicine. InTech, p. 13. https://doi.org/10.5772/54234

Sato, F., Nakajima, T., Ono, K., Svensson, M., Brolin, K., Kaneoka, K., 2014. Dynamic cervical vertebral motion of female and male volunteers and analysis of its interaction with head/neck/torso behavior during low-speed rear impact, in: 2014 IRCOBI Conference Proceedings - International Research Council on the Biomechanics of Injury.

Schmitt, K.U., Niederer, P.F., Cronin, D.S., Muser, M.H., Walz, F., 2014. Trauma biomechanics an introduction to injury biomechanics, Trauma Biomechanics: An Introduction to Injury Biomechanics. https://doi.org/10.1007/978-3-642-53920-6

Shen, D., Cronin, D.S., 2017. Effect of Active Musculature Parameters on Neck Response and Potential for Injury. IRCOBI Conf. Proceedings. 654–655.

Siegmund, G.P., Blouin, J.-S., Brault, J.R., Hedenstierna, S., Inglis, J.T., 2007. Electromyography of Superficial and Deep Neck Muscles During Isometric, Voluntary, and Reflex Contractions. J. Biomech. Eng. 129, 66. https://doi.org/10.1115/1.2401185

Siegmund, G.P., Blouin, J.S., Carpenter, M.G., Brault, J.R., Inglis, J.T., 2008. Are cervical multifidus muscles active during whiplash and startle? An initial experimental study. BMC Musculoskelet. Disord. 9, 1–9. https://doi.org/10.1186/1471-2474-9-80

Siegmund, G.P., Heinrichs, B.E., Lawrence, J.M., 2001a. SAE TECHNICAL Kinetic and Kinematic Responses of the RID2a , Hybrid III and Human Volunteers in Low-Speed Rear-End Collisions 45.

Siegmund, G.P., Sanderson, D.J., Inglis, T.J., 2002. The effect of perturbation acceleration and advance warning on the neck postural responses of seated subjects. Exp. Brain Res. 144, 314–321. https://doi.org/10.1007/s00221-002-1048-2

Siegmund, G.P., Sanderson, D.J., Myers, B.S., Inglis, J.T., 2003. Awareness affects the response of human subjects exposed to a single whiplash-like perturbation. Spine (Phila. Pa. 1976). 28, 671–679. https://doi.org/10.1097/00007632-200304010-00010

Siegmund, G.P., Timothy, I.J., Sanderson, D.J., 2001b. Startle response of human neck muscles sculpted by readiness to perform ballistic head movements. J. Physiol. 535, 289–300. https://doi.org/10.1111/j.1469-7793.2001.00289.x

Skeletal muscle [WWW Document], 2019. URL https://commons.wikimedia.org/wiki/File:Skeletal_muscle.jpg (accessed 9.25.19).

Snyder, R.G., Chaffin, D.B., Foust, D.R., 1975. Bioengineering study of basic physical measurements related to susceptibility to cervical hyperextension-hyperflexion injury Report No.

Stemper, B.D., Corner, B.D., 2016. Whiplash-Associated Disorders: Occupant Kinematics and Neck Morphology. J. Orthop. Sport. Phys. Ther. 46, 834–844. https://doi.org/10.2519/jospt.2016.6846

Sturzenegger, M., DiStefano, G., Radanov, B.P., Schnidrig, A., 2012. Presenting symptoms and signs after whiplash injury: The influence of accident mechanisms. Neurology 44, 688–688. https://doi.org/10.1212/wnl.44.4.688

Swartz, E.E., Floyd, R.T., Cendoma, M., 2005. Cervical spine functional anatomy and the biomechanics of injury due to compressive loading. J. Athl. Train. 40, 155–161.

Thunert, C., 2017. CORAplus Release 4.0.4 User ' s Manual.

Thunnissen, J., Wismans, J., Ewing, C.L., Thomas, D.J., 1995. Human Volunteer Head-Neck Response in Frontal Flexion: A New Analysis, in: SAE Technical Paper Series. San Diego, pp. 439–460. https://doi.org/10.4271/952721

Toursel, T., Stevens, L., Granzier, H., Mounier, Y., 2002. Passive tension of rat skeletal soleus muscle fibers: Effects of unloading conditions. J. Appl. Physiol. 92, 1465–1472. https://doi.org/10.1152/japplphysiol.00621.2001

van den Kroonenberg, A., Philippens, M., Cappon, H., Wismans, J., Hell, W., Langwieder, K., 2010. Human Head-Neck Response During Low-Speed Rear End Impacts, in: SAE Technical Paper Series. https://doi.org/10.4271/983158

Vasavada, A., Li, S., Delp, S., 1998. Influence of muscle morphology and moment arms on moment-geneating capacity of human neck muscles. Spine (Phila. Pa. 1976). 23, 412–422.

Vavalle, N.A., Jelen, B.C., Moreno, D.P., Stitzel, J.D., Gayzik, F.S., 2013. An Evaluation of

Objective Rating Methods for Full-Body Finite Element Model Comparison to PMHS Tests. Traffic Inj. Prev. 14. https://doi.org/10.1080/15389588.2013.802777

Walton, D.M., MacDermid, J.C., Giorgianni, A.A., Mascarenhas, J.C., West, S.C., Zammit, C.A., 2013. Risk Factors for Persistent Problems Following Acute Whiplash Injury: Update of a Systematic Review and Meta-analysis. J. Orthop. Sport. Phys. Ther. 43, 31–43. https://doi.org/10.2519/jospt.2013.4507

Winters, J.M., Stark, L., 1985. Analysis of Fundamental Human Movement Patterns Through the Use of In-Depth Antagonistic Muscle Models. IEEE Trans. Biomed. Eng. BME-32, 826–839. https://doi.org/10.1109/TBME.1985.325498

Wismans, J., van Oorschot, H., Woltring, H., 1986. Omni-Directional Human Head- Neck Response. SAE Trans. 95, 819–837.

Wittek, A., Ono, K., Kajzer, J., Örtengren, R., Inami, S., 2001. Analysis and comparison of reflex times and electromyograms of cervical muscles under impact loading using surface and fine-wire electrodes. IEEE Trans. Biomed. Eng. 48, 143–152. https://doi.org/10.1109/10.909635

Yang, K.H., Barker, J., Cronin, D.S., Gierczycka, D., Hu, J., Iwamoto, M., Jin, X., Kalra, A., Mao, H., Presley, B.R., Shen, D., Singh, D., Zhu, F., 2018. Basic Finite Element Method as Applied to Injury Biomechanics. Elsevier. https://doi.org/10.1016/C2015-0-06702-8

Yeomans, J.S., Li, L., Scott, B.W., Frankland, P.W., 2002. Tactile, acoustic and vestibular systems sum to elicit the startle reflex. Neurosci. Biobehav. Rev. 26, 1–11. https://doi.org/10.1016/S0149-7634(01)00057-4

Appendix A: Kinematics of the Frontal Impact Simulations

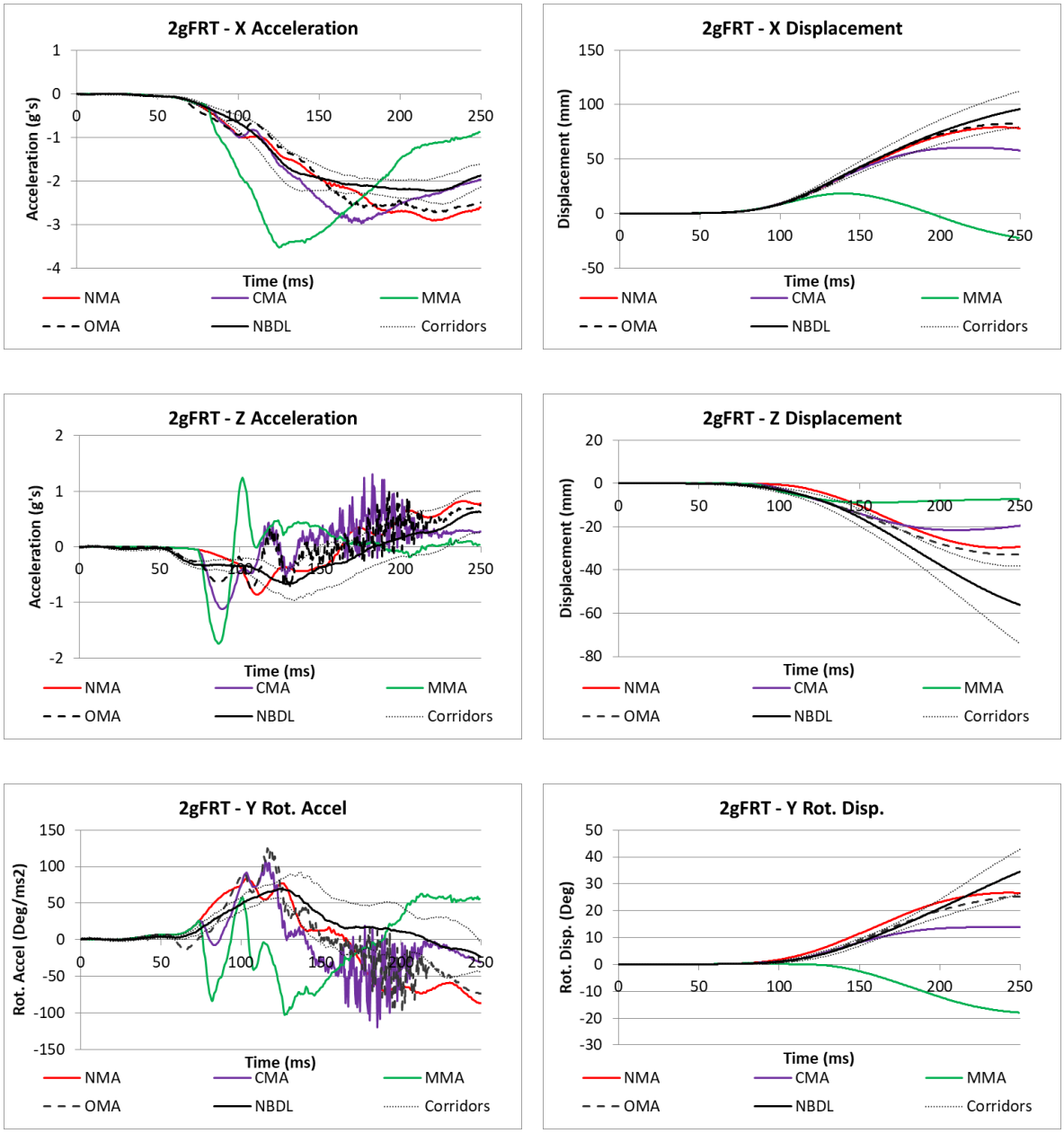

Figure 6-1: Head center of gravity kinematics for the 2g frontal impact in the global coordinate system for all plots except for the linear displacements that are in the local T1 coordinate system.

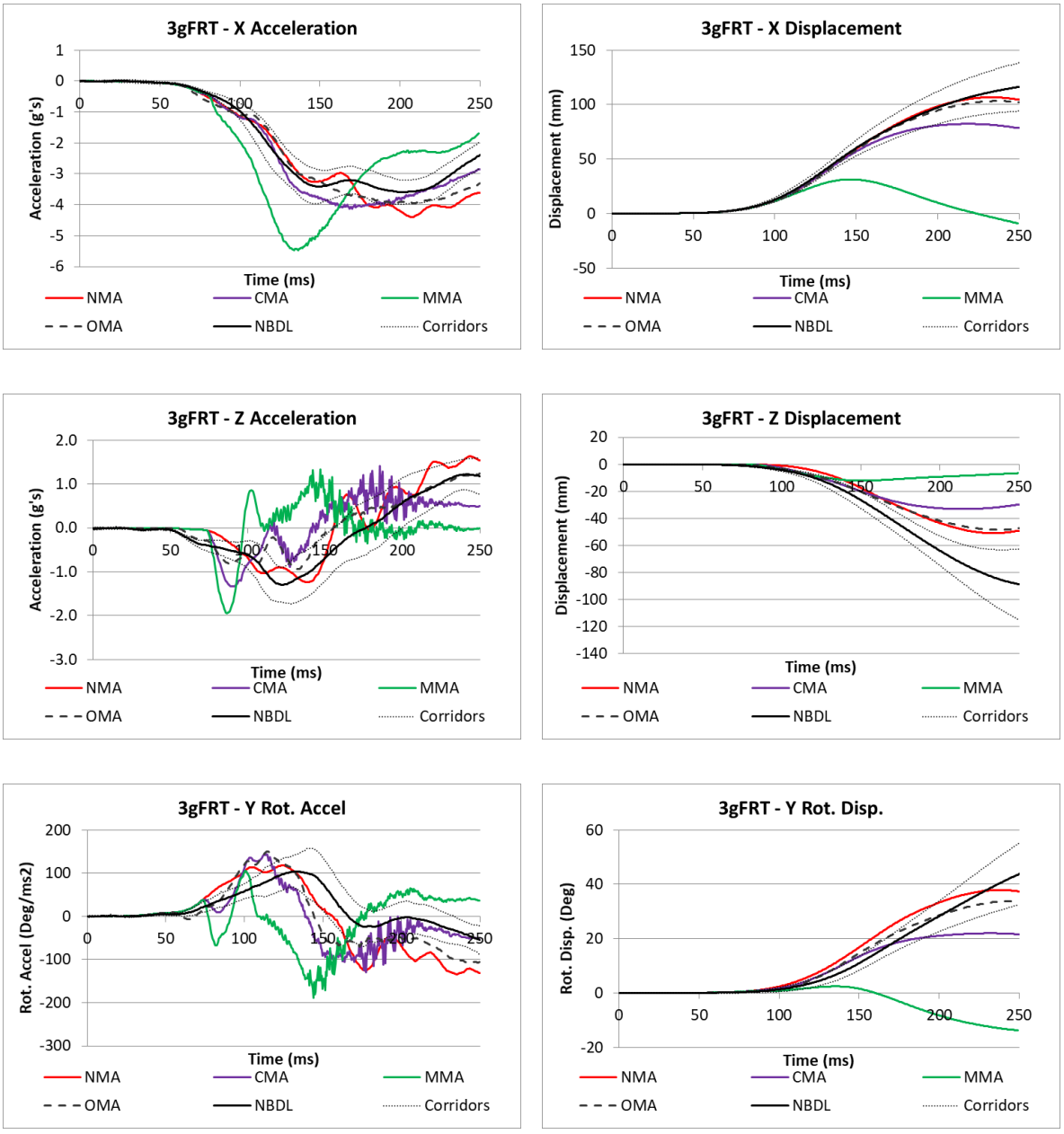

Figure 6-2: Head center of gravity kinematics for the 3g frontal impact in the global coordinate system for all plots except for the linear displacements that are in the local T1 coordinate system.

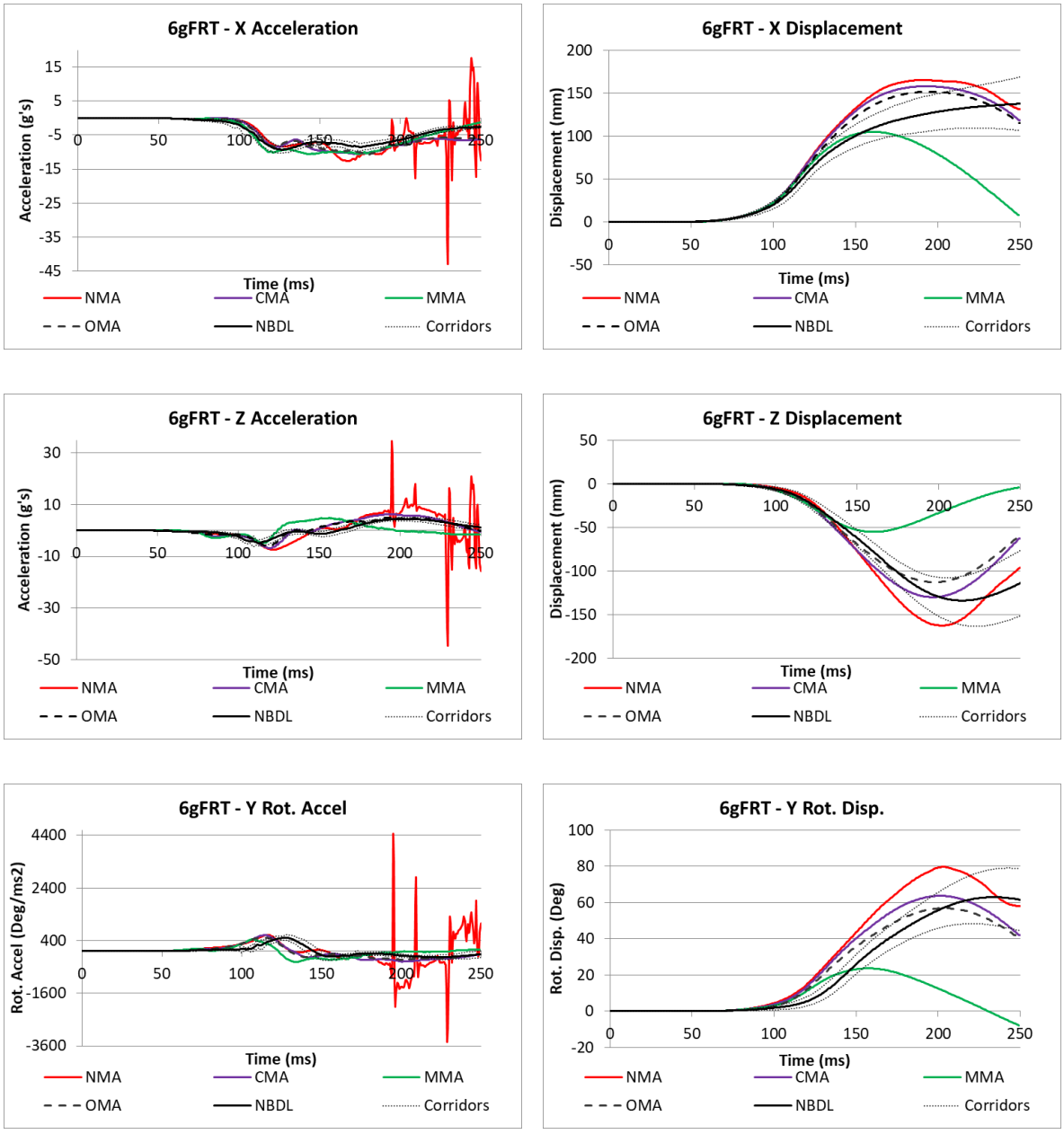

Figure 6-3: Head center of gravity kinematics for the 6g frontal impact in the global coordinate system for all plots except for the linear displacements that are in the local T1 coordinate system.

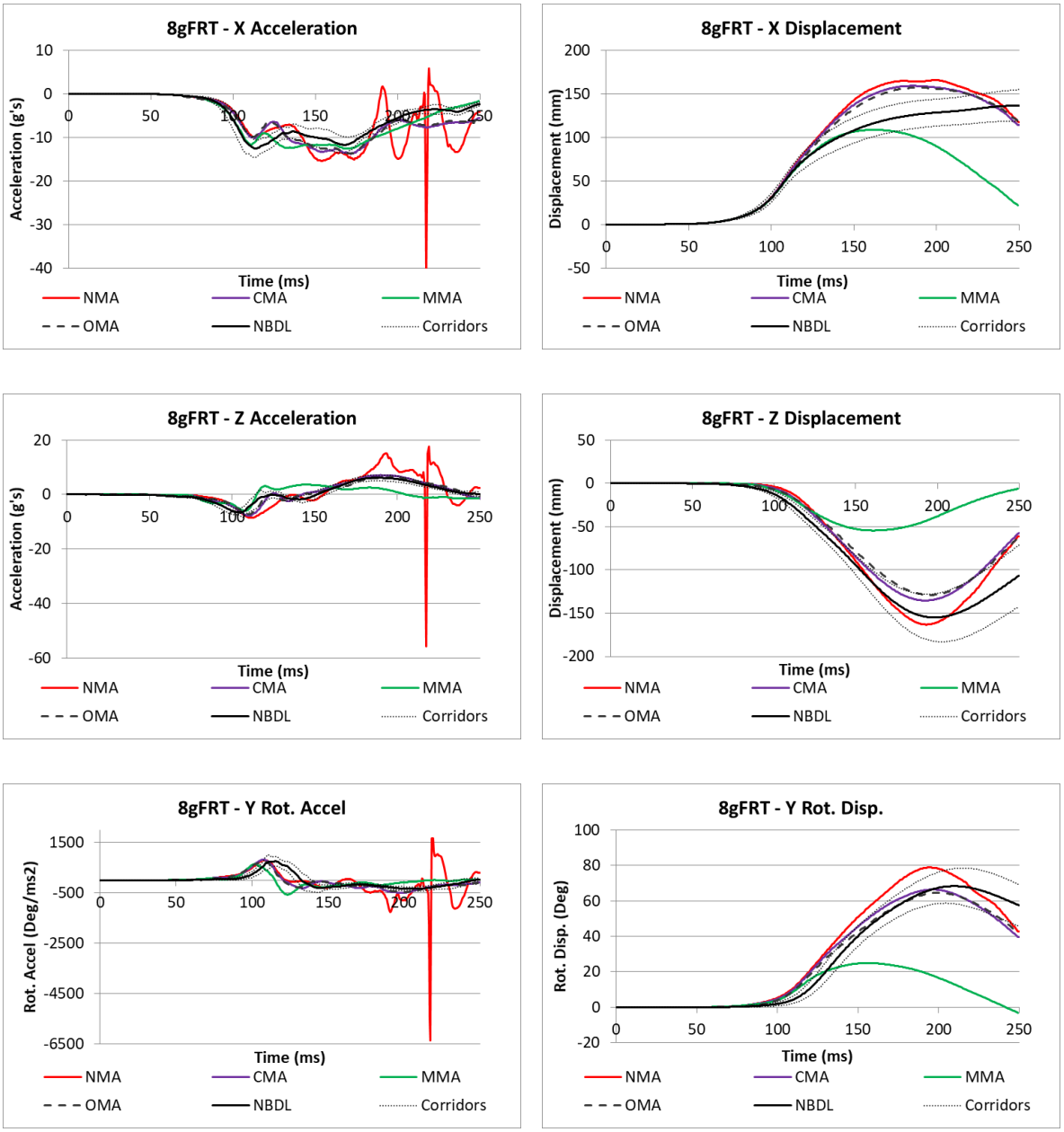

Figure 6-4: Head center of gravity kinematics for the 8g frontal impact in the global coordinate system for all plots except for the linear displacements that are in the local T1 coordinate system.

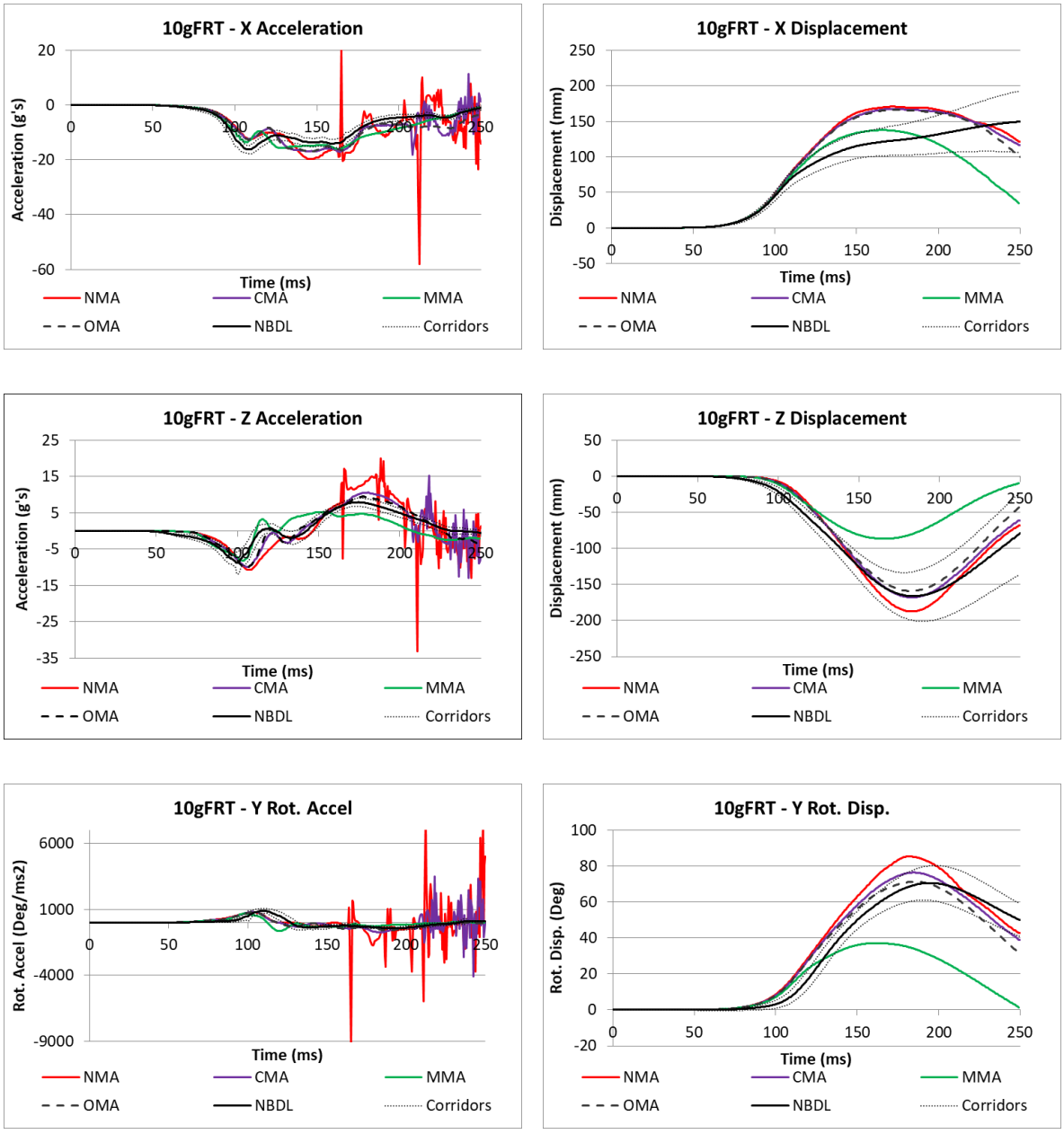

Figure 6-5: Head center of gravity kinematics for the 10g frontal impact in the global coordinate system for all plots except for the linear displacements that are in the local T1 coordinate system.

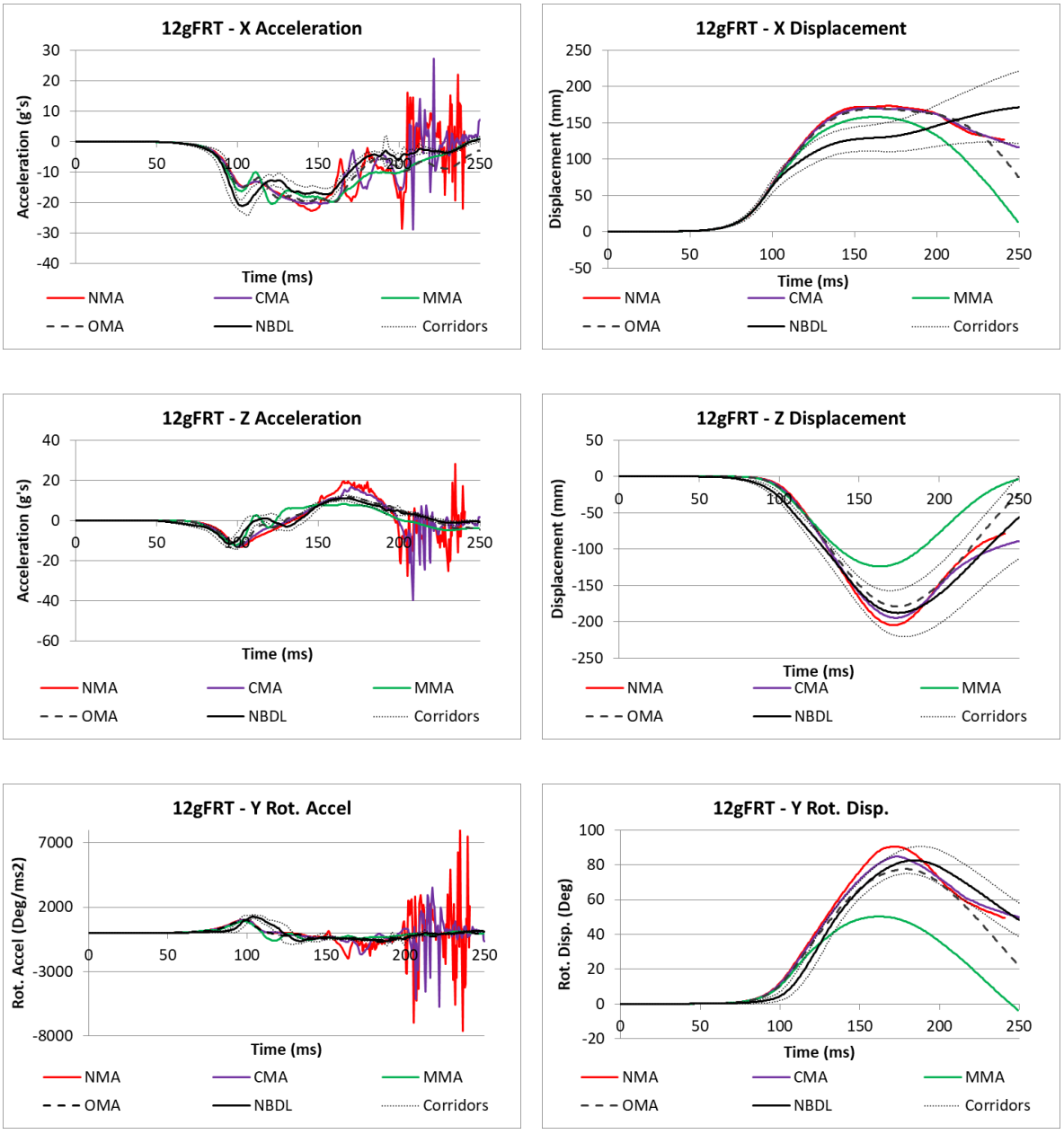

Figure 6-6: Head center of gravity kinematics for the 12g frontal impact in the global coordinate system for all plots except for the linear displacements that are in the local T1 coordinate system.

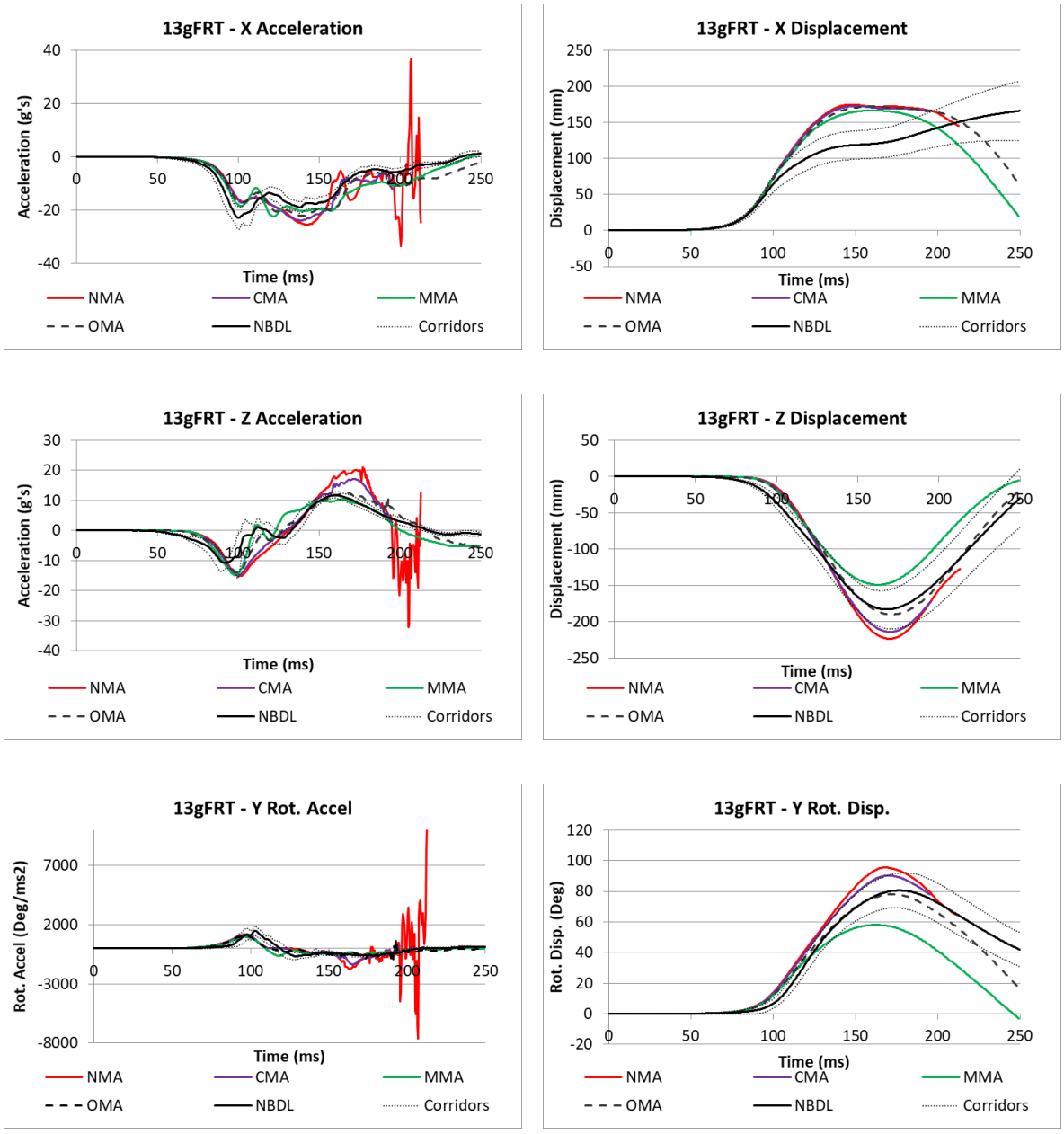

Figure 6-7: Head center of gravity kinematics for the 13g frontal impact in the global coordinate system for all plots except for the linear displacements that are in the local T1 coordinate system.

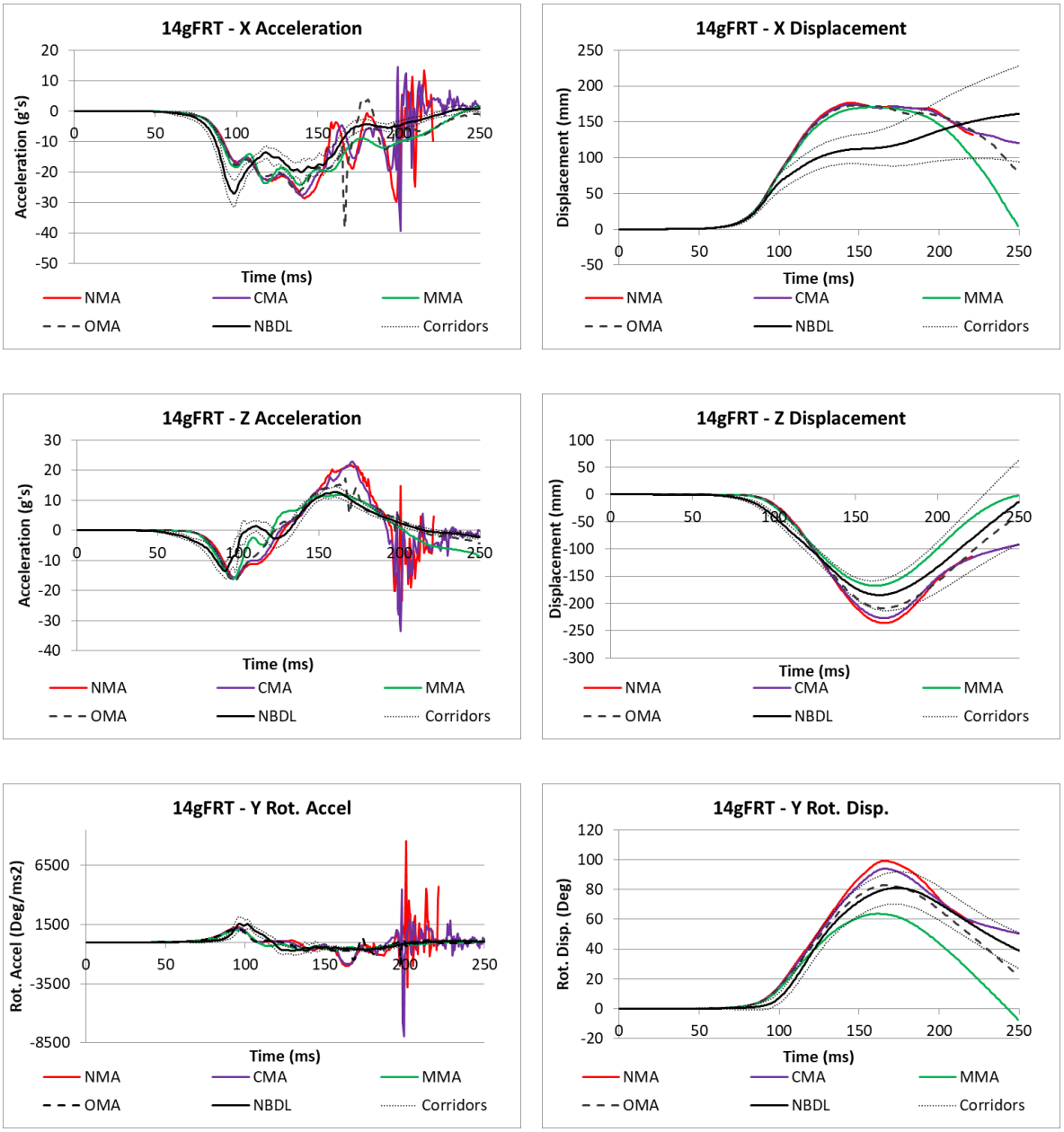

Figure 6-8: Head center of gravity kinematics for the 14g frontal impact in the global coordinate system for all plots except for the linear displacements that are in the local T1 coordinate system.

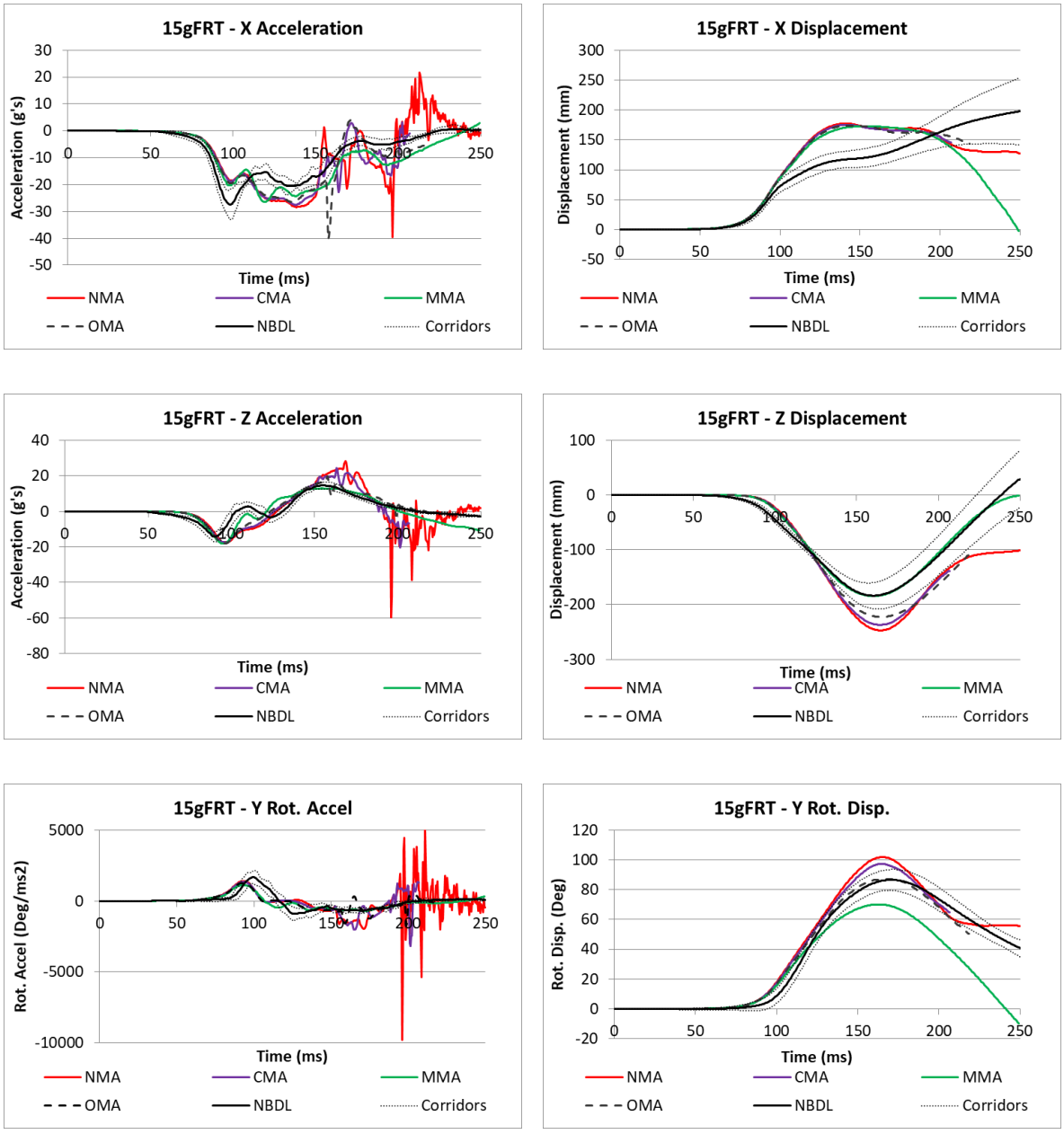

Figure 6-9: Head center of gravity kinematics for the 15g frontal impact in the global coordinate system for all plots except for the linear displacements that are in the local T1 coordinate system.

Appendix B: Kinematics of the Lateral Impact Simulations

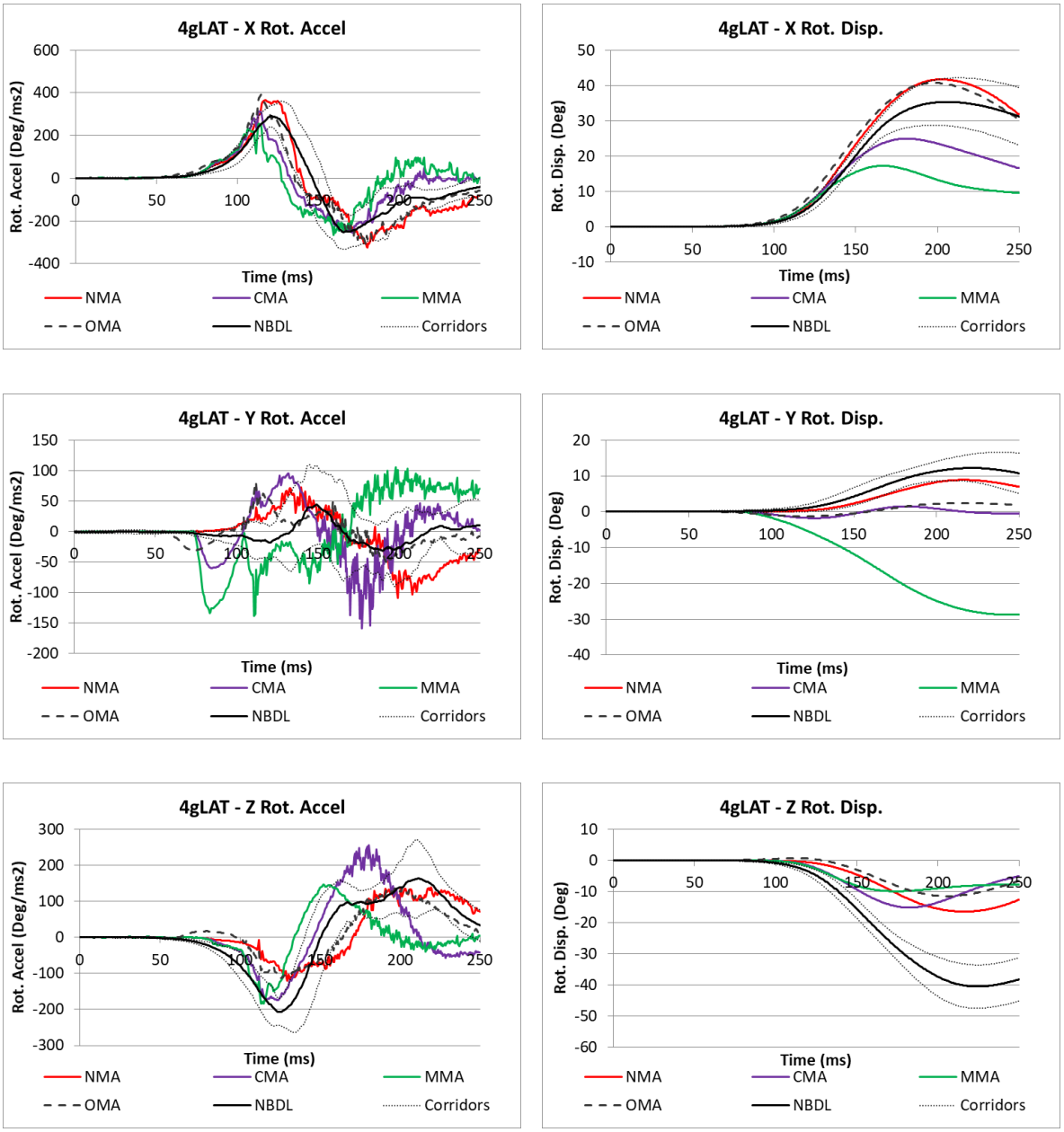

Figure 6-10: Head center of gravity kinematics for the 4g lateral impact in the global coordinate system.

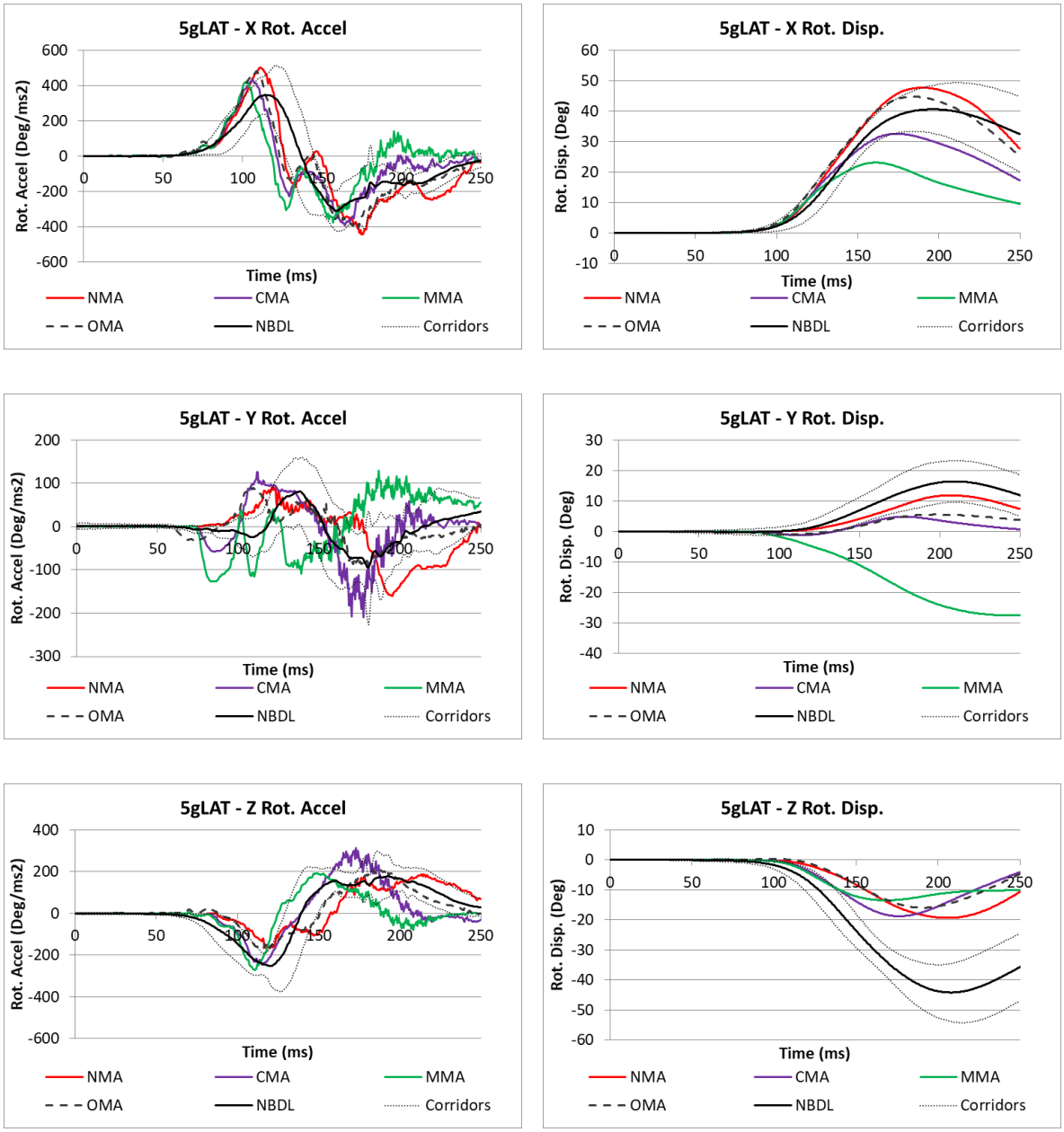

Figure 6-11: Head center of gravity kinematics for the 5g lateral impact in the global coordinate system.

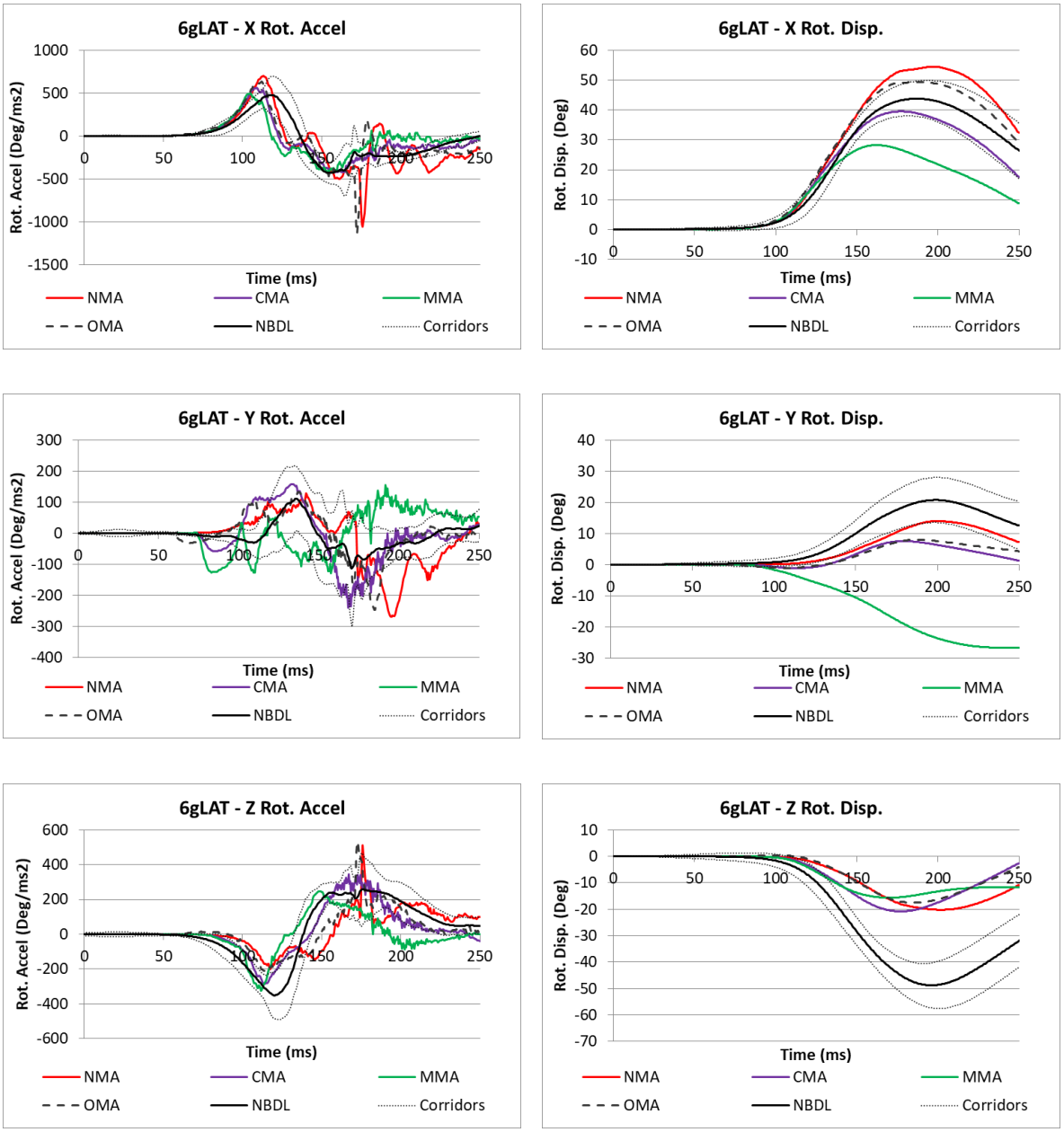

Figure 6-12: Head center of gravity kinematics for the 6g lateral impact in the global coordinate system.

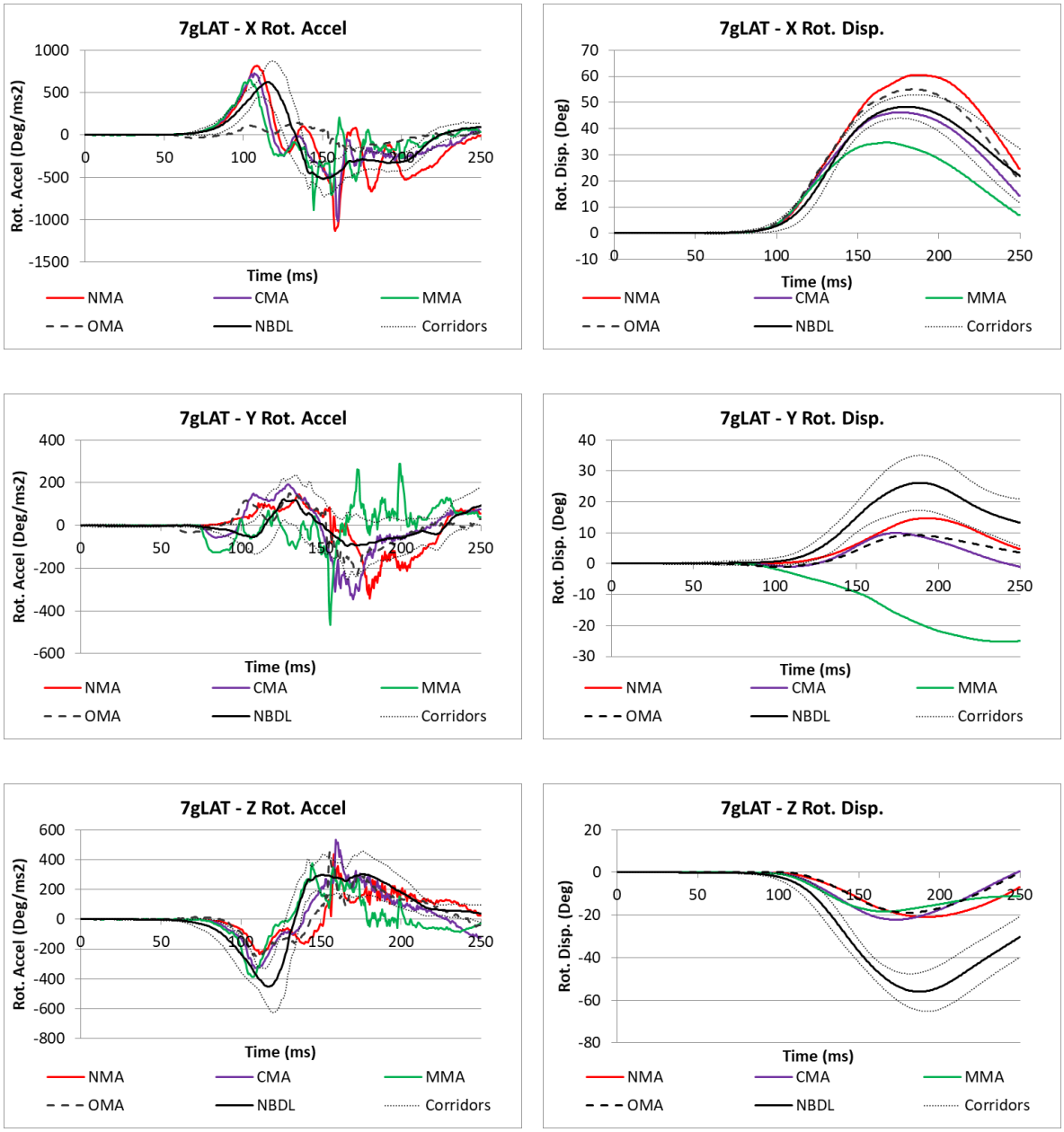

Figure 6-13: Head center of gravity kinematics for the 7g lateral impact in the global coordinate system.

Appendix C: Kinematics of the Rear Impact Simulations

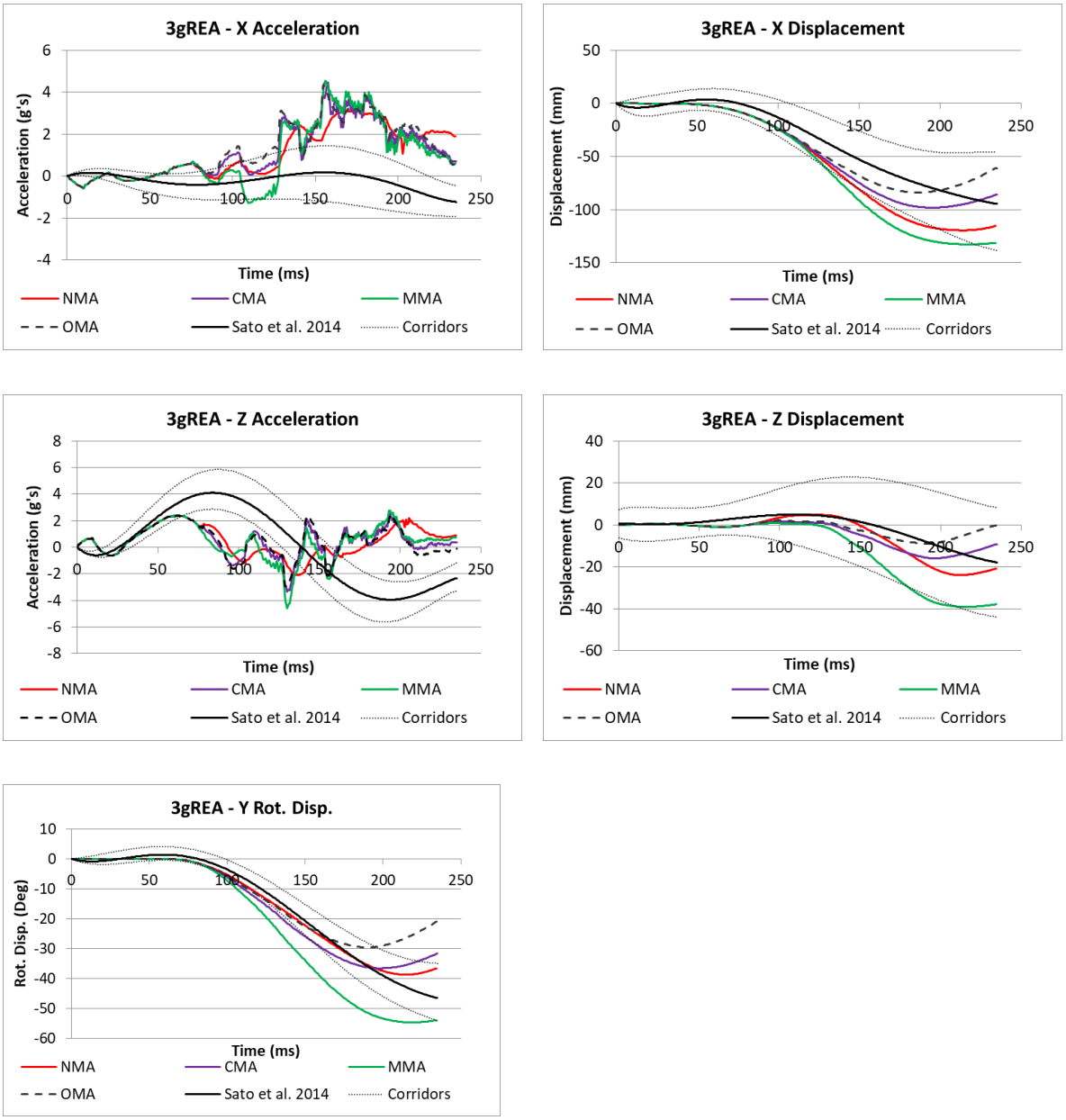

Figure 6-14: Head center of gravity kinematics for the 3g rear impact in the global coordinate system for all plots except for the linear displacements that are in the local T1 coordinate system.

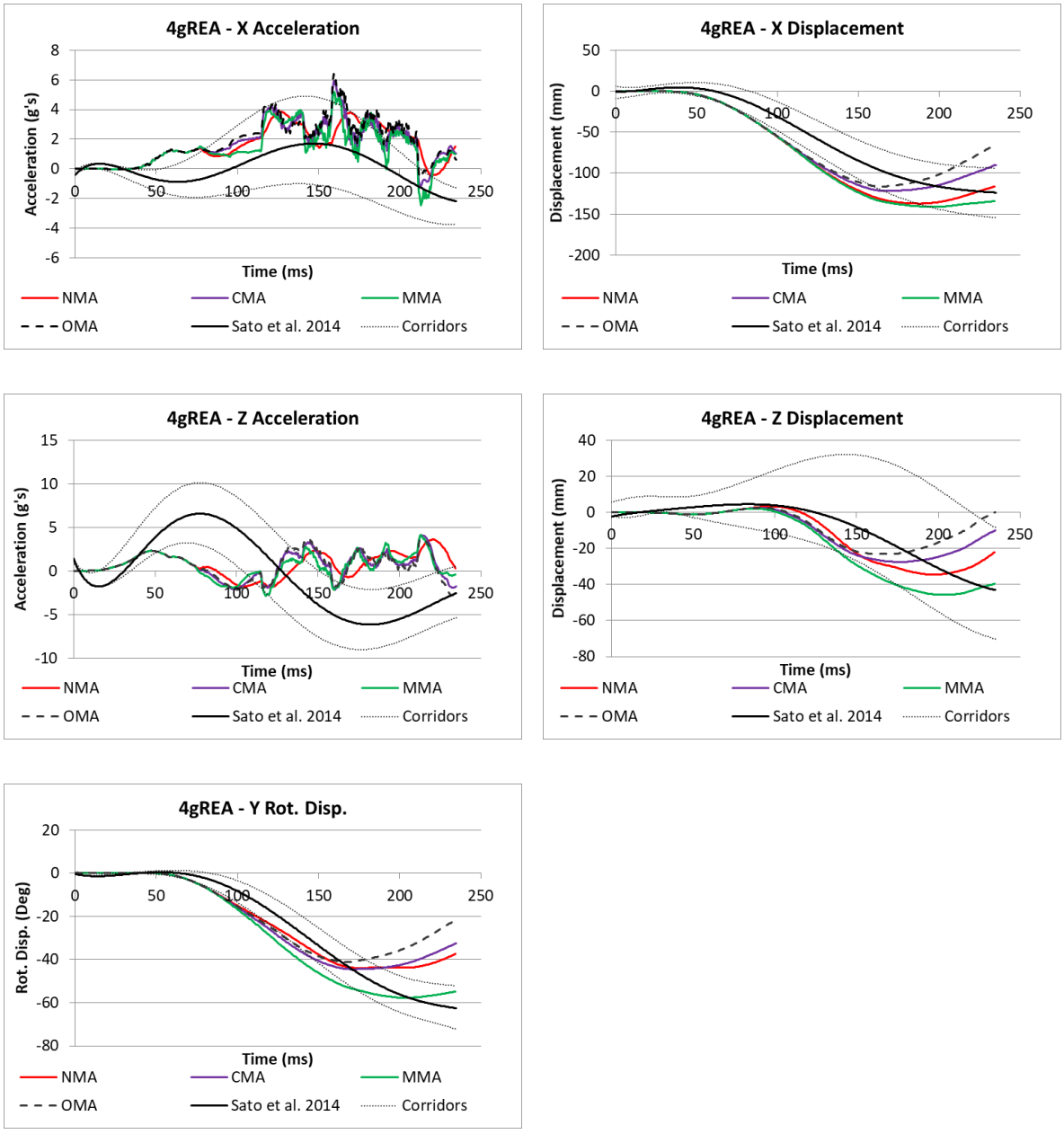

Figure 6-15: Head center of gravity kinematics for the 4g rear impact in the global coordinate system for all plots except for the linear displacements that are in the local T1 coordinate system.

Appendix D: Copyright Permission

Copyright Clearance Center Marketplace™

Springer - License Terms and Conditions

This is a License Agreement between Matheus Augusto Correia ("You") and Springer ("Publisher") provided by Copyright Clearance Center ("CCC"). The license consists of your order details, the terms and conditions provided by Springer, and the CCC terms and conditions.

All payments must be made in full to CCC.

Order Date	11-Mar-2020	**Type of Use**	Republish in a thesis/dissertation
Order license ID	1022624-1		
ISBN-13	978-3-642-53919-0	**Publisher**	Springer Berlin Heidelberg
		Portion	Image/photo/illustration

LICENSED CONTENT

Publication Title	Trauma Biomechanics	**Country**	Germany
Author/Editor	Walz, Felix, Muser, Markus H., Cronin, Duane S., Niederer, Peter F., Schmitt, Kai-Uwe	**Rightsholder**	Springer
		Publication Type	Book
		URL	http://link.springer.com/10.1007/978-3-642-53920-6
Date	01/01/2014		
Language	English		

REQUEST DETAILS

Portion Type	Image/photo/illustration	**Distribution**	Worldwide
Number of images / photos / illustrations	1	**Translation**	Original language of publication
Format (select all that apply)	Print, Electronic	**Copies for the disabled?**	No
		Minor editing privileges?	No
Who will republish the content?	Academic institution	**Incidental promotional use?**	No
		Currency	CAD
Duration of Use	Life of current edition		
Lifetime Unit Quantity	Up to 499		
Rights Requested	Main product		

NEW WORK DETAILS

Title	Activation of Neck Musculature During Frontal, Lateral and Rear Impacts using Detailed Finite Element Modeling	**Institution name**	University of Waterloo
		Expected presentation date	2020-04-30
Instructor name	Duane Cronin		

ADDITIONAL DETAILS

Order reference number	N/A	**The requesting person / organization to appear on the license**	Matheus Augusto Correia

REUSE CONTENT DETAILS

Title, description or numeric reference of the portion(s)	Figure 4.6	**Title of the article/chapter the portion is from**	Spinal Injuries
Editor of portion(s)	N/A	**Author of portion(s)**	Walz, Felix; Muser, Markus H.; Cronin, Duane S.; Niederer, Peter F.; Schmitt, Kai-Uwe
Volume of serial or monograph	N/A		
Page or page range of portion	85	**Issue, if republishing an article from a serial**	N/A
		Publication date of portion	2014-01-01

PUBLISHER TERMS AND CONDITIONS

A maximum of 10% of the content may be licensed for republication. The user is responsible for identifying and seeking separate licenses for any third party materials that are identified anywhere in the work. Without a separate license, such third party materials may not be reused.
If you are placing a request on behalf of/for a corporate organization, please use RightsLink.For further information visit
http://www.nature.com/reprints/permission-requests.html and
https://www.springer.com/gp/rights-permissions/obtaining-permissions/882

CCC Republication Terms and Conditions

1. Description of Service; Defined Terms. This Republication License enables the User to obtain licenses for republication of one or more copyrighted works as described in detail on the relevant Order Confirmation (the "Work(s)"). Copyright Clearance Center, Inc. ("CCC") grants licenses through the Service on behalf of the rightsholder identified on the Order Confirmation (the "Rightsholder"). "Republication", as used herein, generally means the inclusion of a Work, in whole or in part, in a new work or works, also as described on the Order Confirmation. "User", as used herein, means the person or entity making such republication.

2. The terms set forth in the relevant Order Confirmation, and any terms set by the Rightsholder with respect to a particular Work, govern the terms of use of Works in connection with the Service. By using the Service, the person transacting for a republication license on behalf of the User represents and warrants that he/she/it (a) has been duly authorized by the User to accept, and hereby does accept, all such terms and conditions on behalf of User, and (b) shall inform User of all such terms and conditions. In the event such person is a "freelancer" or other third party independent of User and CCC, such party shall be deemed jointly a "User" for purposes of these terms and conditions. In any event, User shall be deemed to have accepted and agreed to all such terms and conditions if User republishes the Work in any fashion.

3. Scope of License; Limitations and Obligations.

   3.1. All Works and all rights therein, including copyright rights, remain the sole and exclusive property of the Rightsholder. The license created by the exchange of an Order Confirmation (and/or any invoice) and payment by User of the full amount set forth on that document includes only those rights expressly set forth in the Order Confirmation and in these terms and conditions, and conveys no other rights in the Work(s) to User. All rights not expressly granted are hereby reserved.

   3.2. General Payment Terms: You may pay by credit card or through an account with us payable at the end of the month. If you and we agree that you may establish a standing account with CCC, then the following terms apply: Remit Payment to: Copyright Clearance Center, 29118 Network Place, Chicago, IL 60673-1291. Payments Due: Invoices are payable upon their delivery to you (or upon our notice to you that they are available to you for downloading). After 30 days, outstanding amounts will be subject to a service charge of 1-1/2% per month or, if less, the maximum rate allowed by applicable law. Unless otherwise specifically set forth in the Order Confirmation or in a separate written agreement signed by CCC, invoices are due and payable on "net 30" terms. While User may exercise the rights licensed immediately upon issuance of the Order Confirmation, the license is automatically revoked and is null and void, as if it had never been issued, if complete payment for the license is not received on a timely basis either from User directly or through a payment agent, such as a credit card company.

   3.3. Unless otherwise provided in the Order Confirmation, any grant of rights to User (i) is "one-time" (including the editions and product family specified in the license), (ii) is non-exclusive and non-transferable and (iii) is subject to any and all limitations and restrictions (such as, but not limited to, limitations on duration of use or circulation) included in the Order Confirmation or invoice and/or in these terms and conditions. Upon completion of the licensed use, User shall either secure a new permission for further use of the Work(s) or immediately cease any new use of the Work(s) and shall render inaccessible (such as by deleting or by removing or severing links or other

locators) any further copies of the Work (except for copies printed on paper in accordance with this license and still in User's stock at the end of such period).

3.4. In the event that the material for which a republication license is sought includes third party materials (such as photographs, illustrations, graphs, inserts and similar materials) which are identified in such material as having been used by permission, User is responsible for identifying, and seeking separate licenses (under this Service or otherwise) for, any of such third party materials; without a separate license, such third party materials may not be used.

3.5. Use of proper copyright notice for a Work is required as a condition of any license granted under the Service. Unless otherwise provided in the Order Confirmation, a proper copyright notice will read substantially as follows: "Republished with permission of [Rightsholder's name], from [Work's title, author, volume, edition number and year of copyright]; permission conveyed through Copyright Clearance Center, Inc. " Such notice must be provided in a reasonably legible font size and must be placed either immediately adjacent to the Work as used (for example, as part of a by-line or footnote but not as a separate electronic link) or in the place where substantially all other credits or notices for the new work containing the republished Work are located. Failure to include the required notice results in loss to the Rightsholder and CCC, and the User shall be liable to pay liquidated damages for each such failure equal to twice the use fee specified in the Order Confirmation, in addition to the use fee itself and any other fees and charges specified.

3.6. User may only make alterations to the Work if and as expressly set forth in the Order Confirmation. No Work may be used in any way that is defamatory, violates the rights of third parties (including such third parties' rights of copyright, privacy, publicity, or other tangible or intangible property), or is otherwise illegal, sexually explicit or obscene. In addition, User may not conjoin a Work with any other material that may result in damage to the reputation of the Rightsholder. User agrees to inform CCC if it becomes aware of any infringement of any rights in a Work and to cooperate with any reasonable request of CCC or the Rightsholder in connection therewith.

4. Indemnity. User hereby indemnifies and agrees to defend the Rightsholder and CCC, and their respective employees and directors, against all claims, liability, damages, costs and expenses, including legal fees and expenses, arising out of any use of a Work beyond the scope of the rights granted herein, or any use of a Work which has been altered in any unauthorized way by User, including claims of defamation or infringement of rights of copyright, publicity, privacy or other tangible or intangible property.

5. Limitation of Liability. UNDER NO CIRCUMSTANCES WILL CCC OR THE RIGHTSHOLDER BE LIABLE FOR ANY DIRECT, INDIRECT, CONSEQUENTIAL OR INCIDENTAL DAMAGES (INCLUDING WITHOUT LIMITATION DAMAGES FOR LOSS OF BUSINESS PROFITS OR INFORMATION, OR FOR BUSINESS INTERRUPTION) ARISING OUT OF THE USE OR INABILITY TO USE A WORK, EVEN IF ONE OF THEM HAS BEEN ADVISED OF THE POSSIBILITY OF SUCH DAMAGES. In any event, the total liability of the Rightsholder and CCC (including their respective employees and directors) shall not exceed the total amount actually paid by User for this license. User assumes full liability for the actions and omissions of its principals, employees, agents, affiliates, successors and assigns.

6. Limited Warranties. THE WORK(S) AND RIGHT(S) ARE PROVIDED "AS IS". CCC HAS THE RIGHT TO GRANT TO USER THE RIGHTS GRANTED IN THE ORDER CONFIRMATION DOCUMENT. CCC AND THE RIGHTSHOLDER DISCLAIM ALL OTHER WARRANTIES RELATING TO THE WORK(S) AND RIGHT(S), EITHER EXPRESS OR IMPLIED, INCLUDING WITHOUT LIMITATION IMPLIED WARRANTIES OF MERCHANTABILITY OR FITNESS FOR A PARTICULAR PURPOSE. ADDITIONAL RIGHTS MAY BE REQUIRED TO USE ILLUSTRATIONS, GRAPHS, PHOTOGRAPHS, ABSTRACTS, INSERTS OR OTHER PORTIONS OF THE WORK (AS OPPOSED TO THE ENTIRE WORK) IN A MANNER CONTEMPLATED BY USER; USER UNDERSTANDS AND AGREES THAT NEITHER CCC NOR THE RIGHTSHOLDER MAY HAVE SUCH ADDITIONAL RIGHTS TO GRANT.

7. Effect of Breach. Any failure by User to pay any amount when due, or any use by User of a Work beyond the scope of the license set forth in the Order Confirmation and/or these terms and conditions, shall be a material breach of the license created by the Order Confirmation and these terms and conditions. Any breach not cured within 30 days of written notice thereof shall result in immediate termination of such license without further notice. Any unauthorized (but licensable) use of a Work that is terminated immediately upon notice thereof may be liquidated by payment of the Rightsholder's ordinary license price therefor; any unauthorized (and unlicensable) use that is not terminated immediately for any reason (including, for example, because materials containing the Work cannot reasonably be recalled) will be subject to all remedies available at law or in equity, but in no event to a payment of less than three times the Rightsholder's ordinary license price for the most closely analogous licensable use plus Rightsholder's and/or CCC's costs and expenses incurred in collecting such payment.

8. Miscellaneous.

8.1. User acknowledges that CCC may, from time to time, make changes or additions to the Service or to these terms and conditions, and CCC reserves the right to send notice to the User by electronic mail or otherwise for the purposes of notifying User of such changes or additions; provided that any such changes or additions shall not apply to permissions already secured and paid for.

8.2. Use of User-related information collected through the Service is governed by CCC's privacy policy, available online here:https://marketplace.copyright.com/rs-ui-web/mp/privacy-policy

8.3. The licensing transaction described in the Order Confirmation is personal to User. Therefore, User may not assign or transfer to any other person (whether a natural person or an organization of any kind) the license created by the Order Confirmation and these terms and conditions or any rights granted hereunder; provided, however, that User may assign such license in its entirety on written notice to CCC in the event of a transfer of all or substantially all of User's rights in the new material which includes the Work(s) licensed under this Service.

8.4. No amendment or waiver of any terms is binding unless set forth in writing and signed by the parties. The Rightsholder and CCC hereby object to any terms contained in any writing prepared by the User or its principals, employees, agents or affiliates and purporting to govern or otherwise relate to the licensing transaction described in the Order Confirmation, which terms are in any way inconsistent with any terms set forth in the Order Confirmation and/or in these terms and conditions or CCC's standard operating procedures, whether such writing is prepared prior to, simultaneously with or subsequent to the Order Confirmation, and whether such writing appears on a copy of the Order Confirmation or in a separate instrument.

8.5. The licensing transaction described in the Order Confirmation document shall be governed by and construed under the law of the State of New York, USA, without regard to the principles thereof of conflicts of law. Any case, controversy, suit, action, or proceeding arising out of, in connection with, or related to such licensing transaction shall be brought, at CCC's sole discretion, in any federal or state court located in the County of New York, State of New York, USA, or in any federal or state court whose geographical jurisdiction covers the location of the Rightsholder set forth in the Order Confirmation. The parties expressly submit to the personal jurisdiction and venue of each such federal or state court.If you have any comments or questions about the Service or Copyright Clearance Center, please contact us at 978-750-8400 or send an e-mail to support@copyright.com.

v 1.1

Copyright Clearance Center Marketplace™

Elsevier Science & Technology Journals - License Terms and Conditions

This is a License Agreement between Matheus Augusto Correia ("You") and Elsevier Science & Technology Journals ("Publisher") provided by Copyright Clearance Center ("CCC"). The license consists of your order details, the terms and conditions provided by Elsevier Science & Technology Journals, and the CCC terms and conditions.

All payments must be made in full to CCC.

Order Date	11-Mar-2020	**Type of Use**	Republish in a thesis/dissertation
Order license ID	1022623-1		
ISSN	0149-7634	**Publisher**	PERGAMON
		Portion	Image/photo/illustration

LICENSED CONTENT

Publication Title	Neuroscience and biobehavioral reviews	**Publication Type**	Journal
		Start Page	1
Article Title	Tactile, acoustic and vestibular systems sum to elicit the startle reflex	**End Page**	11
		Issue	1
Date	01/01/1978	**Volume**	26
Language	English, English		
Country	United Kingdom of Great Britain and Northern Ireland		
Rightsholder	Elsevier Science & Technology Journals		

REQUEST DETAILS

Portion Type	Image/photo/illustration	**Distribution**	Worldwide
Number of images / photos / illustrations	1	**Translation**	Original language of publication
Format (select all that apply)	Print, Electronic	**Copies for the disabled?**	No
		Minor editing privileges?	No
Who will republish the content?	Academic institution	**Incidental promotional use?**	No
Duration of Use	Life of current edition	**Currency**	CAD
Lifetime Unit Quantity	Up to 499		
Rights Requested	Main product		

NEW WORK DETAILS

Title	Activation of Neck Musculature During Frontal, Lateral and Rear Impacts using Detailed Finite Element Modeling	**Institution name**	University of Waterloo
		Expected presentation date	2020-04-30

Instructor name	Duane Cronin

ADDITIONAL DETAILS

Order reference number	N/A	**The requesting person / organization to appear on the license**	Matheus Augusto Correia

REUSE CONTENT DETAILS

Title, description or numeric reference of the portion(s)	Figure 3	**Title of the article/chapter the portion is from**	Tactile, acoustic and vestibular systems sum to elicit the startle reflex
Editor of portion(s)	Yeomans, John S; Li, Liang; Scott, Brian W; Frankland, Paul W	**Author of portion(s)**	Yeomans, John S; Li, Liang; Scott, Brian W; Frankland, Paul W
Volume of serial or monograph	26	**Issue, if republishing an article from a serial**	1
Page or page range of portion	1-11	**Publication date of portion**	2002-01-01

PUBLISHER TERMS AND CONDITIONS

Elsevier publishes Open Access articles in both its Open Access journals and via its Open Access articles option in subscription journals, for which an author selects a user license permitting certain types of reuse without permission. Before proceeding please check if the article is Open Access on http://www.sciencedirect.com and refer to the user license for the individual article. Any reuse not included in the user license terms will require permission. You must always fully and appropriately credit the author and source. If any part of the material to be used (for example, figures) has appeared in the Elsevier publication for which you are seeking permission, with credit or acknowledgement to another source it is the responsibility of the user to ensure their reuse complies with the terms and conditions determined by the rights holder. Please contact permissions@elsevier.com with any queries.

CCC Republication Terms and Conditions

1. Description of Service; Defined Terms. This Republication License enables the User to obtain licenses for republication of one or more copyrighted works as described in detail on the relevant Order Confirmation (the "Work(s)"). Copyright Clearance Center, Inc. ("CCC") grants licenses through the Service on behalf of the rightsholder identified on the Order Confirmation (the "Rightsholder"). "Republication", as used herein, generally means the inclusion of a Work, in whole or in part, in a new work or works, also as described on the Order Confirmation. "User", as used herein, means the person or entity making such republication.

2. The terms set forth in the relevant Order Confirmation, and any terms set by the Rightsholder with respect to a particular Work, govern the terms of use of Works in connection with the Service. By using the Service, the person transacting for a republication license on behalf of the User represents and warrants that he/she/it (a) has been duly authorized by the User to accept, and hereby does accept, all such terms and conditions on behalf of User, and (b) shall inform User of all such terms and conditions. In the event such person is a "freelancer" or other third party independent of User and CCC, such party shall be deemed jointly a "User" for purposes of these terms and conditions. In any event, User shall be deemed to have accepted and agreed to all such terms and conditions if User republishes the Work in any fashion.

3. Scope of License; Limitations and Obligations.

    3.1. All Works and all rights therein, including copyright rights, remain the sole and exclusive property of the Rightsholder. The license created by the exchange of an Order Confirmation (and/or any invoice) and payment by User of the full amount set forth on that document includes only those rights expressly set forth in the Order Confirmation and in these terms and conditions, and conveys no other rights in the

Work(s) to User. All rights not expressly granted are hereby reserved.

3.2. General Payment Terms: You may pay by credit card or through an account with us payable at the end of the month. If you and we agree that you may establish a standing account with CCC, then the following terms apply: Remit Payment to: Copyright Clearance Center, 29118 Network Place, Chicago, IL 60673-1291. Payments Due: Invoices are payable upon their delivery to you (or upon our notice to you that they are available to you for downloading). After 30 days, outstanding amounts will be subject to a service charge of 1-1/2% per month or, if less, the maximum rate allowed by applicable law. Unless otherwise specifically set forth in the Order Confirmation or in a separate written agreement signed by CCC, invoices are due and payable on "net 30" terms. While User may exercise the rights licensed immediately upon issuance of the Order Confirmation, the license is automatically revoked and is null and void, as if it had never been issued, if complete payment for the license is not received on a timely basis either from User directly or through a payment agent, such as a credit card company.

3.3. Unless otherwise provided in the Order Confirmation, any grant of rights to User (i) is "one-time" (including the editions and product family specified in the license), (ii) is non-exclusive and non-transferable and (iii) is subject to any and all limitations and restrictions (such as, but not limited to, limitations on duration of use or circulation) included in the Order Confirmation or invoice and/or in these terms and conditions. Upon completion of the licensed use, User shall either secure a new permission for further use of the Work(s) or immediately cease any new use of the Work(s) and shall render inaccessible (such as by deleting or by removing or severing links or other locators) any further copies of the Work (except for copies printed on paper in accordance with this license and still in User's stock at the end of such period).

3.4. In the event that the material for which a republication license is sought includes third party materials (such as photographs, illustrations, graphs, inserts and similar materials) which are identified in such material as having been used by permission, User is responsible for identifying, and seeking separate licenses (under this Service or otherwise) for, any of such third party materials; without a separate license, such third party materials may not be used.

3.5. Use of proper copyright notice for a Work is required as a condition of any license granted under the Service. Unless otherwise provided in the Order Confirmation, a proper copyright notice will read substantially as follows: "Republished with permission of [Rightsholder's name], from [Work's title, author, volume, edition number and year of copyright]; permission conveyed through Copyright Clearance Center, Inc. " Such notice must be provided in a reasonably legible font size and must be placed either immediately adjacent to the Work as used (for example, as part of a by-line or footnote but not as a separate electronic link) or in the place where substantially all other credits or notices for the new work containing the republished Work are located. Failure to include the required notice results in loss to the Rightsholder and CCC, and the User shall be liable to pay liquidated damages for each such failure equal to twice the use fee specified in the Order Confirmation, in addition to the use fee itself and any other fees and charges specified.

3.6. User may only make alterations to the Work if and as expressly set forth in the Order Confirmation. No Work may be used in any way that is defamatory, violates the rights of third parties (including such third parties' rights of copyright, privacy, publicity, or other tangible or intangible property), or is otherwise illegal, sexually explicit or obscene. In addition, User may not conjoin a Work with any other material that may result in damage to the reputation of the Rightsholder. User agrees to inform CCC if it becomes aware of any infringement of any rights in a Work and to cooperate with any reasonable request of CCC or the Rightsholder in connection therewith.

4. Indemnity. User hereby indemnifies and agrees to defend the Rightsholder and CCC, and their respective employees and directors, against all claims, liability, damages, costs and expenses, including legal fees and expenses, arising out of any use of a Work beyond the scope of the rights granted herein, or any use of a Work which has been altered in any unauthorized way by User, including claims of defamation or infringement of rights of copyright, publicity, privacy or other tangible or intangible property.

5. Limitation of Liability. UNDER NO CIRCUMSTANCES WILL CCC OR THE RIGHTSHOLDER BE LIABLE FOR ANY DIRECT,

INDIRECT, CONSEQUENTIAL OR INCIDENTAL DAMAGES (INCLUDING WITHOUT LIMITATION DAMAGES FOR LOSS OF BUSINESS PROFITS OR INFORMATION, OR FOR BUSINESS INTERRUPTION) ARISING OUT OF THE USE OR INABILITY TO USE A WORK, EVEN IF ONE OF THEM HAS BEEN ADVISED OF THE POSSIBILITY OF SUCH DAMAGES. In any event, the total liability of the Rightsholder and CCC (including their respective employees and directors) shall not exceed the total amount actually paid by User for this license. User assumes full liability for the actions and omissions of its principals, employees, agents, affiliates, successors and assigns.

6. Limited Warranties. THE WORK(S) AND RIGHT(S) ARE PROVIDED "AS IS". CCC HAS THE RIGHT TO GRANT TO USER THE RIGHTS GRANTED IN THE ORDER CONFIRMATION DOCUMENT. CCC AND THE RIGHTSHOLDER DISCLAIM ALL OTHER WARRANTIES RELATING TO THE WORK(S) AND RIGHT(S), EITHER EXPRESS OR IMPLIED, INCLUDING WITHOUT LIMITATION IMPLIED WARRANTIES OF MERCHANTABILITY OR FITNESS FOR A PARTICULAR PURPOSE. ADDITIONAL RIGHTS MAY BE REQUIRED TO USE ILLUSTRATIONS, GRAPHS, PHOTOGRAPHS, ABSTRACTS, INSERTS OR OTHER PORTIONS OF THE WORK (AS OPPOSED TO THE ENTIRE WORK) IN A MANNER CONTEMPLATED BY USER; USER UNDERSTANDS AND AGREES THAT NEITHER CCC NOR THE RIGHTSHOLDER MAY HAVE SUCH ADDITIONAL RIGHTS TO GRANT.

7. Effect of Breach. Any failure by User to pay any amount when due, or any use by User of a Work beyond the scope of the license set forth in the Order Confirmation and/or these terms and conditions, shall be a material breach of the license created by the Order Confirmation and these terms and conditions. Any breach not cured within 30 days of written notice thereof shall result in immediate termination of such license without further notice. Any unauthorized (but licensable) use of a Work that is terminated immediately upon notice thereof may be liquidated by payment of the Rightsholder's ordinary license price therefor; any unauthorized (and unlicensable) use that is not terminated immediately for any reason (including, for example, because materials containing the Work cannot reasonably be recalled) will be subject to all remedies available at law or in equity, but in no event to a payment of less than three times the Rightsholder's ordinary license price for the most closely analogous licensable use plus Rightsholder's and/or CCC's costs and expenses incurred in collecting such payment.

8. Miscellaneous.

   8.1. User acknowledges that CCC may, from time to time, make changes or additions to the Service or to these terms and conditions, and CCC reserves the right to send notice to the User by electronic mail or otherwise for the purposes of notifying User of such changes or additions; provided that any such changes or additions shall not apply to permissions already secured and paid for.

   8.2. Use of User-related information collected through the Service is governed by CCC's privacy policy, available online here:https://marketplace.copyright.com/rs-ui-web/mp/privacy-policy

   8.3. The licensing transaction described in the Order Confirmation is personal to User. Therefore, User may not assign or transfer to any other person (whether a natural person or an organization of any kind) the license created by the Order Confirmation and these terms and conditions or any rights granted hereunder; provided, however, that User may assign such license in its entirety on written notice to CCC in the event of a transfer of all or substantially all of User's rights in the new material which includes the Work(s) licensed under this Service.

   8.4. No amendment or waiver of any terms is binding unless set forth in writing and signed by the parties. The Rightsholder and CCC hereby object to any terms contained in any writing prepared by the User or its principals, employees, agents or affiliates and purporting to govern or otherwise relate to the licensing transaction described in the Order Confirmation, which terms are in any way inconsistent with any terms set forth in the Order Confirmation and/or in these terms and conditions or CCC's standard operating procedures, whether such writing is prepared prior to, simultaneously with or subsequent to the Order Confirmation, and whether such writing appears on a copy of the Order Confirmation or in a separate instrument.

   8.5. The licensing transaction described in the Order Confirmation document shall be governed by and construed under the law of the State of New York, USA, without regard to the principles thereof of conflicts of law. Any case, controversy, suit, action, or proceeding arising out of, in connection with, or related to such licensing transaction shall be brought, at CCC's sole discretion, in any federal or state court located in

the County of New York, State of New York, USA, or in any federal or state court whose geographical jurisdiction covers the location of the Rightsholder set forth in the Order Confirmation. The parties expressly submit to the personal jurisdiction and venue of each such federal or state court.If you have any comments or questions about the Service or Copyright Clearance Center, please contact us at 978-750-8400 or send an e-mail to support@copyright.com.

v 1.1